To myself I am only a child playing on the beach,
while vast oceans of truth lie undiscovered before me

- Isaac Newton

University of Alberta

Modification and Application of Gold Nanoparticles in Surface-Based Immunoassays

by

Lars Björn Laurentius

A thesis submitted to the Faculty of Graduate Studies and Research
in partial fulfillment of the requirements for the degree of

Doctor of Philosophy

Department of Chemistry

Fall 2012
Edmonton, Alberta

Abstract

Gold nanoparticles (AuNPs) are at the forefront of many research areas and generally require very specific surface functionalities to be compatible with targeted applications. Suitable modification schemes should be simple, fast, and robust. A common surface modification involves the use of thiols to coat the AuNPs with a thiolate monolayer; however, the lability of the sulfur-gold interaction can create problems in applications where high stability is required. Alternatively, this thesis explored the use of diazonium salts to modify gold nanoparticles.

In recent years diazonium cation grafting onto planar substrates has gained significant attention. The resulting layers show resilience and controllable properties such as film thickness and functionality. In order to extend this surface chemistry to include AuNPs, the conditions necessary for the spontaneous chemisorption of diazonium derived aryl films to pre-formed gold nanoparticles were developed. The spectroscopic characterization of these organic layers on gold nanoparticles provided evidence for a gold-carbon covalent bond. A direct comparison of nitrobenzene diazonium salt derived layers to the thiol analogue was used to show that diazonium salt modification schemes are similarly simple and fast in comparison, but also exhibit marked differences in film structure as they produce multilayers.

Gold nanoparticles are widely used in biosensing applications providing unique optical properties for signal enhancement and detection schemes. In UV-vis spectroscopy, localized surface plasmon resonance (LSPR) of the AuNPs

leads to an absorption band. The work presented in this thesis explored the capability of utilizing the LSPR band magnitude in a simple transmission UV-vis measurement to determine the nanoparticle density of adsorbed NPs on a transparent substrate. This led to the development of a new method to incorporate AuNPs as extrinsic labels in a sandwich immunoassay. The analyte, rabbit IgG, is captured on a transparent surface and labeled with AuNPs. This was accomplished by tailoring the surface chemistry of the nanoparticles specifically to the target analyte. Consequently, quantitating the magnitude of the LSPR band determines the number of AuNP-labels present on the biochip surface, which in turn is proportional to the analyte concentration captured. In this fashion detection limits on the order of 100 pM were achieved.

Acknowledgements

The University of Alberta has been my home for over 9 years during my B.Sc. and Ph.D. and, although I am glad to move on with my life, I will miss all the remarkable people here in Edmonton. Finishing my thesis has truly been a milestone, which could not have been achieved without the help of so many great friends and co-workers. Thank you to each and every one of you, for all the support and help over the years.

First and foremost, I am eternally grateful to my PhD supervisor, Mark McDermott. You have helped me both inside and outside the lab in becoming a better scientist and person. Your guidance and help throughout the years in graduate school has been invaluable. Thank you Mark for your continuous patience and support.

Also, thanks to my fellow group members: John Toman, Greg Kaufman, Michael Reid, Cici Cao, Ajawmolla Kebede, Shereen Elbayomy, Rongbing Du, Chongjun Pang, and Ibraheem Bushnak. You guys have always been available for advice, help and friendship. Special thanks to a few former group members; Dwayne Shewchuk, David Muñoz-Panaigua, Christ Grant, Rory Chisholm, Francis Nsiah, Aaron Skelhorne, Jane Cao, and Ni Yang, for all your help in the early years of my graduate studies, when I desperately needed help getting started with my research.

In addition, I would like to thank all the staff in the Department of Chemistry and at the National Institute for Nanotechnology (NINT) for their assistance over the years. Special thanks to Ryan Lister, Allan Chilton, Wayne

Moffat, Anita Weiler, Lynne Lechelt, Christie McDermott, and Gregory Kiema. Furthermore, thanks to all the staff at the Alberta Centre for Surface Engineering and Science (ACSES) for sample analysis and data interpretation. I would also like to express my gratitude to the following collaborators for their time and efforts: Rongbing Du, Greg Lopinski, Stanislav Stoyanov, and Hui Qian. Lastly, I am indebted to Richard McCreery for providing access to his facilities at NINT, and Amr Mahmoud for assisting me with countless titanium metal depositions.

Outside the lab and the University, I would like to acknowledge a few close friends that have kept me sane throughout my studies and have continuously provided a life outside of academia: Jacquelyn Jhingree, Tiffany Meinzer, Frank Liu, Craig Lytollis, Michel Gramm, Dagmar, Johannsen, Jordan Hemmes and Billy Wunarto. Thank you for always being there for me.

Last but not least, I am thankful to have such a great family that has supported me over the many years spent at the University of Alberta. The ones close to my heart are my mother, Bärbel; my dad, Hartmut; my brother, Sven; and my better half, Jeanine. You have kept encouraging me right from the start and all the way to the end. I could not have come this far without your help!

Table of Contents

List of Tables

List of Figures

List of Symbols

λ_{max}	Absorption band maximum / position
$\Delta\lambda$	Wavelength shift
m	Sensitivity factor (nm / refractive index units)
n	Refractive index
$n_{adsorbate}$	Refractive index of adsorbate
n_{medium}	Refractive index of medium
d	Adsorbate layer thickness (nm)
L_d	Electromagnetic field decay length (nm)
kDa	Kilo Daltons
MΩ	Mega Ohm
°C	Degrees Celsius
nm	Nanometer
mM	Mili molar
mL	Mili liter
h	Hour
µL	Micro liter
rpm	Revolutions per minute
s	Second
mW	Mili Watts
v/v	Volume/Volume
M	Molar
V	Volts
mV	Mili Volts
eV	Electron Volts
meV	Mili electron Volts
cm^{-1}	Wavenumber
w	Weak
kJ	Kilo Joule
Å	Angstrom

ω	Angular frequency
kV	Kilo Volts
n_{water}	Refractive index of water
σ_{ext}	Extinction cross section
σ_{abs}	Absorbance cross section
σ_{sca}	Scattering cross section
k	Wavevector
Re	Real
a_L	$\frac{m\psi_L(mx)\psi'_L(x) - \psi'_L(mx)\psi_L(x)}{m\psi_L(mx)\eta'_L(x) - \psi'_L(mx)\eta_L(x)}$
b_L	$\frac{\psi_L(mx)\psi'_L(x) - m\psi'_L(mx)\psi_L(x)}{\psi_L(mx)\eta'_L(x) - m\psi'_L(mx)\eta_L(x)}$
m	n/n_m (Complex index of refraction of particle / Real index of refraction of surrounding medium)
x	Size parameter
ψ_L	Riccati-Bessel cylindrical function
η_L	Riccati-Bessel cylindrical function
L	Order of the spherical multimode excitation
c	Speed of light in vacuum
R^3	Particle volume
ε_2	Imaginary component of the dielectric function
ε_1	Real component of dielectric function
ε_m	Dielectric function of the surrounding medium
C	Concentration
l	Path length
Hz	Hertz
N/m	Newton / meter
kHz	Kilo Hertz
μN	Micro Newton
$F_{applied}$	Force applied to substrate
V_S	Setpoint Voltage

$\mathbf{V_B}$	Break-away Voltage
S	Sensitivity of the cantilever to bending (V / nm)
$\mathbf{k_{spring}}$	Spring constant
Kα	X-ray emission from electron transition to the K shell
hν	Planck's constant times frequency
W	Watts
Pa	Pascal
pM	Pico molar
$\mathbf{R^2}$	Correlation coefficient
eV	Electron Volts
$\mathbf{\sigma_{Blank}}$	Standard deviation of the blank signal
$\mathbf{K_d}$	Dissociation constant
$\mathbf{K_{ads}}$	Adsorption constant
$\mathbf{Ext_{max}}$	Maximum extinction at saturation coverage
Ext	Extinction
[antigen]	Concentration of antigen

List of Abbreviations

ACSES	Alberta Center for Surface and Engineering Sciences
AFM	Atomic force microscopy
Ag	Silver
$AgNO_3$	Silver nitrate
AgNPs	Silver nanoparticles
Al	Aluminum
Ar	Argon
Asym.	Asymmetric
a.u.	Arbitrary units
Au	Gold
Au-C	Gold-carbon bond
Au-CN	Gold-cyanide bond
$Au(CN)_2^-$	Gold cyanide
$Au_{20}NB$	Nitrobenzene monomer on a 20 gold atom cluster
$Au_{20}NB_3$	Nitrobenzene trimer on a 20 gold atom cluster
Au20vNB	Nitrobenzene monomer bonded to vertex of a 20 gold atom cluster
$Au_{20}vNB_3$	Nitrobenzene trimer bonded to vertex of a 20 gold atom cluster
AuNP	Gold nanoparticle
AuNPs	Gold nanoparticles
AUTS	N-(2-aminoethyl)-11-aminoundecyltrimethoxy silane
BF	Bright field
BF_4^-	Tetrafluoroborate
BP86	Becke-Perdew functional
BSA	Bovine serum albumin
C	Carbon
CH_2	Methylene
CH_3CN	Acetonitrile
Co	Cobalt
COO^-	Carboxylate

Cr	Chromium
Cu	Copper
CVD	Chemical vapor deposition
Deform.	Deformation
DFT	Density functional theory
dNAB	Diazonium salt derived nitroazobenzene
dNB	Diazonium salt derived nitrobenzene
dPAA	Diazonium derived phenylacetic acid
DSP	Dithiobis(succinimidyl propionate)
ECP	Effective core potential
EDC	N-(3-dimethylaminopropyl)-N'-ethylcarbodiimide hydrochloride
ELISA	Enzyme-linked immunosorbent assay
FAT	Fixed analyzer transmission
Fe	Iron
FWHM	Full-width-half-maximum
GaAs	Gallium Arsenide
g-IgG	Goat IgG
GTO	Gaussian-type orbital
H	Hydrogen
HC-dNAB	High concentration of nitroazobenzene
HOPG	Highly ordered pyrolytic graphite
HREELS	High-resolution energy electron loss spectroscopy
H_2SO_4	Sulfuric acid
H_2O_2	Hydrogen peroxide
Ig	Immunoglobulins
IgA	Immunoglobulin A
IgD	Immunoglobulin D
IgE	Immunoglobulin E
IgG	Immunoglobulin G
IgM	Immunoglobulin M
IR	Infrared

IRRAS	Infrared Reflection Absorption Spectroscopy
i.p.	In-plane
LC-dNAB	Low concentration of nitroazobenzene
LOD	Limit of detection
LSPR	Localized surface plasmon resonance
MCT	Mercury-cadmium-telluride
N	Nitrogen
N_2	Molecular nitrogen
NaCl	Sodium chloride
NB	Nitrobenzene
NHS	N-hydroxysuccinimide
Ni	Nickel
NINT	National Institute for Nanotechnology
NO_2	Nitro group
NP	Nanoparticle
NPs	Nanoparticles
O	Oxygen
PBS	Phosphate buffered saline
Pd	Palladium
PPF	Pyrolyzed photoresist
Pt	Platinum
r-AB	Goat affinity purified antibody to rabbit IgG
r-IgG	Rabbit IgG
RMS	Root-mean-square
%RSD	Percent relative standard deviation
SAMs	Self-assembled monolayers
SDD	Stuttgart-Dresden
SEM	Scanning electron microscopy
SERS	Surface enhanced Raman scattering
SHE	Standard hydrogen electrode
Si	Silicon

SPR	Surface plasmon resonance
ssDNA	Single-stranded DNA
Str.	Stretch
$TBABF_4$	Tetrabutylammonium tetrafluoroborate
TEM	Transmission electron microscopy
Ti	Titanium
$t_{16}COOH$	Thiol derived mercaptohexadecanoic acid
tNB	Thiol derived nitrobenzene
UHV	Ultra high vacuum
UV-vis	Ultra violet-visible
wag.	Wagging
XPS	X-ray photoelectron spectroscopy
Zn	Zinc

Chapter 1:

Introduction

1.1 GENERAL OVERVIEW AND RESEARCH OBJECTIVES

There is a constant need to determine both qualitatively and quantitatively the presence of numerous biological molecules in our world today, i.e. food industry, environmental monitoring, and most importantly health care. A major class of these biomolecules includes immunoglobulins (Ig) such as antigens and antibodies, as they are indicators of diseases and infections. The early detection of these immunoglobulins was carried out by radioimmunoassays, in which the presence of an Ig was determined by capturing the analyte of interest on a solid support and exposing it to highly specific radioactive labels for detection.[1, 2] This type of assay produced the capability and sensitivity needed to quantitate immunoglobulins; however, the use of radioactive materials was a health concern, it required expensive equipment and waste disposal was problematic.[3]

In the late 1960s an alternative to radioactive labeling was invented, which was based on the detection of biomolecules by enzyme-linked labels.[4, 5] In this format, the analyte is captured on a solid support and tagged with enzyme-linked labels. An enzyme substrate is then added to the solid support and the enzyme product is measured, which generally involves a color change in the substrate.[6] This assay was consequently named enzyme-linked immunosorbent assay (ELISA). The assay is typically carried out on a microtiter plate, allowing for multiple analyses to be carried out simultaneously. The capability of a small

number of enzymes to catalyze large amounts of substrate has afforded ELISA detection limits in the picomolar range. The high sensitivity, wide applicability to most analytes, and rapid detection have made ELISA the "gold standard" in biomolecule detection.[3, 7] Nevertheless, researchers have investigated other sensing schemes in hopes of simplifying the assay and employing more stable labels. One such alternative replaces the enzyme label with fluorophores exploiting fluorescence detection, but also here drawbacks involving the label are apparent, as fluorophores are susceptible to photobleaching and detection requires expensive instrumentation.[7] The drive towards new labels has been accelerated with the appearance of nanomaterials.

In the past decade there has been an ever-increasing number of scientific reports detailing the modification of nanostructures and their incorporation into bioassays. At the forefront, the application of gold nanoparticles (AuNPs) has continuously received attention, and several reviews are dedicated to these noble metal nanostructures.[8-14] Faraday is credited with the inception of gold nanoparticles into science in 1857, although colloidal gold has been used for centuries in glass staining, providing a ruby-red color.[15] The major driving force behind the use of gold NPs in bio-detection is their unique optical properties resulting from localized surface plasmon resonance (LSPR) effects.[16-18] These effects result in extremely high absorption and scattering of light. The molar extinction coefficients of AuNPs are several orders of magnitude higher than organic dyes and outperform fluorescent molecules as well, thus exhibiting promising applications as labels.[13]

One of the first applications of gold nanoparticles in biomolecule sensing was based on aggregation of AuNPs in solution, which resulted in a color change from red to purple.[7] Mirkin and coworkers pioneered the detection of single-stranded DNA (ssDNA) by employing two sets of gold nanoparticles in solution, each coated with ssDNA.[19-21] A color change of the AuNP solution was observed when the two strands were complementary, as the strands hybridized bringing the NPs in close proximity to each other. Alternatively, if the strands were not complementary, the hybridization was inhibited, and the NP solution color remained red. This detection scheme is capable of sensing picomolar concentrations of ssDNA and is able to discriminate between perfectly matched oligonucleotides and single base-pair mismatches.[7, 14]

In order to improve the sensitivity, Taton et *al.* developed a different set-up for the detection of target ssDNA, employing a conventional flatbed scanner. The target ssDNA was immobilized on a glass substrate and exposed to ssDNA coated gold nanoparticles, which were captured through the DNA hybridization on the glass surface. Then, a solution of silver ions was reduced in the presence of the captured gold nanoparticles resulting in a silver coating around the immobilized NPs. The extend of silver staining was quantitated by a conventional flatbed scanner resulting in low picomolar detection limits for ssDNA.[22] The benefits of inexpensive read-out techniques combined with superior detection limits were promising and have motivated researchers to pursue strategies that incorporate AuNPs in biosensing. This is also the focus of my thesis, which will

contribute twofold: in the field of surface modification of gold nanoparticles, and in the field of immunoassays employing extrinsic AuNP-labels.

This Chapter will introduce the relevant subject areas that are vital to the understanding of the surface modification and the optical properties of AuNPs. One aspect of my work uses a well-studied surface modification of planar substrates *via* diazonium salts and extends this method to gold nanoparticles (Chapter 2 and 3). The diazonium salt derived surface modification has steadily attracted more interest, as a literature search on SciFinder with the keywords "surface modification" and "diazonium salt" reveals close to 200 publications *per annum* in recent years. The diazonium salt chemistry provides a new approach to the modification of AuNPs, thus facilitating more stable adlayer-substrate interactions as discussed throughout this thesis.

The second aspect of my work focuses on an immunoassay design that incorporates gold nanoparticles as labels in a sandwich assay. The detection is based on a simple and commonly available technique: UV-vis spectroscopy. Chapter 4 and 5 are dedicated to this biosensing area. First, the capability of utilizing AuNPs as labels for the detection by UV-vis spectroscopy will be explored, and then the integration in a biochip format will be evaluated. My goal is that the ideas brought forward by this thesis will provide new strategies and insights in the application of nanoscience to biological detection.

1.2 SURFACE MODIFICATION

Nanoparticle modification strategies are typically derived from modification schemes for planar substrates and applied for the surface modification of nanostructures. In this fashion, the knowledge about a well-known system can be applied and extended to the new substrate. Here, the interest lies in the modification of gold nanoparticles with strongly bound films using established techniques to modify planar gold. Two surface chemistries have received significant attention on this substrate: 1) thiol self-assembled monolayers and 2) aryl diazonium salt derived adlayers. Below, the two strategies are reviewed and the benefits and weaknesses of each are highlighted.

1.2.1 Thiol self-assembled monolayers.

One of the most prevalent methods to modify gold is through thiol self-assembled monolayers (SAMs).[23] The sulfur head group of thiols binds to Au while the other end of the molecule, the terminal group, can be tailored to meet a specific surface functionality. The first report on the formation of thiol monolayers dates back to 1983, when Nuzzo and Allara reported on the adsorption of disulfides on gold.[24] Both alkyl and aryl thiols are readily available with numerous chemical functional groups at the terminal end providing the flexibility needed for applications ranging from molecular electronics[25, 26] to biomolecule immobilization.[27, 28] Thiols have also been used to coat a variety of other substrates such as silver, platinum and copper.[23, 27, 29, 30]

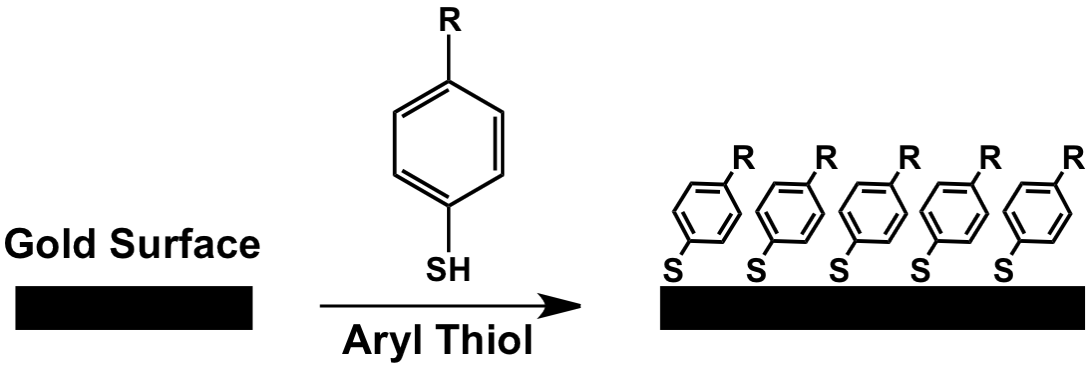

Figure 1.01 Spontaneous self-assembly of aryl thiols on gold forming a well-ordered monolayer.

The benefits of employing thiols to modify gold surfaces include ease of use, reproducible film formation, and wide compatibility due to the flexibility of the terminal group. In Figure 1.01 the formation of an aryl thiolate monolayer is shown schematically on gold. The adsorption process consists of several steps that include diffusion to the surface and re-arrangement into a crystalline film.[27] It is generally understood that thiols and disulfides adsorb to gold as thiolates.[27] Additionally, thiolate films were also demonstrated on gold nanoparticles, both in the application as capping agents during the synthesis of AuNPs and in the modification of preformed AuNPs.[31, 32]

Typically the crystallinity of the adlayer is dependent on the type of thiol used. Long alkanethiols ($C \geq 8$) produce more densely packed, organized structures as van der Waals interactions between the alkyl chains aid monolayer

packing.[33] Further, it was determined that the molecule orientation at the gold surface is typically tilted with respect to the surface normal in order to maximize intermolecular forces.[23, 34] The reported strength of the sulfur-gold interaction, ~50 kcal/mol, is stronger than the interaction between a physisorbed species and Au. However, the sulfur-gold bond is labile enough to allow for surface re-ordering and several studies have shown that thiolate films on gold are prone to oxidation[35-37] and thermal instability at higher temperatures.[27, 38, 39] This instability was one factor which drove the development of alternative surface modification schemes.

1.2.2 Diazonium salt derived films.

An alternate surface chemistry that was later adapted to modify gold was pioneered by Pinson and coworkers in 1992 and involved the modification of carbon substrates with aryl diazonium salts.[40] The motivation behind the early work was to find a modification strategy for carbon electrodes that formed stable yet versatile adlayers.[40] It was later determined that this chemistry resulted in the formation of a covalent C-C bond on carbon substrates such as glassy carbon,[41, 42] highly ordered pyrolytic graphite (HOPG),[41, 43, 44] and pyrolyzed photoresist films (PPF).[45] The accepted mechanism involves the reduction of the diazonium ion by an external potential forming an aryl radical intermediate in close proximity to the conductive substrate.[46] This radical intermediate then binds to the surface forming the initial film. Further, it is also possible *via* an excess of aryl radical intermediates to attack already attached molecules on the surface thereby forming

multilayers.[43, 47] It was also shown that this surface chemistry could be extended to other substrates, i.e. Si,[48, 49] GaAs,[48] Fe,[50] Cu,[49, 51, 52] Pd,[48] Pt,[46, 52] Ag,[53] Zn,[52] Co,[52] Ni,[52] Ti,[54] and Au.[49, 52, 55] Studies on iron and copper surfaces have provided direct evidence for the formation of a covalently bond.[50, 51, 56] In addition, stability studies on a number of substrates modified by diazonium reduction have shown excellent resistance to adverse conditions.[39, 54, 57, 58]

The grafting of diazonium salts was initially carried out by the application of an external potential, but in recent years the electroless or spontaneous deposition was demonstrated.[51, 59-63] It is hypothesized that a substrate with enough reducing potential provides the electrons necessary for the spontaneous reduction of the aryl diazonium cation *via* a redox reaction.[62] Figure 1.02 depicts the spontaneous formation of a diazonium salt derived film on gold. In the first step aryl radicals are produced near the surface of the substrate. These highly reactive radicals then bind to the substrate (2) and additional radicals attack already bound molecules forming multilayers (3). Before the work presented here, the nature of the gold-aryl interaction was unknown. The extent of multilayer formation can be controlled by factors such as diazonium salt concentration and exposure time. However, adlayer reproducibility is not on par with SAMs. The possibilities of physisorbed dimers[64] and azo-linkages[64] among aryl groups or aryl groups and substrate have been omitted in Figure 1.02 for clarity. The R-group in Figure 1.02 indicates the possibility for a variety of different functionalities that can be attached to the ring providing flexibility. The electroless grafting opened a pathway for the modification of nanostructures motivated by the potential for a

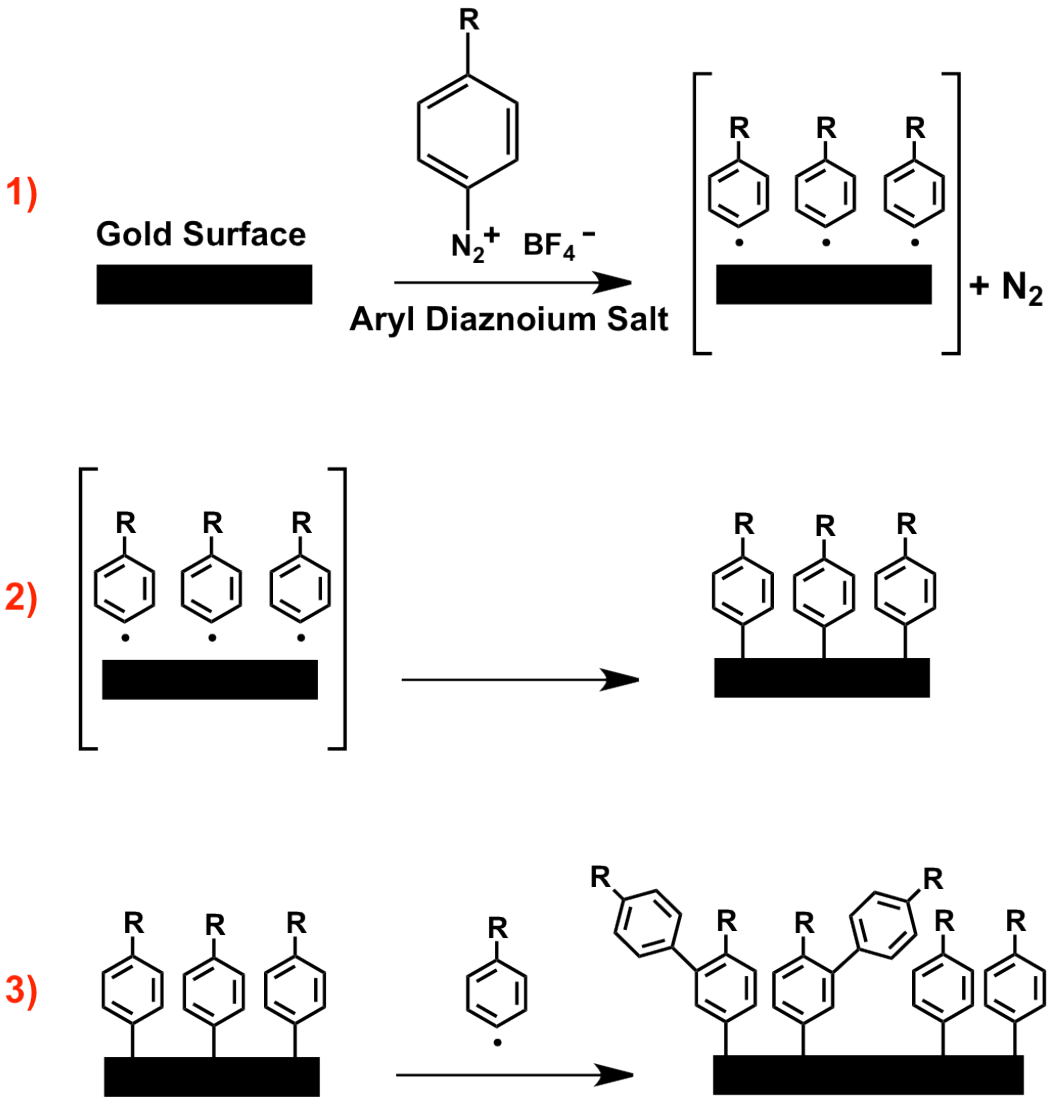

Figure 1.02 Schematic showing the spontaneous reduction of an aryl diazonium cation at a gold surface resulting in a multilayered film with the loss of molecular nitrogen.

strong adlayer-substrate interaction.[65-70] Although the bonding has been elucidated for a majority of substrates, the exact nature of the adsorption on gold is still under investigation and in Chapter 2 strong evidence for the formation of a covalent carbon-gold bond will be presented.

1.3 PROTEIN CHEMISTRY AND BIOASSAY TECHNIQUES

The detection of biomolecules is a vast research area that spans across several disciplines ranging from medicine to analytical chemistry.[71, 72] The work presented in this thesis is focused on immunoassays.[73, 74] Immunoassays employ antibodies to recognize and bind an analyte. Antibodies are a class of proteins called immunoglobulins. This class of molecules present in living organisms finds its importance in recognizing and fighting foreign invaders.[75] Immunoglobulins exist in different classes (IgA, IgD, IgE, IgG, and IgM) depending on their function. Antibodies circulate in the blood stream and recognize a certain substructure on a foreign target called an antigen. The binding is highly selective and this specificity is fundamental to immunoassays.[75] The structure of an immunoglobulin G is shown in Figure 1.03 exhibiting a "Y-shape". The IgG consists of a constant region (the stem) and a variable region (the forks). In the constant region only heavy chains are found and these heavy chains determine the class of immunoglobulin. On the other hand, the variable region contains both heavy and light chains that act in unison to form the recognition site for a specific antigen.[76] An IgG molecule can bind up to two antigens and is generally 150 kDa in size.

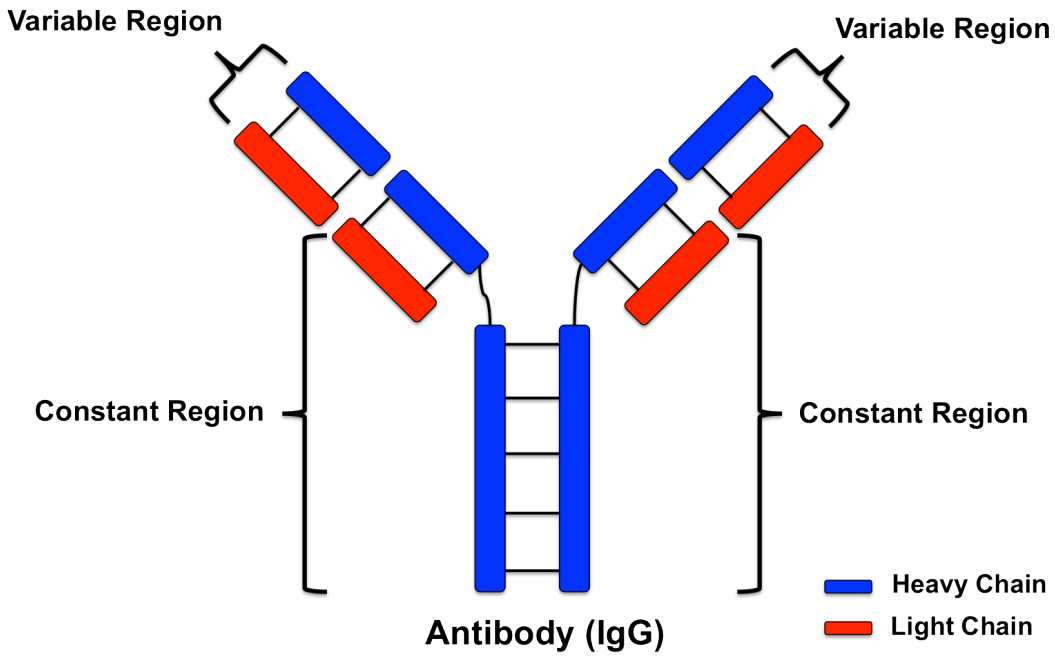

Figure 1.03 Schematic of an IgG antibody structure containing the constant region in the "stem" and the variable region in the "forks". The heavy and light chains are indicated by the colors blue and red, respectively.

In immunoassays the antibody is usually immobilized on a solid support, which then is exposed to a solution containing the target antigen. This antibody immobilization can create assay performance problems as the antibody orientation determines its capability to capture antigens from solution.[77] A random orientation can lead to a reduced capture-agent activity on the biochip (20-50%) as opposed to a perfectly oriented antibody layer.[77] Other factors that could affect antibody

activity include denaturation, which could result from conformational changes as the IgG is immobilized on the biochip surface.[78]

There are several immunoassay techniques presently used in the detection of the antibody-antigen binding, such as enzyme-linked immunosorbent assay (ELISA),[79, 80] fluorescence,[81, 82] and surface plasmon resonance (SPR).[83, 84] These techniques can generally be separated into two groups based on the requirement for an external label in the detection of the analyte of interest: label-free and labeled. SPR is a label-free technique and the majority of other techniques require labels such as enzymes in ELISA or fluorophores in fluorescence-based detection. Label-free techniques offer the advantage of requiring fewer steps/reagents in order to detect binding. However, label-free strictly relies on the specificity of the capture surface and can be prone to false positives. A label brings in a second layer of specificity.

Both label-free and labeled avenues have received significant attention with the incorporation of nanostructures in biosensing. Gold nanoparticles, in particular, exhibit a unique optical property called localized surface plasmon resonance (LSPR) that can be utilized in a label-free sensing-format analogues to SPR,[85] and AuNPs have provided a new method for generating labels in sandwich immunoassays based on surface enhanced Raman scattering (SERS) detection.[86] In the following sections selective assays will be described that are relevant to this thesis and provide the foundation of the work presented in Chapter 4 and 5.

1.3.1 UV-vis spectroscopy of AuNPs in biosensing.

A more detailed treatment of the phenomena associated with AuNPs will be presented in Chapter 4 and only the applicable properties for the techniques presented will be discussed here. Gold nanoparticles exhibit an intense absorption band in the visible region of the spectrum. This phenomenon is called LSPR and results from the collective excitation of conduction electrons in the nanoparticle.[13] The LSPR band position (λ_{max}) is sensitive to changes in the refractive indices of the NP surface and the surrounding medium.[85, 87, 88] This sensitivity is used in LSPR sensing designs that typically consist of a AuNP layer adsorbed on a transparent support, which then is exposed to a target analyte that binds to the surface of the nanoparticle resulting in a λ_{max} shift. The important requirement in this design is careful control of the gold nanoparticle surface chemistry to specifically capture analyte molecules from solution while preventing non-specific binding. A binding event changes the refractive index of the NP surface and typically red-shifts λ_{max}. The shift in the LSPR band can be calculated by equation 1-01 as shown by Van Duyne.[85, 89, 90]

$$\Delta\lambda \approx m(n_{adsorbate} + n_{medium})\left(1 - e^{-2d/l_d}\right) \qquad (1\text{-}01)$$

Here, $\Delta\lambda$ is the wavelength shift, m is the sensitivity factor (nm/refractive index units), n refers to the refractive index of either the adsorbate or the surrounding medium, d is the adsorbate layer thickness (nm) and l_d is the electromagnetic field decay length (nm). Figure 1.04 shows an immunoassay LSPR sensor design, in which the nanoparticle surface has been modified with an antibody that then

captures the target analyte, an antigen, from solution. The binding of the analyte red-shifts the absorption band as shown in the UV-vis spectrum in Figure 1.04.

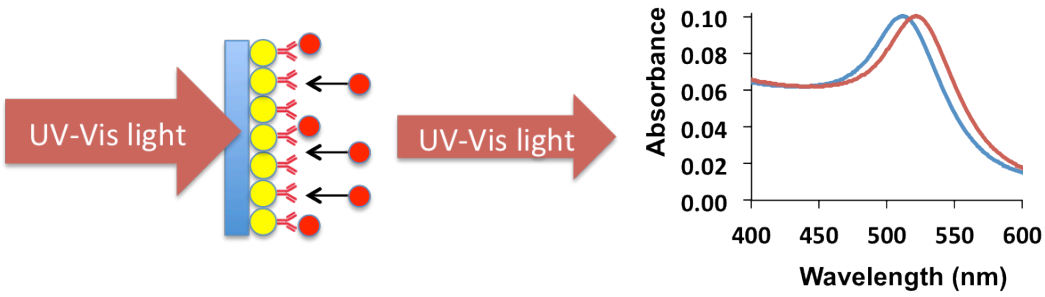

Figure 1.04. An illustration of an immunoassay LSPR sensor-design: a layer of antibody coated gold nanoparticles is immobilized on a transparent substrate and used to bind antigens from solution. The antigen binding results in a shift of the LSPR absorption band.

In a similar format several researcher have employed gold nanoparticle constructs to detect biotin-streptavidin binding[91] and a variety of different immunoglobulin G's (IgG's).[92-95] This detection method can also be extended to silver nanoparticles (AgNPs) as they exhibit the same phenomenon with the exception that the silver LSPR band is located at a higher frequency.[96-98] Lastly, other nanostructures such as silver nanoprisms[99, 100] and gold nanorods[101, 102] have also been utilized in this fashion. Technological advancements in instrumentation have made it possible to detect wavelength shifts as small as 0.0005 nm making

LSPR based methods highly sensitive.[85] Detection limits in the low picomolar range are readily obtainable and the drive towards single nanoparticle/molecule detection is underway.[103] However, sophisticated instrumentation is needed to achieve these low detection limits and the measurement can be prone to subtle changes in solvent composition, resulting in false positives. One significant drawback of this detection method is the inability of multiplexing. The capture layer on the solid support has to be the identical throughout and thus can only bind one specific analyte at a time. Therefore a different approach was explored in this thesis that measures the magnitude of the LSPR band. In order for such a measurement to relay information about analyte concentrations the entire set-up had to be changed. The next Section will present a sandwich assay design, which will be used in conjunction with UV-vis spectroscopy in this thesis.

1.3.2 Surface enhanced Raman scattering (SERS) in biosensing.

Another bioassay design that exploits gold nanoparticles is based on surface-enhanced Raman scattering (SERS). Metal nanoparticles can enhance the Raman signal by both chemical and electromagnetic effects creating the basis for SERS. The chemical enhancement only accounts for a small portion, ~10^2, of the overall enhancement and involves a charge transfer state between the NP and the adsorbent.[104] The majority of the signal improvement results from the localized surface plasmon resonance coupling occurring at the nanoparticle surface when irradiated by light, which can lead to signal enhancements on the order of 10^{14} for single molecules.[86, 105] Other benefits of SERS include narrow spectral

bandwidths allowing to differentiate closely related compounds and the capability for signal averaging as photobleaching is minimal. The signal enhancement coupled with the other advantages of SERS rival techniques such as fluorescence.[106]

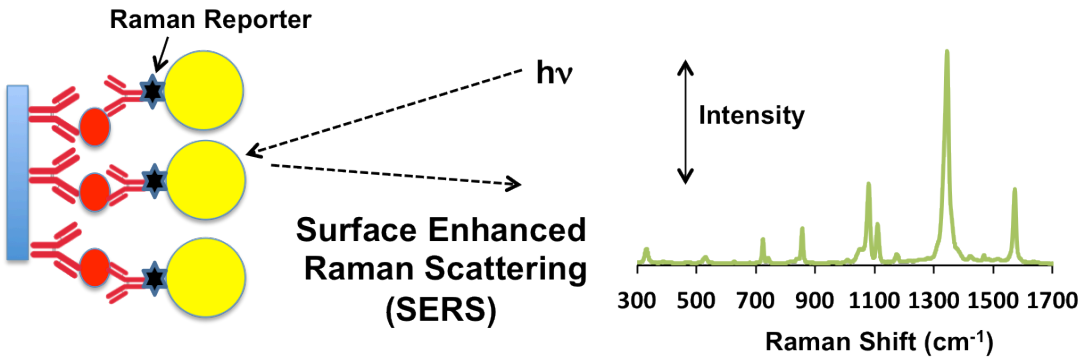

Figure 1.05 A sandwich immunoassay that "sandwiches" the analyte (antigen) between a capture-molecule (antibody) and an antibody coated gold nanoparticle. The AuNP also carries a Raman active molecule (Raman reporter) that is used in the SERS detection of the analyte. This Raman reporter generates the SERS spectrum shown to the right.

The incorporation of SERS in an immunoassay was first demonstrated by Rohr and coworkers in 1989 with a roughened silver film to achieve SERS.[107] A decade later in 1999 Porter and his research group presented the first sandwich immunoassay that utilized gold nanoparticles in SERS detection.[31] The assay was

capable of detecting rabbit and rat IgG at the nanomolar level. Figure 1.05 introduces the sandwich immunoassay format that "sandwiches" the analyte of interest between an immobilized capture-molecule on a solid support and a functionalized nanoparticle label. The gold nanoparticle is bifunctional, carrying a capture-molecule to selectively bind to the analyte and a Raman active molecule (Raman reporter) that will be used in the detection strategy. The SERS response from the Raman reporter is measured and correlated to the analyte concentration.

Several aspects of the sandwich immunoassay have to be carefully controlled to achieve quantitative and reproducible results.[86] The solid support chosen is most often planar gold, which can lead to plasmonic coupling between the gold surface and the AuNPs. The electromagnetic coupling of the two plasmons leads to a shift in the LSPR band of the gold nanoparticle thereby affecting the electromagnetic enhancement of the Raman bands. In order to minimize variations in signal intensity, the solid support has to be manufactured with a low batch-to-batch variability. Even more important are gold nanoparticle size variations and stability as discussed below.

The SERS enhancement for AuNPs is size dependent and variations in nanoparticle diameter affect the overall intensity of the SERS signal.[86] The stability of the coated AuNPs is the other factor that needs to be stringently controlled. The NP surface needs to be designed in such as way that it prevents aggregation by maintaining a slightly negative or positive surface charge to cause electrostatic repulsion.[86] Further, the antibody needs to be covalently linked to the surface to prevent desorption during the assay, which could lead to a reduction in

signal.[108] Here a bifunctional thiol is used that coats the gold surface and carries a reactive succinimidyl ester functionality that reacts with primary amines on the antibody forming an amide linkage.[108, 109] Another aspect is non-specific binding either as a result of the capture layer on the solid support or from the gold nanoparticle. This can generally be prevented by exposing the modified surface to blocking agents such as bovine serum albumin (BSA).[110, 111] Blocking agents are typically smaller proteins that can bind to the surface between antibodies, thus covering the remainder of the surface and preventing any non-specific interactions.

A carefully controlled surface chemistry and a uniform gold nanoparticle size distribution can lead to detection limits in the femtomolar range, as was shown for both IgG's and viral pathogens.[108, 112, 113] Not only does this method provide superior detection limits, it also has the capability of multiplexing by employing different Raman reporter molecules for each type of analyte NP-label.[114]

1.4. MOTIVATIONS AND INTENTIONS

The drive towards stable yet versatile gold nanoparticles was the motivation behind Chapter 2 and the goal was to make use of strong adlayer–substrate interactions while maintaining a simple modification procedure. The spontaneous reduction of diazonium salts met these requirements on planar gold and much of the work presented in Chapter 2 will focus on applying this chemistry to AuNPs. Chapter 3 serves as an extension to the previous chapter and

is meant to provide a better understanding of the diazonium derived film on gold nanoparticles and investigate possible applications.

In the biosensing area, the motivation was to design a simple and readily available detection method that will have the potential to analyze at least 2 analytes simultaneously. This idea is explored in Chapter 4 and applied to an immunoassay in Chapter 5. Although Raman spectrometers have become more affordable in recent years, they are still not present in a majority of analytical laboratories. UV-vis spectrophotometers, on the other hand, are widely employed and significantly less expensive. Therefore, we have combined certain aspects of both techniques and developed a sandwich immunoassay with AuNP-labels similar to the SERS assay shown in Figure 1.05. The detection, however, relies on the LSPR band intensity measured by a common benchtop UV-vis spectrophotometer. The magnitude of the LSPR band, which scales with the number of nanoparticles present, is used instead of the LSPR shift to facilitate the potential for multiplexing by employing other labels such as silver nanoparticles.

1.5 REFERENCES

1. Berson, S. A.; Yalow, R. S.; Bauman, A.; Rothschild, M. A.; Newerly, K. *J. Clin. Invest.* **1956,** 35, (2), 170-190.
2. Yalow, R. S.; Berson, S. A. *J. Clin. Invest.* **1960,** 39, (7), 1157-1175.
3. Lequin, R. M. *Clin. Chem.* **2005,** 51, (12), 2415-2418.
4. Engvall, E.; Perlmann, P. *Immunochemistry* **1971,** 8, (9), 871-&.
5. Vanweeme.Bk; Schuurs, A. H. W. *Febs. Lett.* **1971,** 15, (3), 232-&.
6. Voller, A.; Bartlett, A.; Bidwell, D. E. *J. Clin. Pathol.* **1978,** 31, (6), 507-520.
7. Rosi, N. L.; Mirkin, C. A. *Chem. Rev.* **2005,** 105, (4), 1547-1562.
8. Shipway, A. N.; Katz, E.; Willner, I. *Chemphyschem* **2000,** 1, (1), 18-52.
9. Katz, E.; Willner, I. *Angew. Chem. Int. Edit.* **2004,** 43, (45), 6042-6108.
10. Daniel, M. C.; Astruc, D. *Chem. Rev.* **2004,** 104, (1), 293-346.
11. Algar, W. R.; Prasuhn, D. E.; Stewart, M. H.; Jennings, T. L.; Blanco-Canosa, J. B.; Dawson, P. E.; Medintz, I. L. *Bioconjugate Chem.* **2011,** 22, (5), 825-858.
12. Zamborini, F. P.; Bao, L. L.; Dasari, R. *Anal. Chem.* **2012,** 84, (2), 541-576.
13. Saha, K.; Agasti, S. S.; Kim, C.; Li, X.; Rotello, V. M. *Chem. Rev.* **2012**.
14. Jans, H.; Huo, Q. *Chem. Soc. Rev.* **2012,** 41, (7), 2849-2866.
15. Faraday, M. **1857,** 147, 145-181.
16. Mie, G. *Ann. Phys.* **1908,** 25, (3), 377-445.

17. Van der Hulst, H. C., *Light Scattering by Small Metal Particles*. Wiley: New York, 1957.

18. Bohren, C. F.; Huffman, D. R., *Absorption of Light by Small Particles*. Wiley: New York, 1983.

19. Mirkin, C. A.; Letsinger, R. L.; Mucic, R. C.; Storhoff, J. J. *Nature* **1996,** 382, (6592), 607-609.

20. Elghanian, R.; Storhoff, J. J.; Mucic, R. C.; Letsinger, R. L.; Mirkin, C. A. *Science* **1997,** 277, (5329), 1078-1081.

21. Storhoff, J. J.; Elghanian, R.; Mucic, R. C.; Mirkin, C. A.; Letsinger, R. L. *J. Am. Chem. Soc.* **1998,** 120, (9), 1959-1964.

22. Taton, T. A.; Mirkin, C. A.; Letsinger, R. L. *Science* **2000,** 289, (5485), 1757-1760.

23. Love, J. C.; Estroff, L. A.; Kriebel, J. K.; Nuzzo, R. G.; Whitesides, G. M. *Chem. Rev.* **2005,** 105, (4), 1103-1169.

24. Nuzzo, R. G.; Allara, D. L. *J. Am. Chem. Soc.* **1983,** 105, (13), 4481-4483.

25. Bumm, L. A.; Arnold, J. J.; Cygan, M. T.; Dunbar, T. D.; Burgin, T. P.; Jones, L.; Allara, D. L.; Tour, J. M.; Weiss, P. S. *Science* **1996,** 271, (5256), 1705-1707.

26. Tour, J. M. *Acc. Chem. Res.* **2000,** 33, (11), 791-804.

27. Vericat, C.; Vela, M. E.; Benitez, G.; Carro, P.; Salvarezza, R. C. *Chem. Soc. Rev.* **2010,** 39, (5), 1805-1834.

28. Bonanni, B.; Bizzarri, A. R.; Cannistraro, S. *J. Phys. Chem. B* **2006,** 110, (30), 14574-14580.

29. Laibinis, P. E.; Whitesides, G. M.; Allara, D. L.; Tao, Y. T.; Parikh, A. N.; Nuzzo, R. G. *J. Am. Chem. Soc.* **1991,** 113, (19), 7152-7167.

30. Walczak, M. M.; Chung, C.; Stole, S. M.; Widrig, C. A.; Porter, M. D. *J. Am. Chem. Soc.* **1991,** 113, (7), 2370-2378.

31. Ni, J.; Lipert, R. J.; Dawson, G. B.; Porter, M. D. *Anal. Chem.* **1999,** 71, (21), 4903-4908.

32. Weisbecker, C. S.; Merritt, M. V.; Whitesides, G. M. *Langmuir* **1996,** 12, (16), 3763-3772.

33. Porter, M. D.; Bright, T. B.; Allara, D. L.; Chidsey, C. E. D. *J. Am. Chem. Soc.* **1987,** 109, (12), 3559-3568.

34. Frey, S.; Stadler, V.; Heister, K.; Eck, W.; Zharnikov, M.; Grunze, M.; Zeysing, B.; Terfort, A. *Langmuir* **2001,** 17, (8), 2408-2415.

35. Cooper, E.; Leggett, G. J. *Langmuir* **1998,** 14, (17), 4795-4801.

36. Huang, J. Y.; Hemminger, J. C. *J. Am. Chem. Soc.* **1993,** 115, (8), 3342-3343.

37. Norrod, K. L.; Rowlen, K. L. *J. Am. Chem. Soc.* **1998,** 120, (11), 2656-2657.

38. Delamarche, E.; Michel, B.; Kang, H.; Gerber, C. *Langmuir* **1994,** 10, (11), 4103-4108.

39. Shewchuk, D. M.; McDermott, M. T. *Langmuir* **2009,** 25, (8), 4556-4563.

40. Delamar, M.; Hitmi, R.; Pinson, J.; Saveant, J. M. *J. Am. Chem. Soc.* **1992,** 114, (14), 5883-5884.

41. Allongue, P.; Delamar, M.; Desbat, B.; Fagebaume, O.; Hitmi, R.; Pinson, J.; Saveant, J. M. *J. Am. Chem. Soc.* **1997,** 119, (1), 201-207.

42. Delamar, M.; Desarmot, G.; Fagebaume, O.; Hitmi, R.; Pinson, J.; Saveant, J. M. *Carbon* **1997,** 35, (6), 801-807.

43. Kariuki, J. K.; McDermott, M. T. *Langmuir* **2001,** 17, (19), 5947-5951.

44. Liu, Y. C.; Mccreery, R. L. *J. Am. Chem. Soc.* **1995,** 117, (45), 11254-11259.

45. Anariba, F.; DuVall, S. H.; McCreery, R. L. *Anal. Chem.* **2003,** 75, (15), 3837-3844.

46. Pinson, J.; Podvorica, F. *Chem. Soc. Rev.* **2005,** 34, (5), 429-439.

47. Kariuki, J. K.; McDermott, M. T. *Langmuir* **1999,** 15, (19), 6534-6540.

48. Stewart, M. P.; Maya, F.; Kosynkin, D. V.; Dirk, S. M.; Stapleton, J. J.; McGuiness, C. L.; Allara, D. L.; Tour, J. M. *J. Am. Chem. Soc.* **2004,** 126, (1), 370-378.

49. Combellas, C.; Kanoufi, F.; Pinson, J.; Podvorica, F. I. *J. Am. Chem. Soc.* **2008,** 130, (27), 8576-+.

50. Boukerma, K.; Chehimi, M. M.; Pinson, J.; Blomfield, C. *Langmuir* **2003,** 19, (15), 6333-6335.

51. Hurley, B. L.; McCreery, R. L. *J. Electrochem. Soc.* **2004,** 151, (5), B252-B259.

52. Bernard, M.-C.; Chaussé, A.; Cabet-Deliry, E.; Chehimi, M. M.; Pinson, J.; Podvorica, F.; Vautrin-Ul, C. *Chem. Mat.* **2003,** 15, (18), 3450-3462.

53. Liang, H. H.; Tian, H.; McCreery, R. L. *Appl. Spectrosc.* **2007,** 61, (6), 613-620.

54. Mahmoud, A. M.; Bergren, A. J.; McCreery, R. L. *Anal. Chem.* **2009,** 81, (16), 6972-6980.

55. Laforgue, A.; Addou, T.; Bélanger, D. *Lagmuir* **2005,** 21, (15), 6855-6865.

56. Adenier, A.; Bernard, M.-C.; Chehimi, M. M.; Cabet-Deliry, E.; Desbat, B.; Fagebaume, O.; Pinson, J.; Podvorica, F. *J. Am. Chem. Soc.* **2001,** 123, (19), 4541-4549.

57. Mahmoud, A. M.; Bergren, A. J.; Pekas, N.; McCreery, R. L. *Adv. Funct. Mater.* **2011,** 21, (12), 2273-2281.

58. Paulik, M. G.; Brooksby, P. A.; Abell, A. D.; Downard, A. J. *J. Phys. Chem. C* **2007,** 111, (21), 7808-7815.

59. Lehr, J.; Williamson, B. E.; Flavel, B. S.; Downard, A. J. *Langmuir* **2009,** 25, (23), 13503-13509.

60. Adenier, A.; Barre, N.; Cabet-Deliry, E.; Chausse, A.; Griveau, S.; Mercier, F.; Pinson, J.; Vautrin-Ul, C. *Surf. Sci.* **2006,** 600, (21), 4801-4812.

61. Dyke, C. A.; Tour, J. M. *Nano Lett.* **2003,** 3, (9), 1215-1218.

62. Adenier, A.; Barré, N.; Cabet-Deliry, E.; Chaussé, A.; Griveau, S.; Mercier, F.; Pinson, J.; Vautrin-Ul, C. *Surf. Sci.* **2006,** 600, (21), 4801-4812.

63. Chamoulaud, G.; Bélanger, D. *J. Phys. Chem. C* **2007,** 111, (20), 7501-7507.

64. Mahouche-Chergui, S.; Gam-Derouich, S.; Mangeney, C.; Chehimi, M. M. *Chem. Soc. Rev.* **2011,** 40, (7), 4143-4166.

65. Collins, G.; Fleming, P.; O'Dwyer, C.; Morris, M. A.; Holmes, J. D. *Chem. Mater.* **2011,** 23, (7), 1883-1891.

66. Matrab, T.; Chancolon, J.; L'hermite, M. M.; Rouzaud, J. N.; Deniau, G.; Boudou, J. P.; Chehimi, M. M.; Delamar, M. *Colloids Surf. A* **2006,** 287, (1-3), 217-221.

67. Bahr, J. L.; Yang, J. P.; Kosynkin, D. V.; Bronikowski, M. J.; Smalley, R. E.; Tour, J. M. *J. Am. Chem. Soc.* **2001,** 123, (27), 6536-6542.

68. Mirkhalaf, F.; Schiffrin, D. J. *Langmuir* **2010,** 26, (18), 14995-15001.

69. Ghosh, D.; Chen, S. W. *J. Mater. Chem.* **2008,** 18, (7), 755-762.

70. Mangeney, C.; Qin, Z.; Dahoumane, S. A.; Adenier, A.; Herbst, F.; Boudou, J. P.; Pinson, J.; Chehimi, M. M. *Diam. Relat. Mater.* **2008,** 17, (11), 1881-1887.

71. Wagner, G. *ChemMedChem* **2010,** 5, (6), 961-962.

72. Wu, G., *Assay Development: Fundamentals and Practices*. John Wiley & Sons, Inc.: New Jersey, 2010.

73. Diamandis, E. P.; Christopoulos, T. K., *Immunoassay*. Academic Press: San Diego, 1996.

74. Andrade, J.; Hlady, V., *Protein adsorption and materials biocompatibility: A tutorial review and suggested hypotheses*. Springer: Heidelberg, 1986.

75. Janeway, C. A.; Jr, P. T.; Walport, M.; Shlomchik, M. J., *Immunobiology*. 5 ed.; Garland Science: New York, 2001.

76. Schulz, G. E.; Schirmer, R. H., *Principles of Protein Structure*. Springer: New York, 1979.

77. Lu, B.; Smyth, M. R.; OKennedy, R. *Analyst* **1996,** 121, (3), R29-R32.

78. Fang, F.; Szleifer, I. *Biophys. J.* **2001,** 80, (6), 2568-2589.

79. Porstmann, T.; Kiessig, S. T. *J. Immunol. Methods* **1992,** 150, (1-2), 5-21.

80. Self, C. H.; Cook, D. B. *Curr. Opin. Biotech.* **1996,** 7, (1), 60-65.

81. MacBeath, G.; Schreiber, S. L. *Science* **2000,** 289, (5485), 1760-1763.

82. Sapsford, K. E.; Charles, P. T.; Patterson, C. H.; Ligler, F. S. *Anal. Chem.* **2002,** 74, (5), 1061-1068.

83. Kanda, V.; Kariuki, J. K.; Harrison, D. J.; McDermott, M. T. *Anal. Chem.* **2004,** 76, (24), 7257-7262.

84. Smith, E. A.; Corn, R. M. *Appl. Spectrosc.* **2003,** 57, (11), 320A-332A.

85. Anker, J. N.; Hall, W. P.; Lyandres, O.; Shah, N. C.; Zhao, J.; Van Duyne, R. P. *Nat. Mater.* **2008,** 7, (6), 442-453.

86. Porter, M. D.; Lipert, R. J.; Siperko, L. M.; Wang, G.; Narayanana, R. *Chem. Soc. Rev.* **2008,** 37, (5), 1001-1011.

87. Kelly, K. L.; Coronado, E.; Zhao, L. L.; Schatz, G. C. *J. Phys. Chem. B* **2003,** 107, (3), 668-677.

88. Mulvaney, P. *Langmuir* **1996,** 12, (3), 788-800.

89. Lopatynskyi, A. M.; Lopatynska, O. G.; Guo, L. J.; Chegel, V. I. *IEEE Sens. J.* **2011,** 11, (2), 361-369.

90. Willets, K. A.; Van Duyne, R. P. *Annu. Rev. Phys. Chem.* **2007,** 58, 267-297.

91. Nath, N.; Chilkoti, A. *Anal. Chem.* **2004,** 76, (18), 5370-5378.

92. Englebienne, P. *Analyst* **1998,** 123, (7), 1599-1603.

93. Dahint, R.; Trileva, E.; Acumnan, H.; Konrad, U.; Zimmer, M.; Stadler, V.; Himmelhaus, M. *Biosens. Bioelectron.* **2007,** 22, (12), 3174-3181.

94. Shao, Y. L.; Xu, S. P.; Zheng, X. L.; Wang, Y.; Xu, W. Q. *Sensors-Basel* **2010,** 10, (4), 3585-3596.

95. Woo, J. R.; Lim, D. K.; Nam, J. M. *Small* **2011,** 7, (5), 648-655.

96. Chen, Y. Q.; Lu, C. J. *Sens. Actuators, B* **2009,** 135, (2), 492-498.

97. Haes, A. J.; Van Duyne, R. P. *J. Am. Chem. Soc.* **2002,** 124, (35), 10596-10604.

98. McFarland, A. D.; Van Duyne, R. P. *Nano Lett.* **2003,** 3, (8), 1057-1062.

99. Evanoff, D. D.; Chumanov, G. *Chemphyschem* **2005,** 6, (7), 1221-1231.

100. Hall, W. P.; Ngatia, S. N.; Van Duyne, R. P. *J. Phys. Chem. C* **2011,** 115, (5), 1410-1414.

101. Yu, C. X.; Irudayaraj, J. *Anal. Chem.* **2007,** 79, (2), 572-579.

102. Marinakos, S. M.; Chen, S. H.; Chilkoti, A. *Anal. Chem.* **2007,** 79, (14), 5278-5283.

103. Ament, I.; Prasad, J.; Henkel, A.; Schmachtel, S.; Sonnichsen, C. *Nano Lett.* **2012,** 12, (2), 1092-1095.

104. McFarland, A. D.; Young, M. A.; Dieringer, J. A.; Van Duyne, R. P. *J. Phys. Chem. B* **2005,** 109, (22), 11279-11285.

105. Dieringer, J. A.; Lettan, R. B.; Scheidt, K. A.; Van Duyne, R. P. *J. Am. Chem. Soc.* **2007,** 129, (51), 16249-16256.

106. Kneipp, K.; Kneipp, H.; Manoharan, R.; Hanlon, E. B.; Itzkan, I.; Dasari, R. R.; Feld, M. S. *Appl. Spectrosc.* **1998,** 52, (12), 1493-1497.

107. Rohr, T. E.; Cotton, T.; Fan, N.; Tarcha, P. J. *Anal. Biochem.* **1989,** 182, (2), 388-398.

108. Grubisha, D. S.; Lipert, R. J.; Park, H. Y.; Driskell, J.; Porter, M. D. *Anal. Chem.* **2003,** 75, (21), 5936-5943.

109. Wagner, P.; Hegner, M.; Kernen, P.; Zaugg, F.; Semenza, G. *Biophys. J.* **1996,** 70, (5), 2052-2066.

110. Steinitz, M. *Anal. Biochem.* **2000,** 282, (2), 232-238.

111. Maggio, E. T., *Enzyme Immunoassay*. CRC Press: Boca Raton, FL, 1980.

112. Driskell, J. D.; Kwarta, K. M.; Lipert, R. J.; Porter, M. D.; Neill, J. D.; Ridpath, J. F. *Anal. Chem.* **2005,** 77, (19), 6147-6154.

113. Driskell, J. D.; Uhlenkamp, J. M.; Lipert, R. J.; Porter, M. D. *Anal. Chem.* **2007,** 79, (11), 4141-4148.

114. Wang, G. F.; Park, H. Y.; Lipert, R. J. *Anal. Chem.* **2009,** 81, (23), 9643-9650.

Chapter 2:

Diazonium Derived Aryl Films on Gold Nanoparticles: Evidence for a Carbon-Gold Covalent Bond*

2.1 INTRODUCTION

Methods to functionalize nanoparticles are generally derived from schemes used for modifying macroscopic, planar substrates. The interaction between a substrate and adsorbate layer often controls the structure and properties of the layer and governs the types of applications for which the modified substrate can be employed. Covalent bonding between organic molecules and substrates such as silicon,[1] glass[2] and carbon[3] are known. Electrochemical methods are used to chemically graft polymers to metal surfaces,[4] but in general, organic molecules covalently bound to metals are less prevalent. Organic molecular layers on noble metal surfaces have been used in a wide range of applications. The self-assembly of alkythiolate monolayers is the most broadly applied modification method for noble metals such as gold.[5, 6] The monolayers are easily formed, are highly organized and provide a pathway to create interfaces with a variety of functional groups. The interaction between the sulfur and gold is labile, which allows for the self-organization of this monolayer system but can also lead to instability under certain conditions.[6] Despite the labile nature of the interaction, thiol derived

* **A version of this chapter has been published. Adapted with permission from (Laurentius *et al.*, 2011, *ACS Nano*, 5(5), 4219-4227).**

monolayers on gold are sufficiently stable to be widely applied in fundamental studies, biosensing, molecular electronics and surface patterning.[5]

The modification of conducting surfaces with diazonium salt derived aryl layers gained significant attention.[3, 7] Diazonium salts are electrochemically or spontaneously reduced at the surface of a conductor to form an aryl radical that binds to the surface. These films tend to form multilayers and are relatively disordered.[8, 9] The interaction between diazonium derived aryl films and the substrate is very stable, able to withstand prolonged ultrasonic treatment, boiling in various solvents and long time exposure to ambient conditions.[7] It is widely accepted that the interaction between diazonium derived films and graphitic carbon substrates is a C-C covalent bond. This is supported by Raman spectroscopic evidence[10] and more recently by fragmentation patterns observed in time-of-flight secondary ion mass spectrometry experiments.[11] The bonding of diazonium-derived films on metal surfaces has been studied. Angle resolved X-ray photoelectron spectroscopy (XPS) revealed the presence of a carbide layer at an aryl-Fe interface, suggesting a covalent bond on Fe.[12] Highly stable films have been reported on Cu surfaces and XPS results indicated the presence of both Cu-O-C and Cu-C bonds.[13]

Several groups have reported on the formation of aryl films on gold surfaces *via* the reduction of diazonium salts.[14-19] The structure and stability of electrochemically deposited films are similar to those formed on carbon. Shewchuk and McDermott have shown that diazonium derived nitrobenzene (dNB) films are more strongly bonded to gold surfaces than the thiol analog.[19]

Downard and co-workers have recently examined the formation of diazonium-derived layers on gold by spontaneous (open-circuit) adsorption.[20] It was shown that the growth of nitrobenzene films was dependent on incubation time and films ranging from a sub-monolayer to multilayers consisting of 2-3 layers were observed.

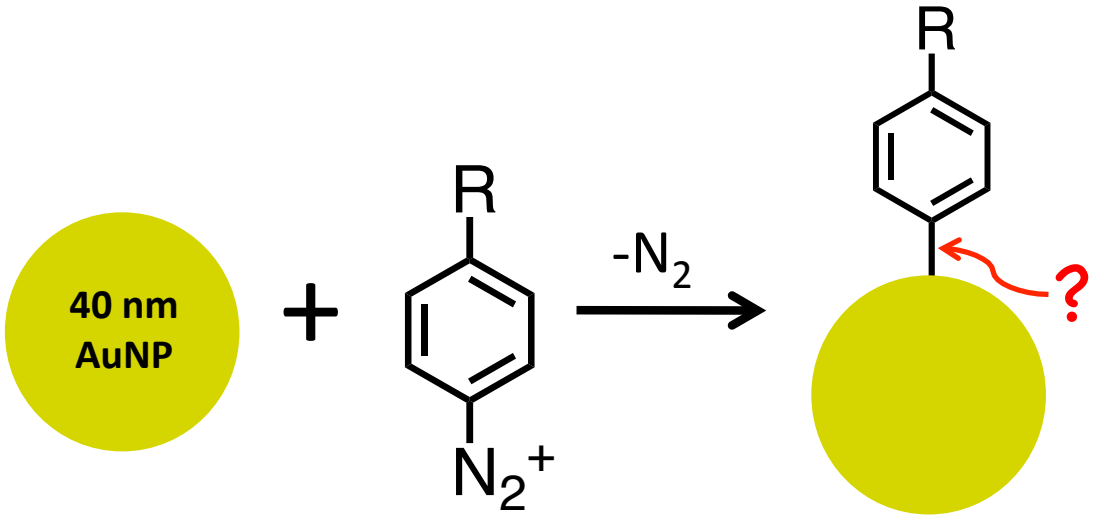

Figure 2.01. Potential reaction between a gold nanoparticle and diazonium cation.

The general understanding of the formation and structure of thiol derived self-assembled monolayers on planar gold substrates opened pathways for the use of thiols in the modification of gold nanoparticles (AuNPs).[21, 22] Following a similar train of thought, we envision the formation of aryl layers on AuNPs via the spontaneous reduction of diazonium salts. A general scheme of the potential reaction is shown in Figure 2.01. Our efforts are focused on showing that this

reaction takes place and in exploring the type of binding between the aryl groups and gold nanoparticles. The use of diazonium derived films for the stabilization of metal nanoparticles has been examined by Schiffrin and coworkers, who reported on the synthesis of gold and platinum nanoparticles in the presence of diazonium salts.[23] They postulated that the formation of a gold-carbon bond would provide superior stability compared to metal-sulfur interactions. A similar process was used for the synthesis of aryl-stabilized palladium nanoparticles.[24] In both of these studies, the existence of a metal-C covalent bond was assumed but not proven. The use of diazonium salts for the modification of pre-formed nanoparticles has also been demonstrated. Mangeney et al. reported on the sonication-assisted, electroless modification of diamond nanoparticles with 4-nitrobenzene diazonium salt.[25]

We demonstrate here the functionalization of pre-formed, citrate stabilized AuNPs by spontaneous adsorption of dNB as shown in Figure 2.01. We are motivated by the potential applications of nanoparticles with covalently bonded layers. In addition, this system affords the ability to probe the aryl group–gold interactions by surface enhanced Raman scattering (SERS). The combination of SERS and density functional theory (DFT) modeling is used to identify a Raman band associated with a Au-C stretch. This vibrational mode is also observed on planar gold surfaces by high-resolution energy electron loss spectroscopy (HREELS). The observation of a Au-C vibrational band is the first direct evidence of a covalent bond in diazonium derived aryl layers on noble metals.

2.2 EXPERIMENTAL

Reagents and Materials. 4-Nitrobenzenediazonium tetrafluoroborate, 97%, (dNB), silver nitrate, 99%, and tetrabutylammonium tetrafluoroborate ($TBABF_4$) were obtained from Sigma-Aldrich and used as received. Nitrobenzene 99% (NB) was purchased from Fisher Scientific. Reagent grade acetonitrile (CH_3CN) was purchased from either Caledon Laboratories or ACP Chemicals Inc. Anhydrous ethyl alcohol was obtained from Commercial Alcohols. 96% sulphuric acid and 30% hydrogen peroxide were obtained from Mallinckrodt. 40 nm citrate capped gold nanoparticles (AuNPs) were purchased from BBInternational with a concentration of $9x10^{10}$ particles/mL. Deionized water with a resistivity of 18 MΩ-cm or better was obtained with a Barnstead Nanopure purification system.

Gold nanoparticle modification. The 40 nm AuNPs were modified by mixing 10 μL of 2 mM 4-nitrobenzenediazonium tetrafluoroborate in acetonitrile with 1 mL of citrate capped gold nanoparticle solution. Control samples were prepared by adding 10 μL of 2 mM nitrobenzene in acetonitrile to 1 mL of AuNPs. The reagents were left to incubate for 24h after which time the nanoparticles were separated from solution *via* centrifugation at 8000 rpm for 10 min in an Eppendorf a5417R microcentrifuge. Next, the AuNP pellet was redispersed in 1 mL of deionized water. A second centrifugation step was added to wash the particles further. The suspended modified particles were stable and stored at 7ºC until use.

Extinction Spectroscopy. All nanoparticle solutions were diluted by a factor of 4 with deionized water before analysis. The extinction spectra were obtained in transmission mode on a double-beam Perkin Elmer Lambda 35 instrument with a photodiode detector. The UV-vis spectrum was scanned from 200 to 1100 nm with a scan rate of 960 nm/min. Deionized water or was used as the blank.

Raman Spectroscopy. The gold nanoparticles were analyzed by surface-enhanced Raman scattering (SERS). A 20 μL volume of the modified AuNPs was deposited on a gold coated 3x1 inch premium microscope slide (Fisher Scientific) and analyzed. SERS spectra were recorded with a Renishaw in Via Raman microscope. Radiation of 785 nm from a high-performance, air-cooled diode laser was used for excitation. The integration time for the Raman spectrum of solid dNB was 10 s with a 17 ± 0.5 mW laser power at the sample. The SERS spectra of dNB modified 40 nm AuNPs, 40 nm AuNPs reacted with NB and unmodified 40 nm AuNPs were integrated for 30 s and the laser power at the sample was 5 ± 0.5 mW. A Molectron Power Max 5100 meter was used to measure the laser power at the sample. All spectra were collected with a 50X objective. Care was taken to deposit equivalent amounts of particles on the slide and to focus the laser beam in areas of similar nanoparticle density for each sample.

High-resolution electron energy loss spectroscopy (HREELS). The electrochemical and spontaneous grafting of diazonium salts on planar gold and the subsequent HREELS analysis was performed by Rongbing Du and Greg

Lopinski at the Steacie Institute for Molecular Sciences. The results obtained support the nanoparticle modification work. A polished Au (111) single-crystal disk oriented to within 0.5^{o} of the (111) plane (Metal Crystals and Oxides) was cleaned in 3:1 v/v concentrated H_2SO_4/30% H_2O_2 at 120^{o}C for 30 min, followed by copious rinsing with Milli-Q water. (*The concentrated H_2SO_4:H_2O_2 piranha solution is very dangerous, particularly in contact with organic materials, and should be handled with extreme care).* Then the electrode was continuously cycled in aqueous 0.5 M H_2SO_4 solution between 0 and 1.75 V (SHE) at 100 mV/s until repeatable cyclic voltammograms were obtained. Cycling was halted and then maintained at 0 V for 60 s in order to obtain an oxide-free surface. Electrochemical grafting employed an Autolab PGSTAT potentiostat (Eco Chemie, Utrecht, Netherlands), a homemade reference electrode consisting of a silver wire submerged in a 0.01 M $AgNO_3$ solution in acetonitrile with 0.1 M tetrabutylammonium tetrafluoroborate ($TBABF_4$), and a platinum wire as the counter electrode. Electrochemical grafting was carried out using three full sweeps from 400 mV to -600 mV at a sweep rate of 200 mV/s and a diazonium salt (4-nitrobenzenediazonium tetrafluoroborate) concentration of 2.5 mM in acetonitrile with 0.1 M $TBABF_4$. Diazonium salt solutions were deaerated for 10 min with Ar gas prior to depositions. Spontaneous grafting was carried out by immersing cleaned Au substrates in a 1 mM solution of the diazonium salt in acetonitrile in the dark for at least 24 h. After the molecular grafting, the modified Au samples were rinsed and sonicated for 30 min in acetonitrile to remove the residual diazonium salt and the physisorbed materials.

The modified Au sample was attached to a molybdenum plate sample holder with a tungsten filament behind the sample to enable radiative heating. Upon transfer to the ultrahigh vacuum system (UHV), samples were heated to less than 400^{o}C to remove physisorbed species. HREELS was carried out with an LK Technologies LK3000 spectrometer. Spectra were acquired in the specular geometry (60^{o} with respect to the surface normal) at an incident beam-energy of 6 eV and a nominal spectrometer resolution of 6 meV (56 cm^{-1}).

Computational techniques. The computational calculations presented in this work were performed by Stanislav Stoyanov, Sergey Gusarov and Andriy Kovalenko from the Theory and Modeling group at the National Institute for Nanotechnology (NINT). The geometry optimization of $Au_{20}NB$ and $Au_{20}NB_3$ in C_S symmetry was performed using the Becke-Perdew (BP86) exchange-correlation functional,[26, 27] as implemented in the Gaussian 09 computational chemistry package.[28] The BP86 functional often yields harmonic frequencies that are close to the experimental values.[29, 30] For comparison, the PBE1PBE functional is also employed.[31] The $Au_{20}NB$ and $Au_{20}NB_3$ contain odd number of electrons and the electronic structures are modeled as unrestricted using double determinants. The Stuttgart-Dresden (SDD) effective core potential (ECP) was used for relativistic treatment of the [1s^2-4f^{14}] core electrons of Au.[32] The (8s7p6d)/[6s5p3d] Gaussian-type orbital (GTO) was applied for the valence shell of Au. The all-electron double-ζ basis set 6-31G* is used for O, N, C and H atoms.[33, 34] The Raman polarizability derivatives were calculated by numerically differentiating the analytic dipole derivatives with respect to an electric field.

2.3 RESULTS AND DISCUSSION

Previous reports have shown that aryl films can be formed on planar gold surfaces from the spontaneous reduction of diazonium ions.[20, 35] It has also been shown that metal nanoparticles can be stabilized during synthesis by a diazonium derived layer.[23, 24] It has not yet been demonstrated that diazonium salts will spontaneously adsorb to preformed gold nanoparticles (AuNPs). We describe here our results from spectroscopic studies that show aryl layers form on the surface of 40 nm AuNPs from the spontaneous adsorption of the corresponding diazonium salt. Vibrational spectroscopic data is used to probe the interaction between the aryl groups and AuNPs.

2.3.1 UV-vis analysis.

A strong absorption band, known as the localized surface plasmon resonance (LSPR), is observed in the visible spectrum of AuNPs. It is known that the position of this band is sensitive to the dielectric constant surrounding the nanoparticle and, thus, responds to surface modification. For example, the self-assembly of an alkanethiolate monolayer on silver nanoparticles was shown to red shift the wavelength maximum (λ_{max}) of the LSPR.[36] The visible spectrum can also be used to monitor the stability and flocculation of nanoparticles in solutions.[36, 37] Commercial 40 nm AuNPs were reacted with nitrobenzene diazonium cations (dNB) as well as nitrobenzene, for comparison. Figure 2.02 contains the extinction spectra centred around the LSPR bands for unmodified,

citrate capped 40 nm AuNPs and nanoparticles exposed to the various potential adsorbates. The λ_{max} values of the LSPR bands are also listed in Figure 2.02.

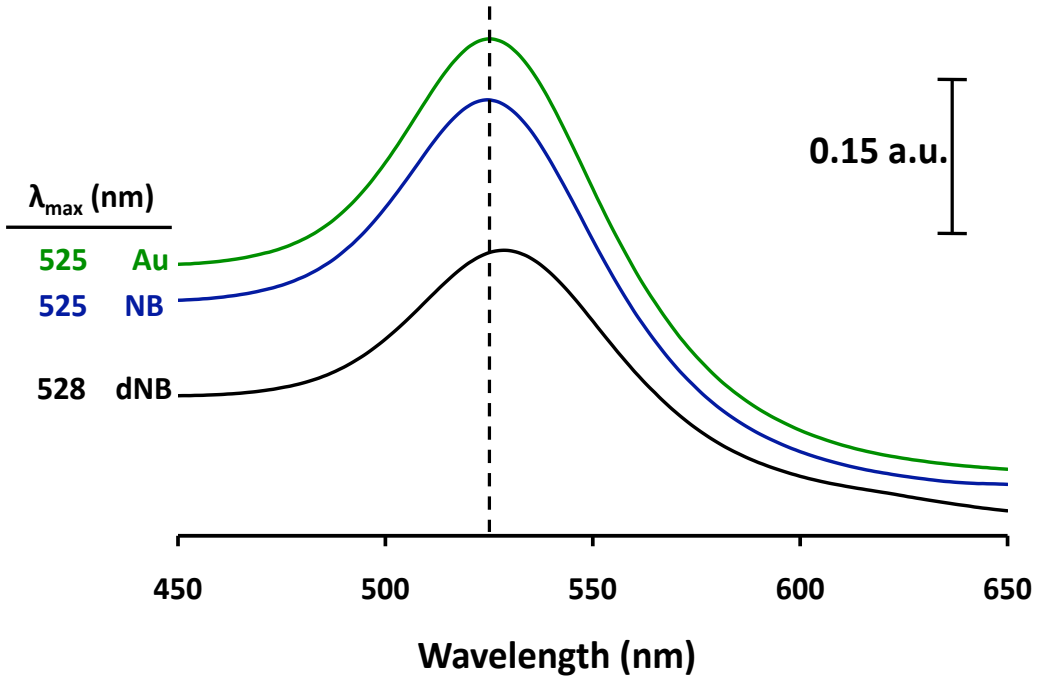

Figure 2.02. Extinction spectra of unmodified 40 nm AuNPs, AuNPs reacted with nitrobenzene (NB, control), and dNB modified 40nm AuNPs. All samples were suspended in water. The mean value of λ_{max} for 3 measurements is shown. The uncertainty of the measurement (s.d.) is 0.3 nm.

The band for the unmodified NPs exhibits a maximum at 525 nm. Nanoparticles reacted with NB yield a λ_{max} that is indistinguishable from unmodified AuNPs, implying there is negligible physisorption through the

aromatic ring or the nitro group. The band position for NPs reacted with dNB is located at 528 nm, red shifted significantly from that for unmodified NPs. This shift in λ_{max} is consistent with the formation of an adsorbate layer on the surface of the nanoparticles. We note that the intensity of the LSPR band for the dNB modified AuNPs is lower than that for the unmodified AuNPs. This is due to loss of a portion of the AuNPs during separation of the modified nanoparticles from unreacted diazonium salt via centrifugation. However, the dNB modified AuNPs that are resuspended remain stable in the aqueous solution. The spectrum in Figure 2.02 provides no indicators of nanoparticle aggregation, as we observe no absorption bands in the region between 600 and 800 nm. We have found that 40 nm AuNPs modified with dNB are stable in solution for at least one month with no evidence of aggregation. We conclude from Figure 2.02 that reaction of dNB with AuNPs results in the formation of an adsorbed layer on the nanoparticle surface.

2.3.2 Vibrational spectroscopy comparison.

We have further characterized the diazonium-derived layers on AuNPs with surface enhanced Raman scattering (SERS). Gold nanoparticles with diameters in the 20 to 100 nm range are excellent substrates for SERS.[38] In addition, NB and NB-containing films have been the subject of a number of normal Raman[39] and SERS investigations.[22, 40] In addition to providing structural information of an adsorbed layer, vibrational spectroscopy is particularly useful for probing the nature of the bonding between various adsorbates and gold substrates; a number of studies have reported evidence of a Au-C covalent bond.

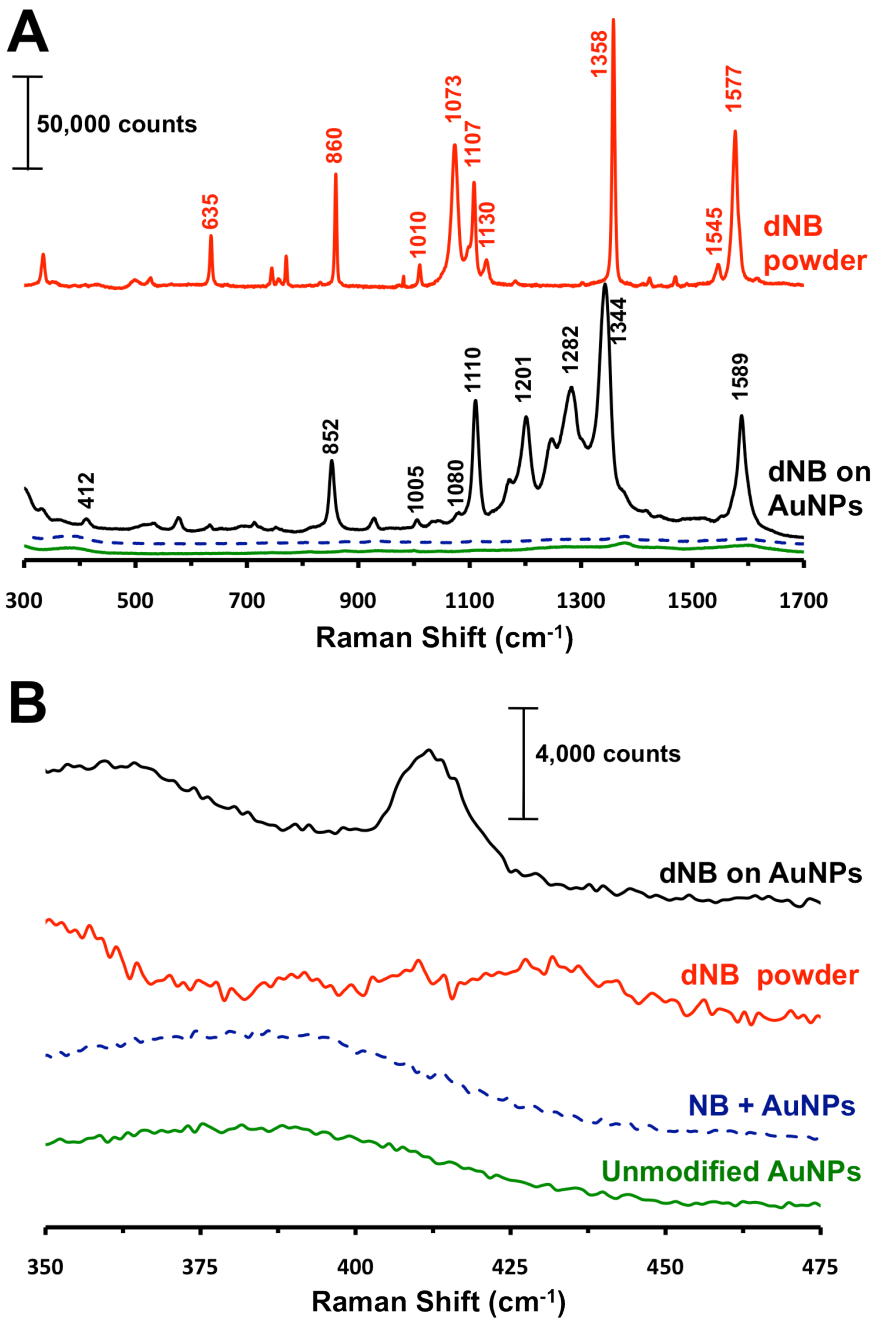

Figure 2.03. (A). Raman spectrum of solid dNB (top spectrum, red) and SERS spectra of dNB modified 40 nm AuNPs (solid black line), 40 nm AuNPs reacted with NB (dashed blue line) and unmodified 40 nm AuNPs (solid green line). (B). Raman and SERS spectra of all the samples in (A) expanded near 400 cm^{-1}.

Table 2.1. Band assignments listed for the Raman spectrum of solid dNB and the SERS spectrum of NB on the surface of 40 nm AuNPs. References 39 and 40 were used for some assignments.

	Band position (cm^{-1})	
Assignment	**dNB Powder**	**dNB on AuNPs**
N≡N stretch	2309	–
Ring stretch	1577	1589
Asymmetric NO_2 str.	1545	–
Symmetric NO_2 stretch	1358	1344
C-N_2 stretch	1130	–
C-N str. + ring str.	1107	1110
CH i.p. bend	1073	1080(w)
Ring breathing	1010	1005(w)
ONO scissor + ring str.	860	852
Asym. Ar C-C str. + C-N-N i.p. deform.	635	–

Recently, infrared photodepletion spectroscopy was used to study Au cluster with chemisorbed CO. The vibrational spectra obtained show Au-CO stretching and Au-C-O bending bands between 250-400 cm^{-1}.[41] Cyanide adsorption to gold has been probed with SERS. One study observed a band at 375 cm^{-1} which was tentatively assigned to $Au(CN)_2^-$.[42] Other investigations have reported an Au-C stretching mode for Au-CN at 370 cm^{-1}.[43-45]

Figure 2.03A contains the Raman spectra in the region between 300 and 1700 cm^{-1} for the various NB-AuNP combinations as well as the normal Raman spectrum of dNB powder. The spectra for the two control samples (unmodified and NB) exhibit no major bands, consistent with negligible physical adsorption of NB to Au nanoparticles. The spectrum of the dNB modified AuNPs is significantly enhanced and features numerous bands that are consistent with those observed in the dNB powder spectrum. Band assignments are listed in Table 2.1. The relative intensities of some of the more prominent bands as well as band positions in the SERS spectrum agree well with the dNB powder spectrum. Despite these similarities, there are notable differences between the two spectra. First, bands in the powder spectrum associated with the diazonium moiety are not observed in the SERS spectrum. A strong band is observed in the powder spectrum at 2309 cm^{-1} (not shown), which corresponds to the N-N stretch of the diazonium group. This band is not observed in the SERS spectrum of dNB on AuNPs. In addition, bands at 1130 and 635 cm^{-1} in the dNB powder spectrum also involve the diazonium moiety (Table 2.1) and are not observed in the SERS spectrum. Taken together, these observations are strong evidence for spontaneous reduction of the diazonium cation to the aryl radical and the formation of a NB layer at the AuNP surface.

A second major difference in the spectra in Figure 2.03A is evident in the region between 1200 and 1300 cm^{-1}. The SERS spectrum of dNB on AuNPs exhibits bands at 1201, 1250 and 1282 cm^{-1} that are not present in the dNB powder spectrum. We believe these bands are due to the multilayer nature of the

dNB film on the AuNPs and assignment of these bands will be discussed below. Finally, a low intensity band at 412 cm^{-1} is observed in the dNB spectrum. This band is highlighted in the expanded region of the spectra in Figure 2.03B. A band centered at 412 cm^{-1} is clearly present in the dNB spectrum and not in the spectra of the powder or either of the control spectra. We have also observed this band in SERS spectra of other diazonium salts spontaneously adsorbed to AuNPs. Reaction of 40 nm AuNPs with nitroazobenzene diazonium salt results in a band at 416 cm^{-1}, while reaction with phenylacetic acid diazonium salt produces a band at 410 cm^{-1}. As noted above, previous work has assigned bands at 375 cm^{-1} to a Au-C stretch for Au-CN. We thus tentatively assign the band at 412 cm^{-1} observed in Figure 2.03B to a Au-C stretch. The modeling studies described below support this assignment.

2.3.3 Computational study of modified gold nanoparticles.

It is well accepted that electrochemically deposited diazonium derived layers are bound to carbon materials through a C-C covalent bond.[7] Although it has been shown that these types of aryl films are strongly bonded to gold and other metals[13, 19] and a Au-C bond has been predicted computationally,[46, 47] direct spectroscopic evidence of a Au—C covalent bond has not yet been reported. The attachment and configuration of phenyl groups to gold have been previously explored using density functional theory (DFT). It has been predicted using DFT that the bond between the phenyl group and the gold surface is chemical in nature and that the upright configuration of the phenyl ring is favored.[46] Other modeling

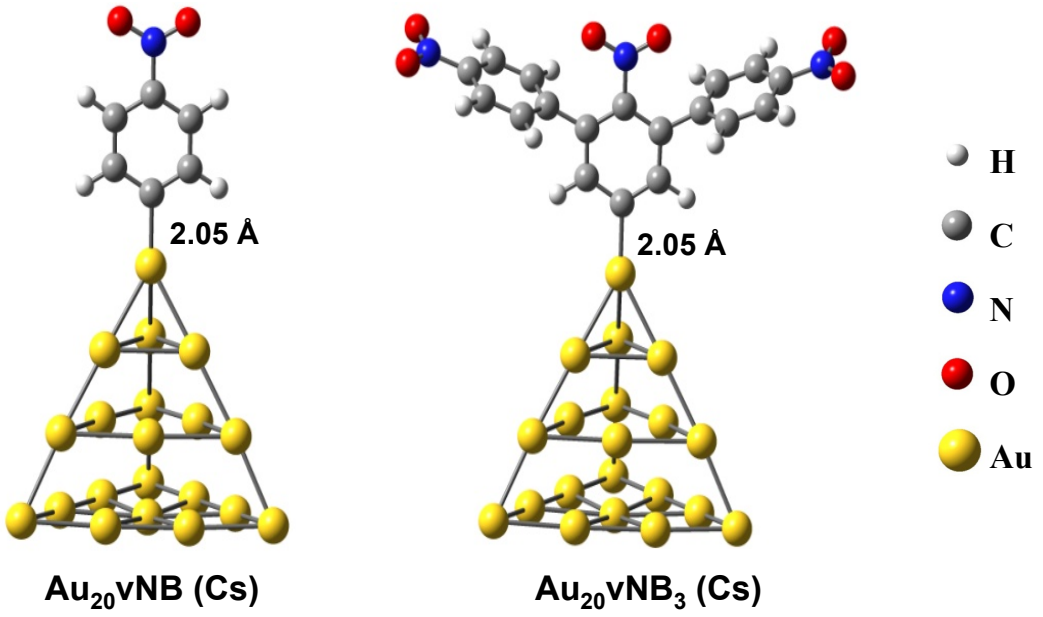

Figure 2.04. Optimized structure of a nitrobenzene monomer (Au_{20}vNB) and trimer ($Au_{20}vNB_3$) covalently bonded to pyramidal Au_{20} clusters.

efforts have used and optimized DFT calculations to complement SERS experimental results.[48] Schatz and coworkers have developed a time-dependent DFT method for calculating SERS enhancement factors and predicting band positions. The model is based on a pyridine molecule adsorbed to a 20 atom silver cluster.[29, 49] Building upon these previous reports, we model dNB adsorbed to gold nanoparticles as an NB molecule covalently bonded to the vertex of an Au_{20} pyramidal cluster and label it Au_{20}vNB (Figure 2.04). The effect of NB multilayer formation on Raman spectra is modeled by an NB trimer bonded to the vertex of an Au_{20} cluster, labeled as $Au_{20}vNB_3$. In Figure 2.04, we show the optimized

geometries of the structures containing NB and NB_3 bonded to the vertices of Au_{20} pyramids. Binding configurations containing NB and NB_3 covalently bonded to the vertex of the Au_{20} pyramid are more stable by 44 and 39 kJ/mol, respectively, than the configurations bonded to the face of the pyramid. Optimization of structures containing NB bonded to the rim of the Au_{20} pyramid converges to either a vertex or a surface bonded structure. The optimized Au-C bond lengths are 2.05 Å for both Au_{20}vNB and Au_{20}vNB_3.

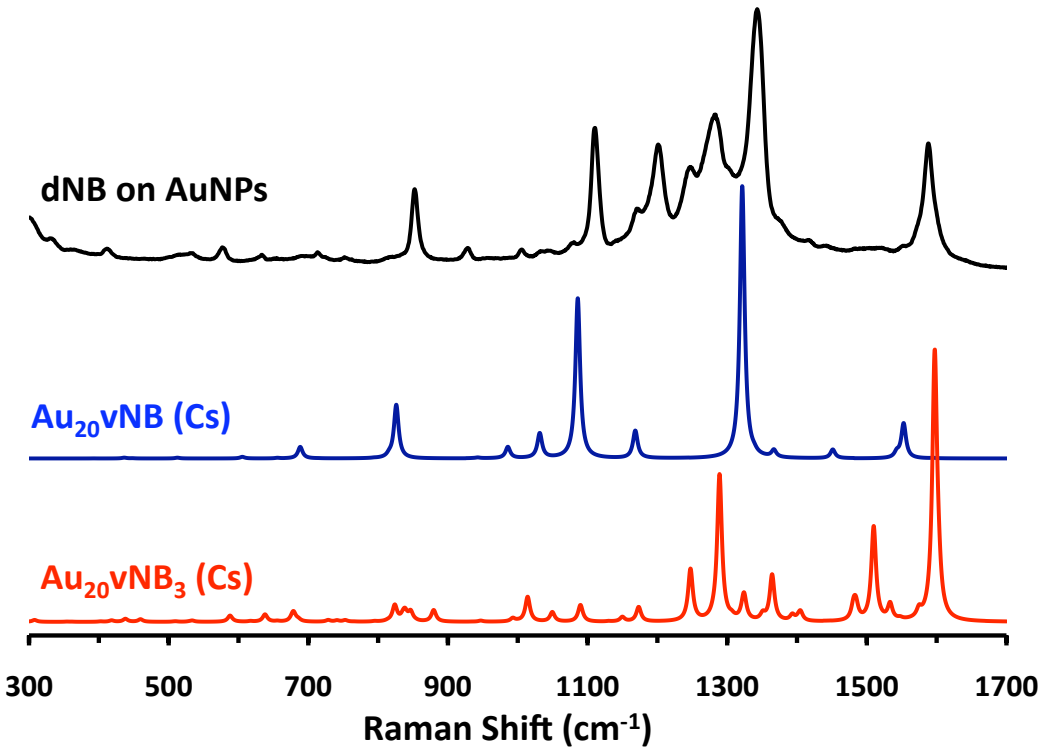

Figure 2.05. Calculated Raman spectra (Gaussian 09) of Au_{20}vNB and Au_{20}vNB_3 compared to the SERS spectrum of dNB bonded to AuNPs.

Table 2.2. Assignment of Raman bands from the SERS spectrum and from calculated (Gaussian 09) spectra of the Au_{20}vNB and Au_{20}vNB_3 structures.

	Band position (cm^{-1})		
Assignment	**SERS of dNB on AuNPs**	**Au_{20}vNB**	**Au_{20}vNB_3**
Ring stretch	1589	1553	1598, 1510
Symmetric NO_2 stretch	1344	1322	1365, 1325
Ring breathing	1282, 1250	1277 (weak)	1289, 1248
C-H i.p. bend	1201, 1170	1169	1174, 1152
C-N str. + ring str.	1110	1086	1091
ONO scissor + ring str.	852	836	825
Au-NB stretch	412	439	414

The calculated Raman spectra for the model systems as well as the experimental SERS spectrum of dNB on AuNPs are shown in Figure 2.05. The electronic absorption maximum for nitrobenzene is 263 nm and we do not expect any resonance Raman effects with the 785 nm excitation used here. Thus, the Raman scattering intensities for the model systems were calculated for the static case. Band assignments for the two models as well as the experimental SERS

spectrum are listed in Table 2.2. Qualitatively, in terms of relative band intensities and band positions, the spectrum derived from the Au_{20}vNB model agrees more closely to the experimental SERS spectrum. This implies that the majority of the nitrobenzene molecules bound to the 40 nm AuNPs are in a single layer. The spectrum yielded by the $Au_{20}vNB_3$ model contains a number of additional modes assignable to the NB groups in the second layer. Of particular interest are ring breathing modes for the second layer of NB groups at 1289 and 1248 cm^{-1}. These modes agree well with bands observed at 1282 and 1250 cm^{-1} in the SERS spectrum. Multiple bands for in-plane C-H bending modes in the spectrum of $Au_{20}vNB_3$ are also consistent with the SERS spectrum. A number of other bands predicted for $Au_{20}vNB_3$ are not observed in the SERS spectrum. These differences may be due to dissimilarities in the structure of the branched units in the dNB layer on the AuNPs and the model trimer structure. The model also does not account for coverage effects, which will certainly influence the bands observed in the SERS spectrum. Despite this, the agreement of the SERS spectrum with the calculated spectra of the two model structures is consistent with a diazonium derived NB film bound to the AuNPs that contains branched multilayer structures.

A number of reports have addressed the interaction between diazonium derived films and metals based on the stability of the film to various treatments.[13, 15, 18, 19] Shewchuk and others have previously shown that electrochemically deposited dNB remains bound to planar gold surfaces following severe ultrasonic treatment[15, 19] and exposure to boiling solvents.[19] In addition, the dNB layer cannot

be entirely displaced by long chain alkane thiols that completely displace a mercaptonitrobenzene monolayer. Recently, it was shown that a portion of a spontaneously adsorbed dNB film on planar gold remains following ultrasonic treatment in acetonitrile.[20] It has been suggested that these observations were due to a covalent linkage between the diazonium derived film and the gold surface. However, direct evidence of a Au-C covalent bond has not yet been reported. The

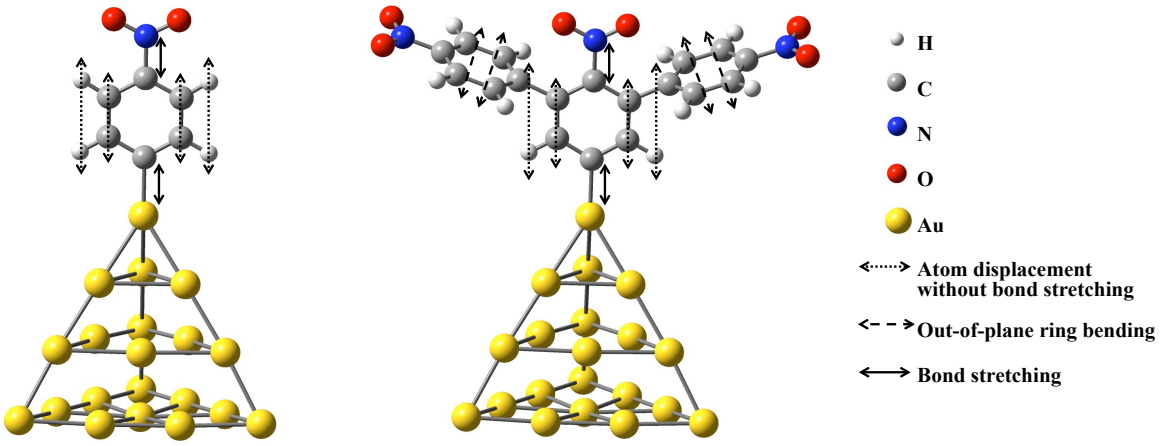

Figure 2.06. Illustration of the calculated (Gaussian 09) vibrational modes at 439 cm^{-1} ($Au_{20}vNB$) and 414 cm^{-1} ($Au_{20}vNB_3$) that involve Au-C bond stretching coupled with out-of-plane aromatic ring bending modes.

calculated Raman spectra from the two model systems both contain bands due to modes involving a Au-C stretch. As listed in Table 2.2, this band appears at 439 cm^{-1} for Au_{20}vNB and 414 cm^{-1} for Au_{20}vNB_3. The modes responsible for these bands are shown in Figure 2.06. As noted above, we observe a band at 412 cm^{-1} in the SERS spectrum of dNB on AuNPs that is neither observed in the Raman spectrum of the dNB starting material nor in the controls (SERS spectra of unmodified AuNPs and AuNPs with physisorbed NB). There are also no other bands in that vicinity of the SERS spectrum. We thus assign the 412 cm^{-1} band to a mode involving a Au-C stretch as predicted in the Raman spectra of our models. This provides direct evidence for the existence of a Au-C covalent bond for this system.

2.3.4 HREELS supporting evidence on planar gold.

The observation of a Au-C stretch in SERS spectra is compelling evidence for the existence of a gold-carbon covalent bond in diazonium derived films on nanoparticles. Confirmation that this mode of bonding occurs on planar surfaces requires a highly surface sensitive vibrational spectroscopic method. We thus studied dNB films on single crystal Au(111) surfaces with high-resolution electron energy loss spectroscopy (HREELS). In HREELS vibrational modes of adsorbed molecules can be identified by analyzing the energy loss of inelastically scattered electrons. Dipole active modes tend to dominate HREELS spectra in the specular scattering geometry, however, non-dipole active modes can be observed as well. Thus, HREELS spectra are very comparable and complementary to SERS spectra.

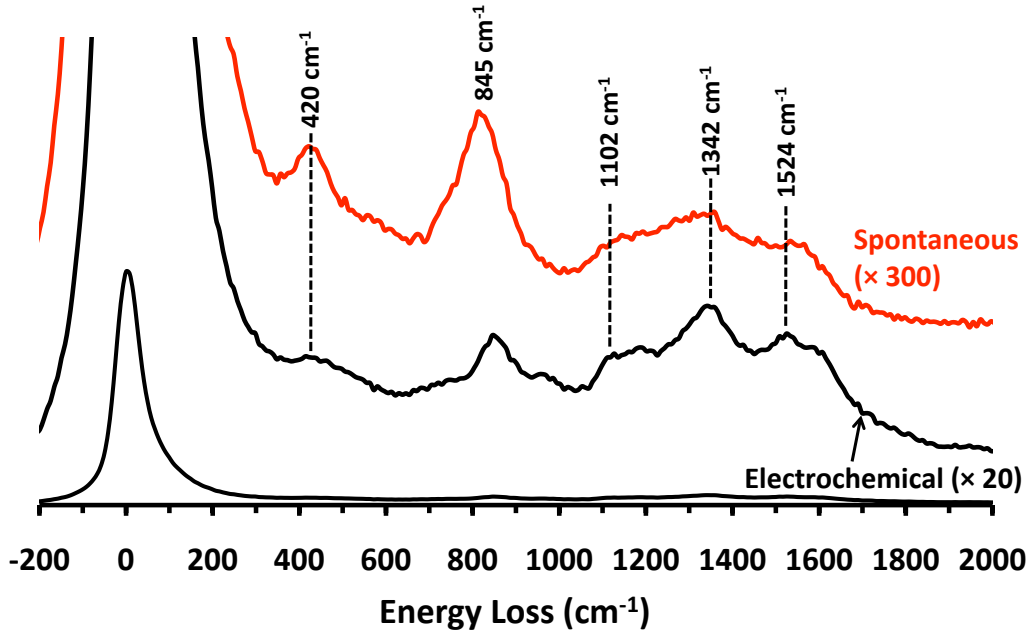

Figure 2.07. HREELS spectra for dNB films on Au(111) by spontaneous adsorption (upper, red curve) and electrochemical grafting (middle and lower, black curve). The lower spectrum is for the electrochemically deposited film plotted at full scale. The other spectra are plotted with expanded y-axis to better observe the vibration bands.

Figure 2.07 contains HREELS spectra for Au(111) modified with dNB by both electrochemical grafting and spontaneous adsorption. The bottom spectrum in Figure 2.07 is that for the electrochemically deposited film plotted at full-scale and showing the relative intensities between the elastically scattered and

inelastically scattered electrons. The signal intensities for the other two spectra in Figure 2.07 were normalized to the elastic bands and were expanded for clarity. The electrochemically deposited film yields bands at 1524, 1342, 1102, 845, and 420 cm^{-1} in the region shown. The band at 845 cm^{-1} is assigned to the ring stretch + ONO scissor mode and is in good agreement with the SERS peak observed at 852 cm^{-1}. The 1102 cm^{-1} band is assigned to a mode involving a ring stretch and a C-N stretch (Table 2.1). The bands at 1342 and 1524 cm^{-1} are assigned to symmetric and asymmetric NO_2 stretching based on previous publications.[19, 50] The peak observed at 420 cm^{-1} is assigned to the Au-C stretch due to its proximity to the 412 cm^{-1} band in the SERS spectra.

The bands due to inelastic scattering for the spontaneously adsorbed dNB are much less intense than those for the electrochemically deposited film. Based on our group's previous work, we expect that the conditions used here for electrochemical deposition results in a dense, multilayer film of dNB with a thickness of ~2 nm. Since, in general the inelastic scattering intensity increases with surface coverage, the lower loss peak intensities observed for spontaneous adsorbed film indicates that the coverage of dNB groups is substantially lower than that observed for the electrochemically deposited film. Despite the difference in coverage, the HREELS spectrum for the spontaneously adsorbed dNB film contains bands with similar position as the electrochemically deposited film. An interesting observation is the higher relative intensity of the band at 420 cm^{-1} in the spectrum of the spontaneously adsorbed film. We believe the enhanced intensity of this mode results from a relatively thin spontaneously adsorbed film

compared to the electrochemically deposited film. A less intense band for a mode located at the metal-film interface is expected for a thicker, multilayer film due to the limited probing depth of the electrons. This observation also provides support for our assignment of the 420 cm^{-1} band to a Au-C stretching vibration. We thus conclude that a Au-C covalent bond is formed upon either spontaneous adsorption or electrochemical grafting of dNB to Au (111).

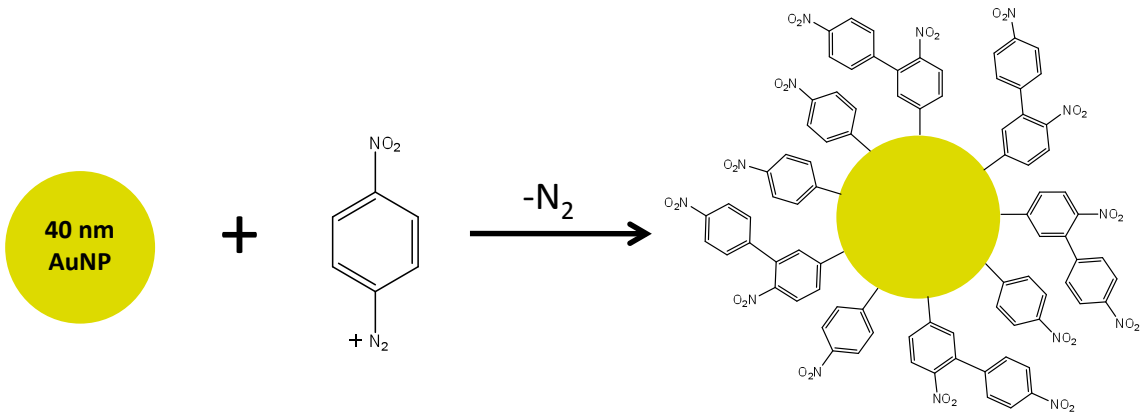

Figure 2.08. Reaction scheme for the spontaneous adsorption of dNB to 40 nm AuNPs illustrating the proposed film structure on the surface of the nanoparticle.

2.4 CONCLUSION

The results presented here show that aryl films can be formed on gold nanoparticles by spontaneous reaction with diazonium precursors. Nanoparticles modified with diazonium derived nitrobenzene yield excellent quality SERS spectra. Both UV-visible extinction spectroscopy and SERS are consistent with the formation of a nitrobenzene layer. The nitrobenzene modified nanoparticles are stable in solution for at least 1 month. Comparison of the SERS spectrum with Raman spectra from DFT modeling indicates a degree of multilayer formation on the nanoparticles. The results are consistent with a reaction such as that shown in Figure 2.08. Although Figure 2.08 implies propagation of the multilayer solely through aryl-aryl attachment, propagation via radical attack of the nitro group is also a possibility. Importantly, the DFT modeling leads to the assignment of a SERS observed band at 412 cm^{-1} to a Au-C stretching mode. This is the first direct evidence of a gold-carbon covalent bond in these systems. Results from HREELS experiments confirm the existence of a Au-C bond for diazonium derived films on planar surfaces. The anchoring of these types of films through a covalent interaction explains their enhanced stability compared to thiol derived monolayer analogs. Diazonium derived films on gold and other metals will continue to find applications where high stability and/or strong adsorbate-substrate coupling are required.

2.5 REFERENCES

1. Buriak, J. M. *Chem. Rev.* **2002,** 102, (5), 1271-1308.
2. Ulman, A. *Chem. Rev.* **1996,** 96, 1533-1554.
3. Downard, A. J. *Electroanalysis* **2000,** 12, (14), 1085-1096.
4. Palacin, S.; Bureau, C.; Charlier, J.; Deniau, G.; Mouanda, B.; Viel, P. *ChemPhysChem* **2004,** 5, (1468-1481).
5. Love, J. C.; Estroff, L. A.; Kriebel, J. K.; Nuzzo, R. G.; Whitesides, G. M. *Chem. Rev.* **2005,** 105, 1103-1169.
6. Vericat, C.; Vela, M. E.; Benitez, G.; Carro, P.; Salvarezza, R. C. *Chem. Soc. Rev.* **2010,** 39, 1805-1834.
7. Pinson, J.; Podvorica, F. *Chem. Soc. Rev.* **2005,** 34, (5), 429-439.
8. Kariuki, J. K.; McDermott, M. T. *Langmuir* **1999,** 15, (19), 6534-6540.
9. Kariuki, J. K.; McDermott, M. T. *Langmuir* **2001,** 17, (19), 5947-5951.
10. Liu, Y.-C.; McCreery, R. L. *Anal. Chem.* **1997,** 69, 2091-2097.
11. Combellas, C.; Kanoufi, F.; Pinson, J.; Podvorica, F. I. *Langmuir* **2005,** 21, (1), 280-286.
12. Boukerma, K.; Chehimi, M. M.; Pinson, J.; Blomfield, C. *Langmuir* **2003,** 19, (15), 6333-6335.
13. Hurley, B. L.; McCreery, R. L. *J. Electrochem. Soc.* **2004,** 151, (5), B252-B259.
14. Bernard, M. C.; Chausse, A.; Cabet-Deliry, E.; Chehimi, M. M.; Pinson, J.; Podvorica, F.; Vautrin-Ul, C. *Chem. Mater.* **2003,** 15, (18), 3450-3462.

15. Laforgue, A.; Addou, T.; Belanger, D. *Langmuir* **2005,** 21, (15), 6855-6865.

16. Ricci, A.; Bonazzola, C.; Calvo, E. J. *Phys. Chem. Chem. Phys.* **2006,** 8, (37), 4297-4299.

17. Liu, G. Z.; Bocking, T.; Gooding, J. J. *J. Electroanal. Chem.* **2007,** 600, (2), 335-344.

18. Paulik, M. G.; Brooksby, P. A.; Abell, A. D.; Downard, A. J. *J. Phys. Chem. C* **2007,** 111, (21), 7808-7815.

19. Shewchuk, D. M.; McDermott, M. T. *Langmuir* **2009,** 25, (8), 4556-4563.

20. Lehr, J.; Williamson, B. E.; Flavel, B. S.; Downard, A. J. *Langmuir* **2009,** 25, (23), 13503-13509.

21. Brust, M.; Fink, J.; Bethell, D.; Schiffrin, D. J.; Kiely, C. *J. Chem. Soc., Chem. Commun.* **1995**, (16), 1655-1656.

22. Ni, J.; Lipert, R. J.; Dawson, G. B.; Porter, M. D. *Anal. Chem.* **1999,** 71, (21), 4903-4908.

23. Mirkhalaf, F.; Paprotny, J.; Schiffrin, D. J. *J. Am. Chem. Soc.* **2006,** 128, (23), 7400-7401.

24. Ghosh, D.; Chen, S. W. *J. Mater. Chem.* **2008,** 18, (7), 755-762.

25. Mangeney, C.; Qin, Z.; Dahoumane, S. A.; Adenier, A.; Herbst, F.; Boudou, J. P.; Pinson, J.; Chehimi, M. M. *Diamond Relat. Mater.* **2008,** 17, (11), 1881-1887.

26. Becke, A. D. *Phys. Rev. A* **1988,** 38, (6), 3098-3100.

27. Perdew, J. P. *Phys. Rev. B* **1986,** 33, (12), 8822-8824.

28. Frisch, M. J.; Trucks, G. W.; Schlegel, H. B.; Scuseria, G. E.; Robb, M. A.; Cheeseman, J. R.; Scalmani, G.; Barone, V.; Mennucci, B.; Petersson, G. A., et al. *Gaussian 09*, Gaussian, Inc.: Wallingford CT, 2009.

29. Aikens, C. M.; Schatz, G. C. *J. Phys. Chem. A* **2006,** 110, (49), 13317-13324.

30. Neugebauer, J.; Hess, B. A. *J. Chem. Phys.* **2003,** 118, (16), 7215-7225.

31. Perdew, J. P.; Burke, K.; Ernzerhof, M. *Phys. Rev. Lett.* **1996,** 77, (18), 3865-3868.

32. Andrae, D.; Haussermann, U.; Dolg, M.; Stoll, H.; Preuss, H. *Theor. Chim. Acta* **1990,** 77, (2), 123-141.

33. Mclean, A. D.; Chandler, G. S. *J. Chem. Phys.* **1980,** 72, (10), 5639-5648.

34. Krishnan, R.; Binkley, J. S.; Seeger, R.; Pople, J. A. *J. Chem. Phys.* **1980,** 72, (1), 650-654.

35. Adenier, A.; Cabet-Deliry, E.; Chausse, A.; Griveau, S.; Mercier, F.; Pinson, J.; Vautrin-Ul, C. *Chem. Mater.* **2005,** 17, (3), 491-501.

36. Malinsky, M. D.; Kelly, K. L.; Schatz, G. C.; Van Duyne, R. P. *J. Am. Chem. Soc.* **2001,** 123, (7), 1471-1482.

37. Weisbecker, C. S.; Merritt, M. V.; Whitesides, G. M. *Langmuir* **1996,** 12, (16), 3763-3772.

38. Porter, M. D.; Lipert, R. J.; Siperko, L. M.; Wang, G.; Narayanan, R. *Chem. Soc. Rev.* **2008,** 37, 1001-1011.

39. Clarkson, J.; Smith, W. E. *J. Mol. Struct.* **2003,** 655, 413-422.

40. Skadtchenko, B. O.; Aroca, R. *Spectrochim. Acta, Part A* **2001,** 57, 1009-1016.

41. Fielicke, A.; von Helden, G.; Meijer, G.; Pedersen, D. B.; Simard, B.; Rayner, D. M. *J. Am. Chem. Soc.* **2005,** 127, (23), 8416-8423.

42. Baltruschat, H.; Heitbaum, J. *J. Electroanal. Chem.* **1983,** 157, (2), 319-326.

43. Beltramo, G. L.; Shubina, T. E.; Mitchell, S. J.; Koper, M. T. M. *J. Electroanal. Chem.* **2004,** 563, (1), 111-120.

44. Watling, K.; Hope, G. A.; Woods, R. *J. Electrochem. Soc.* **2005,** 152, (6), D103-D108.

45. Bozzini, B.; D'Urzo, L.; Mele, C.; Romanello, V. *J. Phys. Chem. C* **2008,** 112, (16), 6352-6358.

46. Jiang, D. E.; Sumpter, B. G.; Dai, S. *J. Am. Chem. Soc.* **2006,** 128, (18), 6030-6031.

47. de la Llave, E.; Ricci, A.; Calvo, E. J.; Scherlis, D. A. *J. Phys. Chem. C* **2008,** 112, (45), 17611-17617.

48. Zhao, J.; Dieringer, J. A.; Zhang, X. Y.; Schatz, G. C.; Van Duyne, R. P. *J. Phys. Chem. C* **2008,** 112, (49), 19302-19310.

49. Zhao, L. L.; Jensen, L.; Schatz, G. C. *J. Am. Chem. Soc.* **2006,** 128, (9), 2911-2919.

50. Whelan, C. M.; Barnes, C. J.; Walker, C. G. H.; Brown, N. M. D. *Surf. Sci.* **1999,** 425, (2-3), 195-211.

Chapter 3:

Evidence for Controllable Multilayer Formation of Spontaneously Grafted Diazonium Salt Derived Layers on Gold Nanoparticles

3.1 INTRODUCTION

In Chapter 2 the modification of gold nanoparticles with diazonium salt precursors was introduced and it was shown that these layers are covalently linked to the gold surface through an Au-C covalent bond. This chapter will serve as an extension to that work and characterize the adlayers in more detail providing a better understanding of the nature of the resulting film. The motivation behind this study is the ongoing importance of gold nanoparticles (AuNPs) in a variety of applications such as bioassays,[1-4] medical imaging,[5, 6] and electrocatalysis.[7] In almost every application the integration of nanoparticles (NPs) requires a carefully designed surface chemistry. To this end we have continued the work on spontaneous grafting of diazonium ions on AuNPs utilizing the covalent nature of the adlayer.

The gold nanoparticle modification scheme presented here is derived from the better understood surface modification of planar substrates that include silicon,[8] carbon,[9] and gold.[10] For planar substrates the diazonium derived adlayer attachment proceeds *via* a radical intermediate that is either generated by application of an external potential or by spontaneous reduction of the diazonium

ions in the presence of a conductive material. Aryl radicals either bind to the substrate directly or attach to already adsorbed molecules forming multilayers. Kariuki was the first to show multilayer formation on highly oriented pyrolytic graphite (1999) and on glassy carbon (2001) by probing defect sites and employing masks to cover areas on the substrate allowing for height differentiation by atomic force microscopy (AFM).[11, 12] These results were later confirmed by Anariba *et al.* on pyrolyzed photoresist films (2003) using AFM to scratch an area of the diazonium derived film and then to measure the height difference between the scratched area and the intact film.[13] This "scratch test" has now become a common method to measure film thickness.[14] Closely related to the work presented in this chapter, Downard and coworkers have shown evidence of multilayer formation for the spontaneous reduction of nitrobenzene diazonium ions on planar gold substrates (2009).[15] It has also been shown that diazonium derived films can grow to a substantial thickness that is limited by the availability of radicals in solution. Film thicknesses on the order of 1-2 μm can be achieved by prolonged chronoamperometric treatment.[11, 16, 17]

The knowledge from the behavior of diazonium derived films on planar substrates can be used to explain discrepancies observed in Chapter 2 between experimentally derived SERS spectra and calculated Raman spectra of modified AuNPs. In this study we demonstrate that the modification of AuNPs with diazonium salt precursors results in multilayer formation, as shown in Figure 3.01A. In order to provide evidence for such a claim we compared the thickness of diazonium-derived adlayers on gold nanoparticles to self-assembled

monolayers of aliphatic and aromatic thiolates (Figure 3.01B). [18-20] This comparison will provide a basis on which we can attribute spectroscopic and microscopic differences between the two modification schemes such as localized surface plasmon resonance (LSPR) shifts, complex vibrational modes, and film thicknesses to multilayer formation. For this purpose the thiol and diazonium ion derived layers are probed with extinction spectroscopy, surface-enhanced Raman scattering (SERS) and high-resolution transmission electron microscopy (TEM).

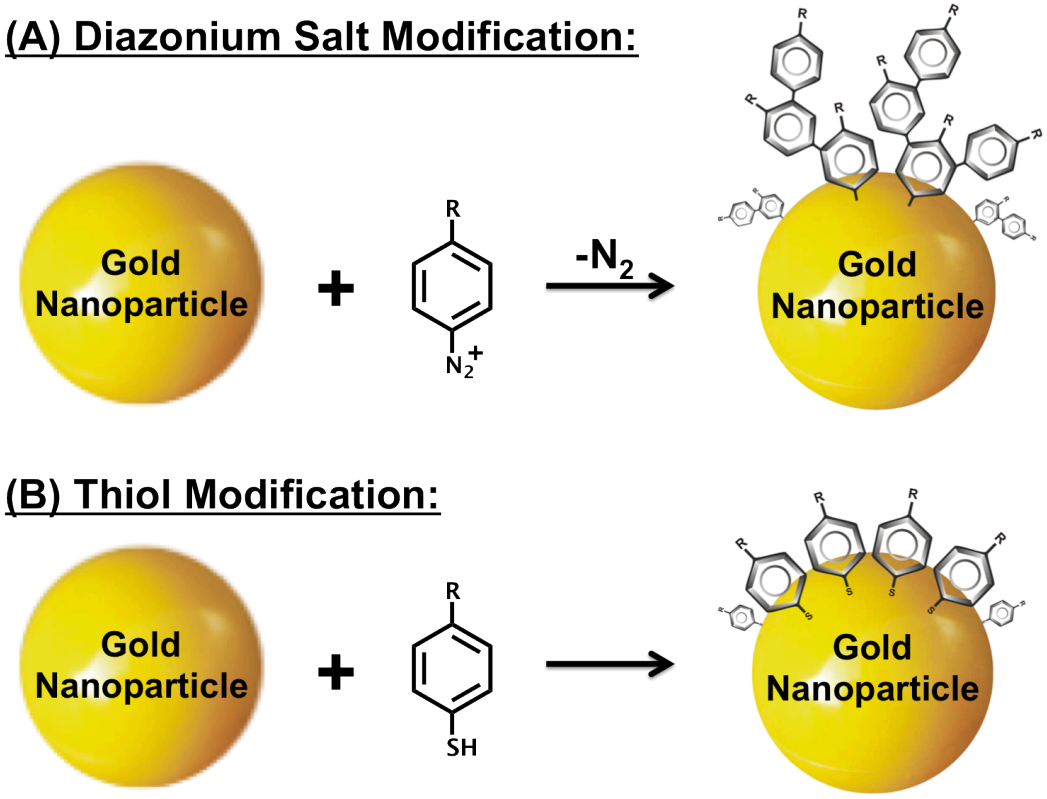

Figure 3.01. A reaction scheme shown for the spontaneous modification of gold nanoparticles with (A) diazonium ions forming a multi-layered film and (B) thiols forming a single-layered film.

3.2 EXPERIMENTAL

Reagents and Materials. 4-Nitrobenzenediazonium tetrafluoroborate, 97%, (dNB); 16-Mercaptohexadecanoic acid, 90% ($tC_{16}COOH$); and 4-Nitrobenzenethiol, 80%, (tNB) were obtained from Sigma-Aldrich and used as received. 4-Nitroazobenzene (dNAB) was synthesized according to a previously published procedure by Starkey.[21] Anhydrous acetonitrile (CH_3CN) was purchased from Caledon Laboratories. Sulphuric acid, 96%, and hydrogen peroxide, 30%, were obtained from Mallinckrodt. Premium microscope slides (3x1 inch) were received from Fisher Scientific. Citrate-capped 40 ± 3 nm gold nanoparticles (AuNPs) were purchased from BBInternational with a concentration of 9×10^{10} particles/mL. Deionized water with a resistivity of 18 MΩ-cm or better was obtained with a Millipore Milli-Q Plus purification system.

Gold nanoparticle modification. 40 nm AuNPs were modified by mixing 10 μL of 2 mM diazonium ion or thiol in acetonitrile with 1 mL of citrate-capped gold nanoparticle solution. The effect of precursor concentration was investigated by choosing two different concentrations in the modification procedure mentioned above for dNAB: a low concentration of 2 mM (LC-dNAB) and a high concentration of 10 mM (HC-dNAB). The reagents were left to incubate for 24 h after which time the nanoparticles were separated from solution *via* centrifugation at 8000 rpm for 10 min in an Eppendorf a5417R microcentrifuge. The supernatant was carefully removed with a micropipette and the AuNP pellet was redispersed in 1 mL of deionized water. A second centrifugation/cleaning step was added to

wash the particles further. The modified particles are stable and stored at 7 ºC until use.

Extinction Spectroscopy. All nanoparticle solutions were diluted by a factor of 2 with deionized water before analysis. The extinction spectra were obtained in transmission mode on a double-beam Perkin Elmer Lambda 35 spectrophotometer. The UV-vis spectra were scanned from 200 – 1100 nm with a scan rate of 960 nm/min. Deionized water was used as the blank.

Raman Spectroscopy. The gold nanoparticles were analyzed with surface-enhanced Raman scattering (SERS). A 20 μL volume of the modified AuNPs was deposited on a clean gold-coated microscope slide and analyzed. These gold-coated microscope slides were fabricated by coating a glass microscope slide with an adhesive layer of 5 nm Cr followed by 300 nm Au in a thermal evaporation system, Torr International. SERS spectra were recorded with a Renishaw inVia Raman microscope. Radiation of 785 nm from a high-performance, air-cooled diode laser was used for excitation. The SERS spectra of dNB, dNAB, tNB, and tC_{16}COOH modified 40 nm AuNPs were obtained by integrating the sample for 10 s with a laser power at the sample of 0.33 ± 0.02 mW. An Edmund Optics handheld laser power meter was used to measure the laser power at the sample. All spectra were collected with a 50× objective. Care was taken to visually deposit equivalent amounts of particles on the slide and to focus the laser beam in areas of similar nanoparticle density for each sample.

Transmission electron microscopy (TEM). The sample handling and TEM analysis was performed by Hui Qian at the Hitachi Electron Microscopy Products Centre (National Institute for Nanotechnology). TEM specimen were prepared by applying one drop of nanoparticle solution onto a silicon nitride membrane window grid. The excess solution was blotted with a filter paper after a period of one minute in order to provide time for AuNP adsorption to the grid. The grid was dried in air before being transferred to the ultra-high vacuum chamber. The images were collected on a 200kV JEOL2200FS field emission transmission electron microscope (TEM) equipped with an in-column omega type energy filter. An objective aperture and an energy filter slit were applied to obtain zero-loss bright field (BF)-TEM images, which enhanced the contrast of thin organic layers around the AuNPs.

3.3 RESULTS AND DISCUSSION

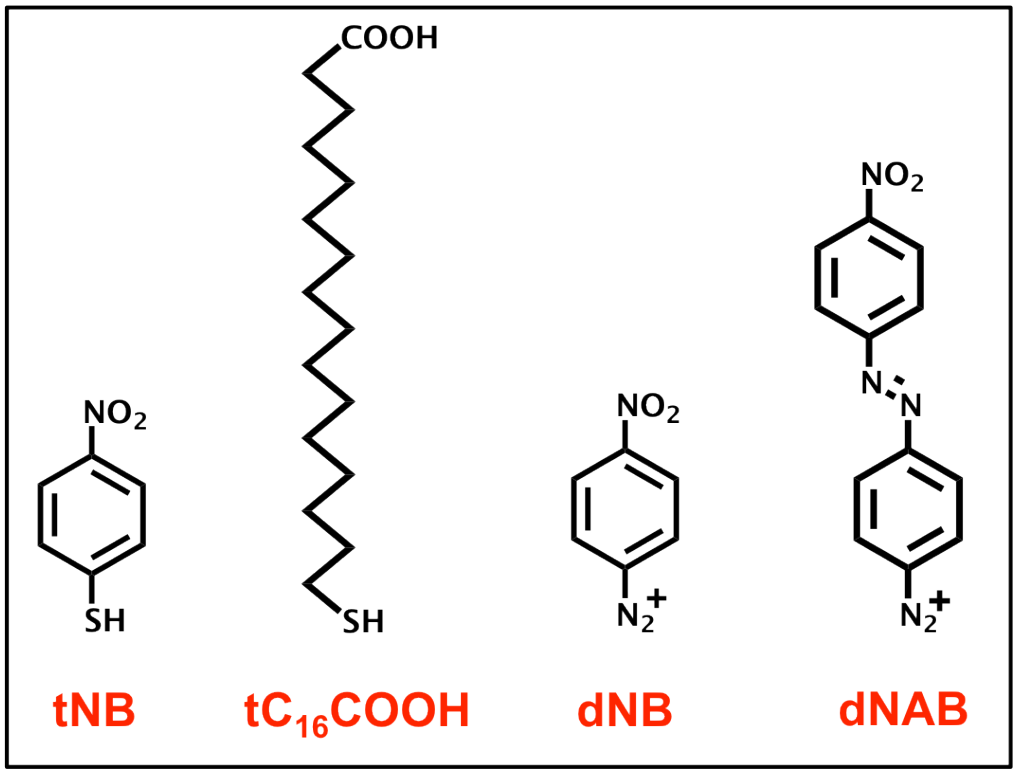

Figure 3.02. Molecules (drawn to scale) used in the modification of AuNPs from left to right: 4-nitrobenzenethiol (tNB), 16-mercaptohexadecanoic acid ($tC_{16}COOH$), 4-nitrobenzene diazonium salt (dNB), and 4-nitroazobenzene diazonium salt (dNAB).

In order to investigate the thickness of diazonium-derived organic films on gold nanoparticles we have characterized and compared a series of thiol and diazonium modified AuNPs, *i.e.* 4-nitrobenzenethiol (tNB), 16-mercaptohexadecanoic acid ($tC_{16}COOH$), 4-nitrobenzene diazonium salt (dNB), and 4-nitroazobenzene diazonium salt (dNAB). These four molecules (Figure

3.02) were chosen for two reasons: 1) to directly compare the two different modification schemes for similar structures using tNB and dNB, and 2) to provide examples of different molecular sizes for both thiol and diazonium derived layers. In the first case, any changes observed in TEM, extinction spectroscopy or SERS should result from differences in linkage and film formation of nitrobenzene on the gold nanoparticle surface. In the second case, changes in the resulting film thickness are strictly a consequence of molecular size, and this provides additional examples to support our findings. Lastly, dNAB is used to illustrate the capability of controlling layer thickness by varying diazonium salt concentration during NP modification from low concentration (LC-dNAB, ~20 μM) to high concentration (HC-dNAB, ~100 μM).

3.3.1. TEM film thickness measurements.

Modified gold nanoparticles were imaged with high-resolution TEM to quantitatively measure the layer thickness. Previously, TEM has been used to image citrate[22] and aliphatic thiols[20] on gold nanoparticles. Furthermore, aryl diazonium derived layers have been imaged on the surface of single-wall carbon nanotubes,[23] multi-walled carbon nanotubes, [24] germanium nanowires,[25] and gold nanoparticles synthesized in the presence of diazonium salt capping agents.[7] In the latter case, the high-resolution images indicated a monolayer of diazonium-derived decylbenzene on the AuNP surface, whereas nitrobiphenyl diazonium salt derived films formed multilayers on germanium wires with 2-4 nm in diameter.

So far there has been no direct evidence for multilayer formation on gold nanoparticles and applications of such diazonium-derived systems have been limited. We have used both silicon nitride membranes and carbon grids to support our samples and to assess beam induced carbon contamination that could result from a carbon support.[26]

Both thiolate monolayers and aryl diazonium derived films on AuNPs were imaged to compare a known system with diazonium-derived layers. AuNPs were incubated for the same time (24 h) and at the same concentration for both thiols and diazonium salts in order to facilitate a direct comparison. Figure 3.03 shows bright field (BF)-TEM images of the organic film surrounding the nanoparticle for each of the four molecules (tNB, $tC_{16}COOH$, dNB, and dNAB) and the citrate-capped starting material. Both the citrate-capped AuNPs (Figure 3.03A) and tNB (Figure 3.03C) display a thin film. This can be explained by the similar molecular diameters for citrate and nitrobenzene. In contrast, for mercapto-hexadecanoic acid ($tC_{16}COOH$, Figure 3.03B) we observe a thicker adlayer as a result of the increased molecular length. The organic layer thickness for dNB (Figure 3.03D) resembles that of $t_{16}COOH$ (Figure 3.03B) indicating multilayer formation, as mercaptohexadecanoic acid is 2-3 times the size of a nitrobenzene molecule. Thicker films are observed for LC-dNAB and HC-dNAB (Figure 3.03E and F). In addition, a direct comparison between the TEM images of thiol and diazonium derived films shows that diazonium derived layers produce thicker films. Table 3.1 lists the theoretical monolayer thickness, along with the measurements obtained from the TEM images for the various adsorbates.

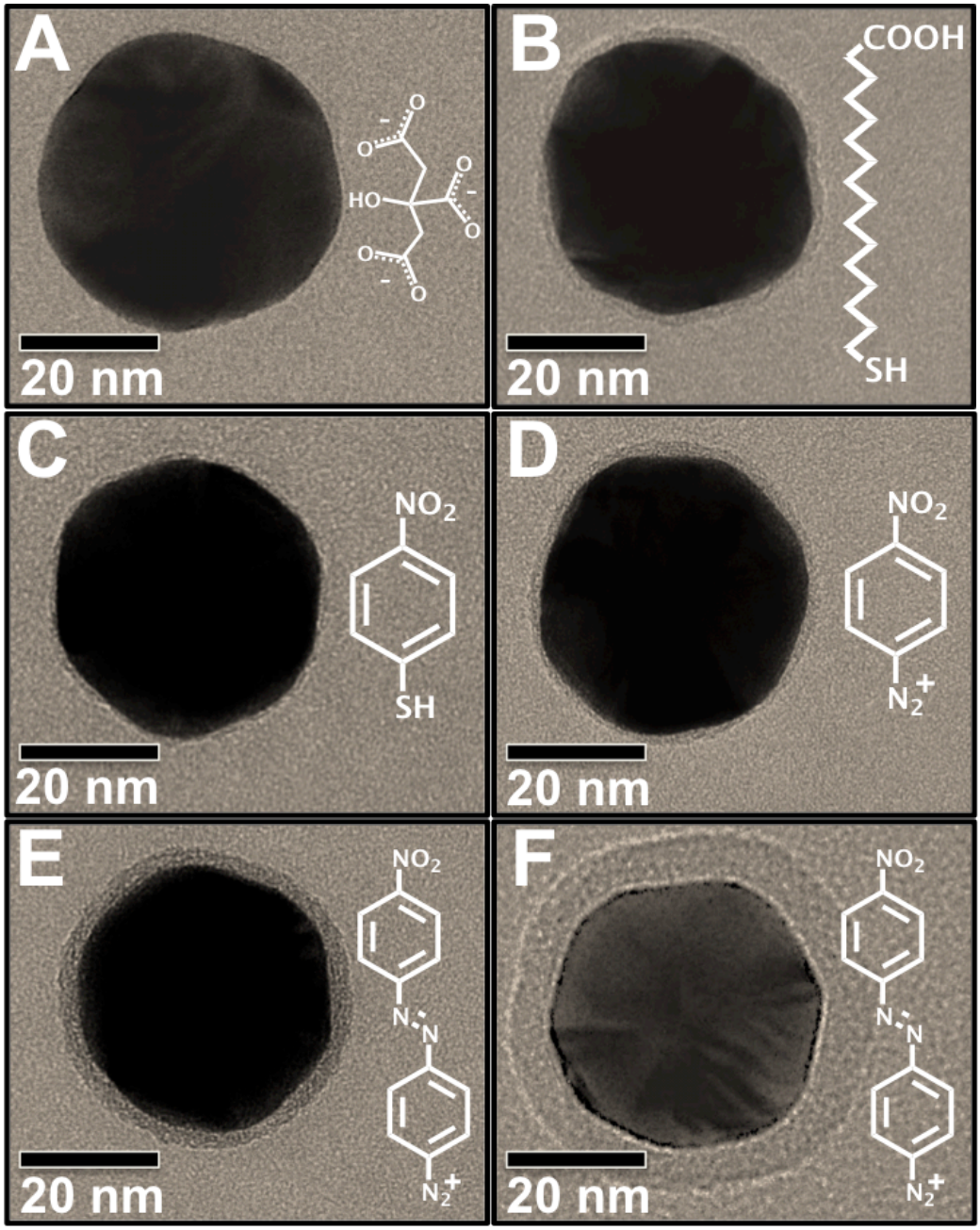

Figure 3.03. Bright field TEM (BF-TEM) images for 40nm gold nanoparticles capped with: (A) citrate, (B) mercaptohexadecanoic acid ($tC_{16}COOH$), (C) nitrobenzene thiol (tNB), (D) nitrobenzene diazonium salt (dNB), (E) low-concentration nitroazobenzene diazonium salt (LC-dNAB), and (F) high-concentration nitroazobenzene diazonium salt (HC-dNAB).

Table 3.1. Summary of calculated molecule diameters and experimental measurements taken from extinction spectroscopy and TEM images for 40 nm gold nanoparticles: citrate-capped (citrate), thiol modified (tNB and $tC_{16}COOH$), and diazonium salt modified (dNB and dNAB).

	calculated monolayer film thickness[a] (nm)	LSPR λ_{max} (nm)[b]	film thickness from TEM (nm)[b]
citrate	0.8[22]	526.6 ± 0.3	0.8 ± 0.1
tNB	0.6-0.9[27, 28]	527.9 ± 0.5	0.8 ± 0.1
$tC_{16}COOH$	2.2-2.5[29]	529.6 ± 0.1	2.2 ± 0.1
dNB	0.79[30]	531 ± 1	2.2 ± 0.2
LC-dNAB	1.4[13]	532 ± 1	4.0 ± 0.3
HC-dNAB	1.4[13]	535 ± 2	7.5 ± 0.4

[a] *Theoretical values for a monolayer thickness for the 5 molecules listed are based on reported values.*
[b] *The listed values are averages based on n=3 measurements for LSPR values and n=6 measurements for adlayer thicknesses.*

All nanoparticle precursors used in the two modification schemes presented here are capped with a monolayer of citrate that prevents aggregation. This layer binds to the gold surface through electrostatic interactions and has a thickness of approximately 0.8 nm,[22] in excellent agreement with our TEM derived thickness measurement of 0.8 ± 0.1 nm. The thin tNB adlayer measures 0.8 nm, which corresponds to a monolayer of nitrobenzene molecules on the surface. Similarly, the mercaptohexadecanoic acid ($tC_{16}COOH$) film measures 2.2 nm in diameter yielding monolayer coverage on the gold nanoparticle. The range of 2.2-2.5 nm listed for the theoretical monolayer height in Table 3.1 relates to the

orientation of these alkane thiols on the gold surface. It is well known that long-chained alkyl thiolates prefer a tilted orientation on planar gold and our results presented here show evidence for a similar orientation on the surface of gold nanoparticles.[31, 32]

In contrast, diazonium salts have been shown to produce multilayers on planar substrates. We observe dNB film thicknesses of 2.2 nm (Table 3.1), which theoretically corresponds to ≈3 layers of nitrobenzene. A similar result is achieved for dNAB, which exhibits an adlayer thickness of 4.0 nm for LC-dNAB. Furthermore, in most instances altering the incubation time and/or concentration controls the thickness of such a film. This effect was probed by changing the concentration for dNAB from 2 mM to 10 mM. The film thickness for the more concentrated dNAB measures 7.5 nm and amounts to approximately 5-6 layers of nitroazobenzene at the nanoparticle surface. Hence, there is a noticeable difference in film formation between thiols and diazonium salts on AuNPs and we have shown, for the first time, evidence for diazonium derived multilayer formation on gold nanoparticles. Furthermore, the difference in the initial diazonium salt concentration during the modification can significantly alter the resulting film diameter.

3.3.2 Extinction spectroscopy analysis.

A commonly used technique to monitor gold nanoparticle modification is extinction spectroscopy.[4, 33] The localized surface plasmon of AuNPs results in a

strong extinction band in the visible region near 520 nm as shown in Figure 3.04. The position of this extinction band is influenced by the nanoparticle size,[34, 35] shape,[34, 35] flocculation[36] and dielectric constant of the particle and the medium.[20, 35, 36] In the modification of the nanoparticle surface with organic molecules the dielectric constant of the surrounding medium is changed, which in turn affects the LSPR band position. This sensitivity towards changes in the dielectric constant of the surrounding medium upon addition of organic molecules to the nanoparticle surface can be employed as a diagnostic to verify a successful surface modification. This is demonstrated by equation 3-01 that was introduced in Chapter 1 and describes the effect of changes in refractive index and adsorbate thickness on the shift in λ_{max}.[4] The dielectric constant is the square of the complex refractive index.[37]

$$\Delta\lambda \approx m(n_{adsorbate} + n_{medium})\left(1 - e^{-2d/l_d}\right) \qquad (3\text{-}01)$$

Here, $\Delta\lambda$ is the wavelength shift, m is the sensitivity factor (nm/refractive index units), n refers to the refractive index of either the adsorbate or the surrounding medium, d is the adsorbate layer thickness (nm) and l_d is the electromagnetic field decay length (nm). Typically, the refractive index of an organic monolayer (1.5-1.6)[28, 38] is higher than the refractive index of a solvent (n_{water} = 1.33)[33] resulting in a red shift of the LSPR band.

The effect of film structure and thickness as measured by TEM on the extinction spectra is shown in Figure 3.04. All modified NPs exhibit extinction bands that are red-shifted from the original, citrate capped NPs. The amount that

each band is shifted scales with the film thickness. The larger shift induced by dNB relative to the equally thick $tC_{16}COOH$ is likely due to slight differences in refractive index. The refractive index of alkane thiol monolayers is typically estimated at 1.5, while a value of 1.62 has been reported for a tNB monolayer.[28] It is clear from Figure 3.04 that diazonium-derived films on AuNPs shift the position of the extinction band in a predictable way.

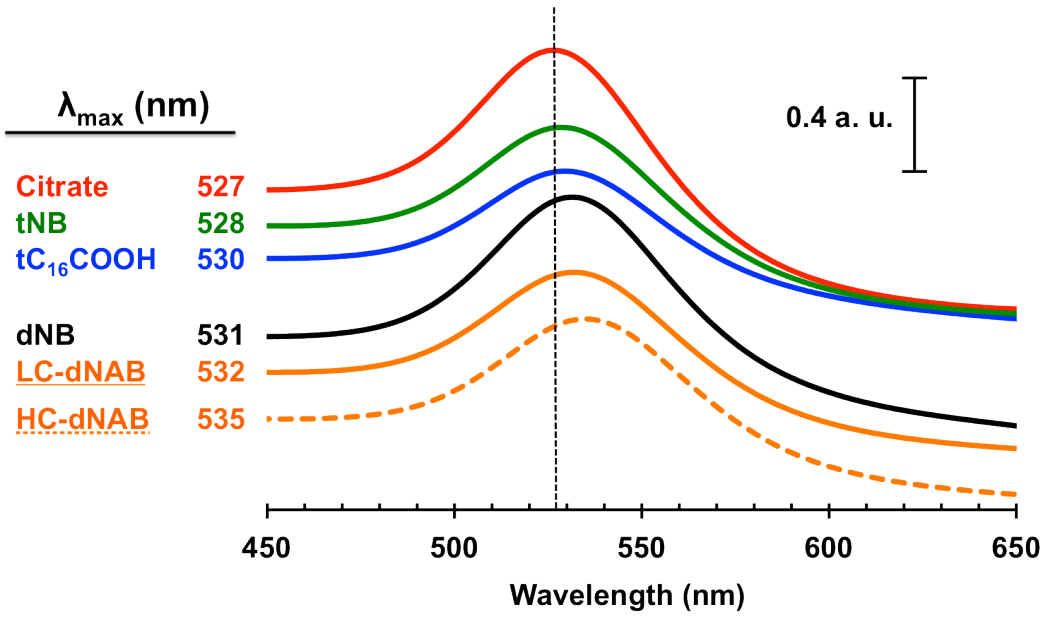

Figure 3.04. Extinction spectra for citrate-capped AuNPs (Citrate) and modified AuNPs with: nitrobenzene thiol (tNB), mercaptohexadecanoic acid ($tC_{16}COOH$), nitrobenzene diazonium salt (dNB), low-concentration nitroazobenzene diazonium salt (LC-dNAB), and high-concentration nitroazobenzene diazonium salt (HC-dNAB). The extinction maximum (λ_{max}) for each spectrum is listed on the left. The values are based on n=3 measurements and the uncertainties are listed in Table 3.1.

Other aspects of the extinction curves shown in Figure 3.04 include extinction magnitudes and LSPR band broadening. The absolute magnitudes are not consistent and this is most likely linked to the loss of nanoparticles during the centrifugation / cleaning steps in the modification procedure. In regards to the band broadening, all curves exhibit approximately similar width (60 nm) defined as the full-width-half-maximum (FWHM). This is a good indication that no aggregation during the NP modification has occurred.[20] Further, nanoparticle solution stability can be evaluated by monitoring the extinction spectrum in the region between 600 to 800 nm for the appearance of a second absorption band that indicates aggregation. There are no additional bands observed in any of the modified AuNP solutions (data not shown) and the resulting nanoparticles are stable for at least 1 month.

3.3.3 Surface-enhanced Raman scattering (SERS) characterization.

Raman spectroscopy is especially useful in providing structural information and due to narrow Raman bandwidths closely related compounds can be differentiated. Noble metal NPs are known to provide a strong electromagnetic field enhancement of Raman spectra of molecules adsorbed to their surface. SERS enhancements at AuNPs are as high as 10^6.[39] This enhancement is particularly prevalent within a few nanometers of the nanoparticle surface. The SERS spectra for all modified NPs are analyzed. A direct comparison between tNB and dNB modified NPs shows the effect of the multilayer structure on the SERS spectrum.

The SERS spectra for citrate, $tC_{16}COOH$, and dNAB modified AuNPs are displayed in Figure 3.05 and exhibit the typical vibrational bands for the respective molecules. Both hexadecanoic acid and citrate are poor Raman scatterers, which is manifested in the weak Raman band intensities observed. However, the main bands for citrate are present and agree with previously published literature.[22, 40] These bands consist of 1573 cm^{-1} for the asymmetric COO- stretching mode; two bands at 1436 cm^{-1} and 1313 cm^{-1} for the symmetric COO- stretching mode. Lastly, the C-C band at 1050 cm^{-1} and the C-O band at 855 cm^{-1} are also observed in the spectrum. This confirms the presence of citrate on the nanoparticle surface before these NPs were modified with thiols or diazonium salts. Similarly, we observe vibrational bands characteristic of a monolayer of mercaptohexadecanoic acid.[32, 41, 42] These bands consist of an O-H bend at 1435 cm^{-1}, C-OH stretch at 1295 cm^{-1}, chain rocking at 1112 cm^{-1}, and a C-S stretch at 710cm^{-1}. We also detect the symmetric and asymmetric CH_2 stretches at 2850 and 2895 cm^{-1}, respectively (data not shown).

Nitroazobenzene, on the other hand, is an excellent Raman scatterer[43] as shown by the intense SERS spectrum for the dNAB in Figure 3.05. To our knowledge, this is the first reported SERS spectrum of dNAB adsorbed to AuNPs and it adds to the list of diazonium precursors that can be used in the modification of gold nanoparticles. A comparison of the obtained SERS spectrum for dNAB to previously published Raman spectra by McCreery and co-workers of dNAB on carbon, silver, and titanium substrates shows many similarities.[43-45] The major Raman bands observed here are ring stretching (1589 cm^{-1}), N=N stretching (1452

cm^{-1}), symmetric NO_2 stretching (1342 cm^{-1}), and two complex stretching modes at 1142 cm^{-1} and 1107 cm^{-1} corresponding to ring-N=N and ring-NO_2 stretching, respectively.

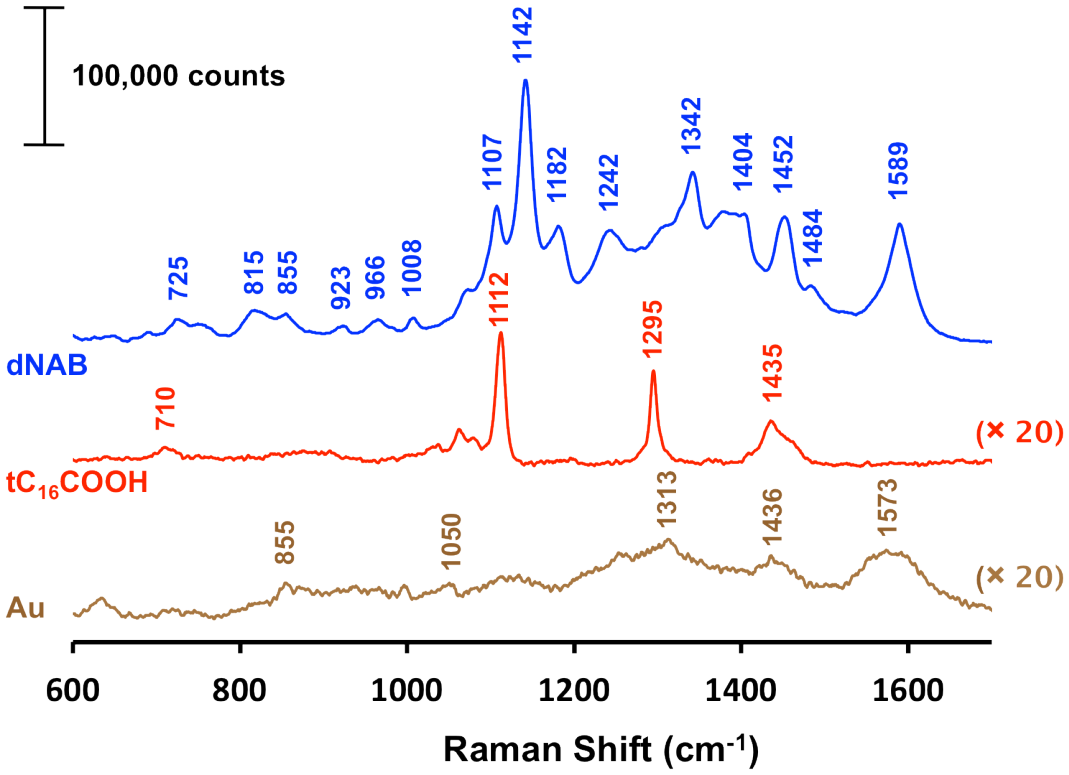

Figure 3.05. SERS spectra on 40nm AuNPs for diazonium salt derived nitroazobenzene (dNAB) in blue, thiol derived hexadecanoic acid ($tC_{16}COOH$) in red, and electrostatic bound citrate (Au) in brown. Both $tC_{16}COOH$ and Au spectra have been magnified by a factor of 20. A 785 nm laser was used to collect the SERS spectra.

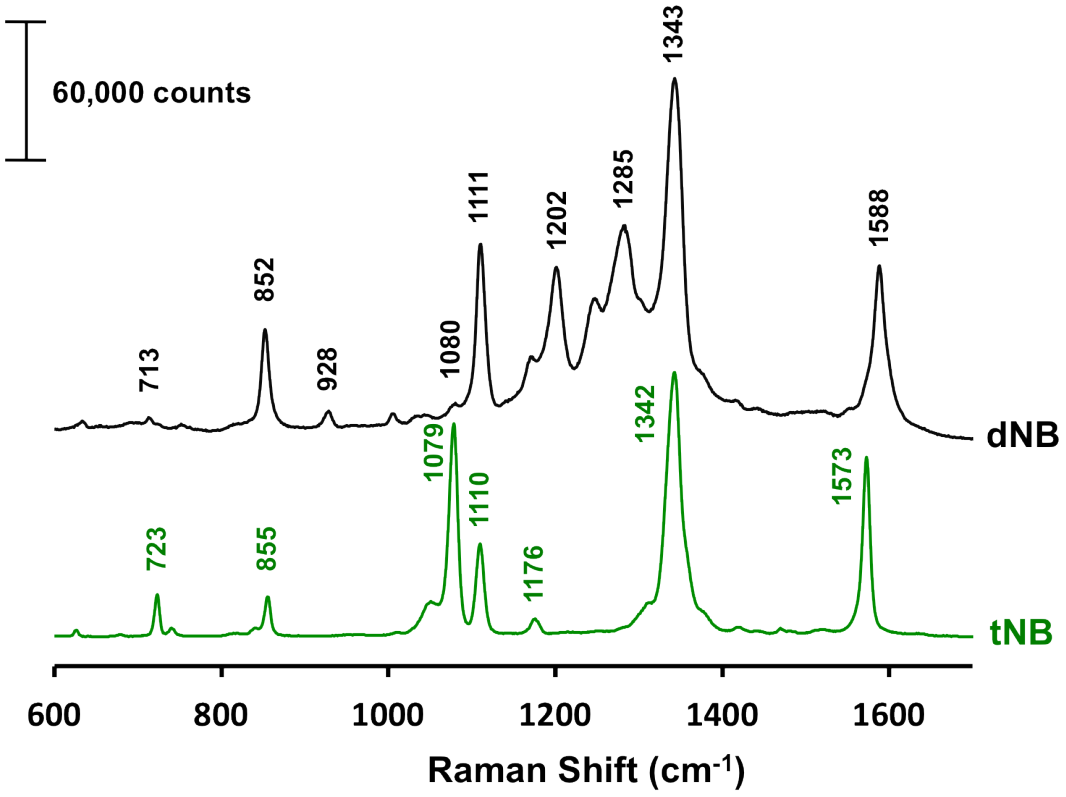

Figure 3.06. SERS spectra of diazonium derived 4-nitrobenzene (dNB) and thiol derived 4-nitrobenzene (tNB) on 40 nm gold nanoparticles. Both spectra were collected by irradiating visually equal amounts of AuNPs with a 785 nm laser. The spectra are offset and the major bands a labeled for comparison.

Table 3.2: Band assignments listed for the SERS spectra of nitroazobenzene (dNAB) on the surface of 40 nm AuNPs. Assignments were made based on published work.[43, 44]

Assignment	dNAB on AuNPs (cm^{-1})
Ring stretch	1589
Asym. NO_2 str.	1484
N=N str.	1452
N=N str. + ring str.	1404
Sym. NO_2 str.	1342
C-H i.p. bend	1242, 1182
Ring-N=N str.	1142
Ring-NO_2 str.	1107
Ring deformation	1008, 966
C-H bend	923
NO_2 bend	855
C-H deformation	815
C-H + C=C wag.	725

A complete compilation of the Raman bands in the region between 600 cm^{-1} and 1700 cm^{-1} is listed in Table 3.2, which includes the various bending and deformation modes of the NAB molecule. Although rather weak, we also observe

the asymmetric NO_2 stretch at 1484 cm^{-1} for nitroazobenzene, which was not detected by McCreery and co-workers. Another marked difference is the appearance of two bands instead of one for C-H i.p. bending (1242 cm^{-1} and 1182cm^{-1}) and ring deformation modes (1008 cm^{-1} and 966 cm^{-1}). We attribute these additional bands to dNAB multilayer formation on the gold nanoparticle surface, as indicated in the TEM section of this chapter. The reason behind the appearance of the band splitting in our results compared to McCreery's work is most likely due to the SERS enhancement at the AuNP surface, which greatly increases sensitivity in contrast to Raman spectra collected on planar substrates without any surface enhancement effects.

Pursuing the SERS characterization further, Figure 3.06 provides a direct comparison of a NB modified NPs with two different binding interactions. Differences in the SERS spectra can be attributed to structural differences in the adlayer. The major SERS bands for both tNB and dNB are summarized in Table 3.3. Two striking similarities between the SERS spectra are the intense ring-stretching mode at 1573 cm^{-1} for tNB and 1588 cm^{-1} for dNB, and the most prominent symmetric nitro stretch at 1342 cm^{-1} and 1343 cm^{-1}, respectively. The band positions are in agreement with previously published Raman spectra for nitrobenzene.[46-49] A cluster of peaks appearing in the region from 1200–1300 cm^{-1} are unique to dNB and have been assigned to ring breathing and C-H bending modes based on DFT calculations in our previous work.[50] We attribute these additional bands (1285 cm^{-1}, 1250 cm^{-1}, 1202 cm^{-1}) to complex vibrational modes within the multilayer structure of dNB.

Table 3.3. Band assignments listed for the SERS spectra of diazonium salt derived nitrobenzene (dNB) and thiol-derived nitrobenzene on the surface of 40 nm AuNPs. References 46, 47, and 48 were used for some assignments.

	Band position (cm^{-1})	
Assignment	**tNB on AuNPs**	**dNB on AuNPs**
Ring stretch	1573	1588
Symmetric NO_2 stretch	1342	1343
Ring breathing	–	1285
Ring breathing	–	1250
C-H i.p. bend	–	1202
C-H i.p. bend	1176	1170
C-N str. + ring str.	1110	1111
CH i.p. bend	1079	1080(w)
C-N stretch	1051	1040(w)/1049(w)
Ring breathing	1010(w)	1006(w)
C-H o.o.p. bend	933(w)	928
ONO scissor + ring str.	855	852
C-S stretch	723	–
C-H and C-C wagging	723	713
CCC i.p. bending	637	634

Additionally, the C-N stretch is split into two bands for dNB at 1040 cm^{-1} and 1049 cm^{-1}. There are two possible explanations for this splitting from the single band at 1051 cm^{-1} in tNB: effect of multilayer formation producing complex stretching modes, or an indication of azo coupling present in dNB films. [51] In terms of peak positioning, the bands in both spectra are usually within 10 cm^{-1}, as would be expected for closely related molecules. Lastly, the precursor for the dNB derived layers is a diazonium salt containing a N≡N bond, which is highly Raman active producing a stretch at 2300 cm^{-1}. This stretch is absent in our spectrum (not shown here) and provides further evidence for the radical attachment mechanism at the gold nanoparticle surface. Thus, the SERS spectra support the formation of a nitrobenzene film for both tNB and dNB, while the spectral comparison between the two molecules highlights differences in film structure and provides evidence for the formation of multilayers in dNB.

As an illustration of applicability, a variety of thiolates have been used as Raman reporters (molecules that a good Raman scatterers) in SERS based sandwich-type immunoassays for low-level detection of analytes and multiplexing.[1, 19] In this format the nanoparticle surface is coated with both a bioactive molecule, which binds specifically to the target analyte immobilized on a planar substrate, and a Raman active thiolate. Porter and co-workers have shown femtomolar detection of a prostate-specific antigen employing such bi-functional AuNPs[1] and they have shown the detection of four different antigens on the same chip employing four unique Raman scatterers.[52] Diazonium salt derived layers produce very similar SERS spectra compared to thiols as shown in Figure 3.06. In

both cases the Raman intensity and bandwidth are alike. However, there are differences in the SERS bands present due to structural changes of the adlayer. These spectral variations are sufficient to discriminate the two Raman active molecules. Consequently, diazonium salts provide new labels for multiplexing in SERS-based bioassays.

3.4 CONCLUSION

In conclusion, the comparison of thiol and diazonium derived layers on gold nanoparticles provides an excellent basis to explore structural differences in the two different modification schemes. The fact that thiol modification results in a thiolate monolayer on gold nanoparticles makes it possible to attribute differences observed in extinction spectroscopy, SERS, and TEM to multilayer formation. This is the first demonstration of diazonium salt derived multilayer formation on AuNPs. The thickness of this film can be controlled by modification conditions such as concentration as was shown for dNAB in this study.

Furthermore, we have presented a direct comparison of SERS spectra for nitrobenzene for the two modification schemes. The differences in the two spectra can now with certainty be assigned to complex vibrational modes stemming from multilayer formation for dNB, and the similarities can be exploited in applications such as SERS based immunoassays to expand on the number of Raman reporters available. Lastly, the structural differences resulting from the two different modification techniques will provide researchers with additional methods to control adlayer thickness on gold nanoparticles to suit specific applications.

3.5 REFERENCES

1. Grubisha, D. S.; Lipert, R. J.; Park, H. Y.; Driskell, J.; Porter, M. D. *Anal. Chem.* **2003,** 75, (21), 5936-5943.
2. Englebienne, P. *Analyst* **1998,** 123, (7), 1599-1603.
3. Grabar, K. C.; Freeman, R. G.; Hommer, M. B.; Natan, M. J. *Anal. Chem.* **1995,** 67, (4), 735-743.
4. Anker, J. N.; Hall, W. P.; Lyandres, O.; Shah, N. C.; Zhao, J.; Van Duyne, R. P. *Nat. Mater.* **2008,** 7, (6), 442-453.
5. El-Sayed, I. H.; Huang, X. H.; El-Sayed, M. A. *Nano Lett.* **2005,** 5, (5), 829-834.
6. Popovtzer, R.; Agrawal, A.; Kotov, N. A.; Popovtzer, A.; Balter, J.; Carey, T. E.; Kopelman, R. *Nano Lett.* **2008,** 8, (12), 4593-4596.
7. Mirkhalaf, F.; Schiffrin, D. J. *Langmuir* **2010,** 26, (18), 14995-15001.
8. Buriak, J. M. *Chem. Rev.* **2002,** 102, (5), 1271-1308.
9. Downard, A. J. *Electroanal.* **2000,** 12, (14), 1085-1096.
10. Bernard, M. C.; Chausse, A.; Cabet-Deliry, E.; Chehimi, M. M.; Pinson, J.; Podvorica, F.; Vautrin-Ul, C. *Chem. Mater.* **2003,** 15, (18), 3450-3462.
11. Kariuki, J. K.; McDermott, M. T. *Langmuir* **1999,** 15, (19), 6534-6540.
12. Kariuki, J. K.; McDermott, M. T. *Langmuir* **2001,** 17, (19), 5947-5951.
13. Anariba, F.; DuVall, S. H.; McCreery, R. L. *Anal. Chem.* **2003,** 75, (15), 3837-3844.
14. Pinson, J.; Podvorica, F. *Chem. Soc. Rev.* **2005,** 34, (5), 429-439.

15. Lehr, J.; Williamson, B. E.; Flavel, B. S.; Downard, A. J. *Langmuir* **2009,** 25, (23), 13503-13509.

16. Adenier, A.; Combellas, C.; Kanoufi, F.; Pinson, J.; Podvorica, F. I. *Chem. Mater.* **2006,** 18, (8), 2021-2029.

17. Mahouche-Chergui, S.; Gam-Derouich, S.; Mangeney, C.; Chehimi, M. M. *Chem. Soc. Rev.* **2011,** 40, (7), 4143-4166.

18. Brust, M.; Fink, J.; Bethell, D.; Schiffrin, D. J.; Kiely, C. *J. Chem. Soc. Chem. Comm.* **1995**, (16), 1655-1656.

19. Ni, J.; Lipert, R. J.; Dawson, G. B.; Porter, M. D. *Anal. Chem.* **1999,** 71, (21), 4903-4908.

20. Weisbecker, C. S.; Merritt, M. V.; Whitesides, G. M. *Langmuir* **1996,** 12, (16), 3763-3772.

21. Starkey, E. B. *Org. Synth.* **1939,** 19, 40-42.

22. Mabuchi, M.; Takenaka, T.; Fujiyoshi, Y.; Uyeda, N. *Surf. Sci.* **1982,** 119, (2-3), 150-158.

23. Bahr, J. L.; Yang, J. P.; Kosynkin, D. V.; Bronikowski, M. J.; Smalley, R. E.; Tour, J. M. *J. Am. Chem. Soc.* **2001,** 123, (27), 6536-6542.

24. Matrab, T.; Chancolon, J.; L'hermite, M. M.; Rouzaud, J. N.; Deniau, G.; Boudou, J. P.; Chehimi, M. M.; Delamar, M. *Colloids Surf. A* **2006,** 287, (1-3), 217-221.

25. Collins, G.; Fleming, P.; O'Dwyer, C.; Morris, M. A.; Holmes, J. D. *Chem. Mater.* **2011,** 23, (7), 1883-1891.

26. Egerton, R. F.; Li, P.; Malac, M. *Micron* **2004,** 35, (6), 399-409.

27. Shewchuk, D. M.; McDermott, M. T. *Langmuir* **2009,** 25, (8), 4556-4563.

28. Jakubowicz, A.; Jia, H.; Wallace, R. M.; Gnade, B. E. *Langmuir* **2005,** 21, (3), 950-955.

29. Meldrum, F. C.; Flath, J.; Knoll, W. *Langmuir* **1997,** 13, (7), 2033-2049.

30. Brooksby, P. A.; Downard, A. J. *Langmuir* **2004,** 20, (12), 5038-5045.

31. Bain, C. D.; Troughton, E. B.; Tao, Y. T.; Evall, J.; Whitesides, G. M.; Nuzzo, R. G. *J. Am. Chem. Soc.* **1989,** 111, (1), 321-335.

32. Nuzzo, R. G.; Dubois, L. H.; Allara, D. L. *J. Am. Chem. Soc.* **1990,** 112, (2), 558-569.

33. Lopatynskyi, A. M.; Lopatynska, O. G.; Guo, L. J.; Chegel, V. I. *IEEE Sens. J.* **2011,** 11, (2), 361-369.

34. Jain, P. K.; Lee, K. S.; El-Sayed, I. H.; El-Sayed, M. A. *J. Phys. Chem. B* **2006,** 110, (14), 7238-7248.

35. Lee, K. S.; El-Sayed, M. A. *J. Phys. Chem. B* **2005,** 109, (43), 20331-20338.

36. Malinsky, M. D.; Kelly, K. L.; Schatz, G. C.; Van Duyne, R. P. *J. Am. Chem. Soc.* **2001,** 123, (7), 1471-1482.

37. Ohki, S. *J. Theor. Biol.* **1968,** 19, (1), 97-&.

38. Porter, M. D.; Bright, T. B.; Allara, D. L.; Chidsey, C. E. D. *J. Am. Chem. Soc.* **1987,** 109, (12), 3559-3568.

39. Baker, G. A.; Moore, D. S. *Anal. Bioanal. Chem.* **2005,** 382, (8), 1751-1770.

40. Zou, X. Q.; Ying, E. B.; Dong, S. J. *Nanotechnology* **2006,** 17, (18), 4758-4764.

41. Creager, S. E.; Steiger, C. M. *Langmuir* **1995,** 11, (6), 1852-1854.

42. Morales-Cruz, A. L.; Tremont, R.; Martinez, R.; Romanach, R.; Cabrera, C. R. *Appl. Surf. Sci.* **2005,** 241, (3-4), 371-383.

43. Liang, H. H.; Tian, H.; McCreery, R. L. *Appl. Spectrosc.* **2007,** 61, (6), 613-620.

44. Itoh, T.; McCreery, R. L. *J. Am. Chem. Soc.* **2002,** 124, (36), 10894-10902.

45. Mahmoud, A. M.; Bergren, A. J.; McCreery, R. L. *Anal. Chem.* **2009,** 81, (16), 6972-6980.

46. Futamata, M. *J. Phys. Chem.* **1995,** 99, (31), 11901-11908.

47. Skadtchenko, B. O.; Aroca, R. *Spectrochim. Acta, Part A* **2001,** 57, (5), 1009-1016.

48. Clarkson, J.; Smith, W. E. *J. Mol. Struct.* **2003,** 655, (3), 413-422.

49. Shin, K. S.; Lee, H. S.; Joo, S. W.; Kim, K. *J. Phys. Chem. C* **2007,** 111, (42), 15223-15227.

50. Laurentius, L.; Stoyanov, S. R.; Gusarov, S.; Kovalenko, A.; Du, R.; Lopinski, G. P.; McDermott, M. T. ACS Nano **2011**, 5, (5), 4219-4227.

51. Laforgue, A.; Addou, T.; Belanger, D. *Langmuir* **2005,** 21, (15), 6855-6865.

52. Wang, G. F.; Park, H. Y.; Lipert, R. J. *Anal. Chem.* **2009,** 81, (23), 9643-9650.

Chapter 4:

Nanoparticle Adsorption to Modified Transparent Substrates: Method Development towards Biosensing

4.1 INTRODUCTION

The biosensing field has been re-vitalized with the incorporation of nanoparticles and nanostructures.[1-3] Specifically gold nanoparticles have found applications in Raman-based immunoassays,[4] optical enzyme-linked immunosorbent assay (ELISA),[5] DNA hybridization studies,[6] surface plasmon resonance (SPR)[7-12] and localized surface plasmon resonance (LSPR) sensing.[13, 14] The work described in this chapter will focus on LSPR sensing and lay the groundwork for a simplified approach to detect biomolecules in a sandwich immunoassay format. LSPR is described as the collective oscillation of conductance electrons as a result of exposure to electro-magnetic radiation. In UV-vis spectroscopy of gold nanoparticles this effect leads to the appearance of an LSPR band in the visible region and the theory that governs the interaction of light with metal nanoparticles will be discussed below.

In 1908 Gustav Mie formulated an approach derived from Maxwell's equations to predict the influence of electromagnetic radiation on colloids.[15-19] When light interacts with a particle the likelihood of an interaction taking place is summed up in the extinction cross section σ_{ext}, which is made up of two terms, namely σ_{abs} (absorbance) and σ_{sca} (scattering), as shown by equation 4-01.

$$\sigma_{ext} = \sigma_{abs} + \sigma_{sca} \qquad (4\text{-}01)$$

The extinction cross section can be calculated from equation 4-02, where *k* refers to the wavevector, and (a_L + b_L) is a simplification of a mathematical expression that includes the indexes of refraction for the particle and the surrounding medium, size parameters, and Riccati-Bessel cylindrical functions. The σ_{ext} expression also contains the term *L* that includes dipolar, quadrupolar, and higher-order modes.

$$\sigma_{ext} = \frac{2\pi}{|k|^2}\sum_{L=1}^{\infty}(2L+1)\,Re\{a_L + b_L\} \qquad (4\text{-}02)$$

There is however an approximation that can be used for particle sizes much smaller than the resonance wavelength. The nanoparticles used in this study range from 10-100 nm and fall within this quasi-static regime. In this regime higher order excitation modes are absent and the dipole mode dominates.[16] This simplifies the expression for the extinction cross section as shown by equation 4-03.

$$\sigma_{ext}(\omega) = 12\frac{\omega}{c}{\varepsilon_m}^{3/2}\pi R^3\frac{\varepsilon_2(\omega)}{[\varepsilon_1(\omega)+2\varepsilon_m]^2+\varepsilon_2(\omega)^2} \qquad (4\text{-}03)$$

Close examination of the expression for σ_{ext} in equation 4-03 reveals that the extinction cross section is dependent on the particle volume (R^3), the complex dielectric function of the particle (ε_1 *and* ε_2), and the real dielectric function of the surrounding medium (ε_m). A study conducted by Johnson and Christy has demonstrated the effect of changes in the particle dielectric function.[20] For gold and silver, both the real and imaginary part of the dielectric function are significantly different resulting in distinct wavelength maxima or resonance wavelengths. The dependence on R^3 also implies that larger nanoparticles have a higher extinction cross section and result in greater absorption/scattering of light.

The σ_{ext} can be related to the unitless extinction read-out in an UV-vis experiment by equation 4-04 that is derived from the Beer-Lambert law.[21] In this equation the extinction cross section takes area units (cm^2), path length l is in (cm), and concentration, C, is in the form of number density (cm^{-3}).

$$Extinction_{\lambda} = 0.434 C l \sigma_{ext} \qquad (4\text{-}04)$$

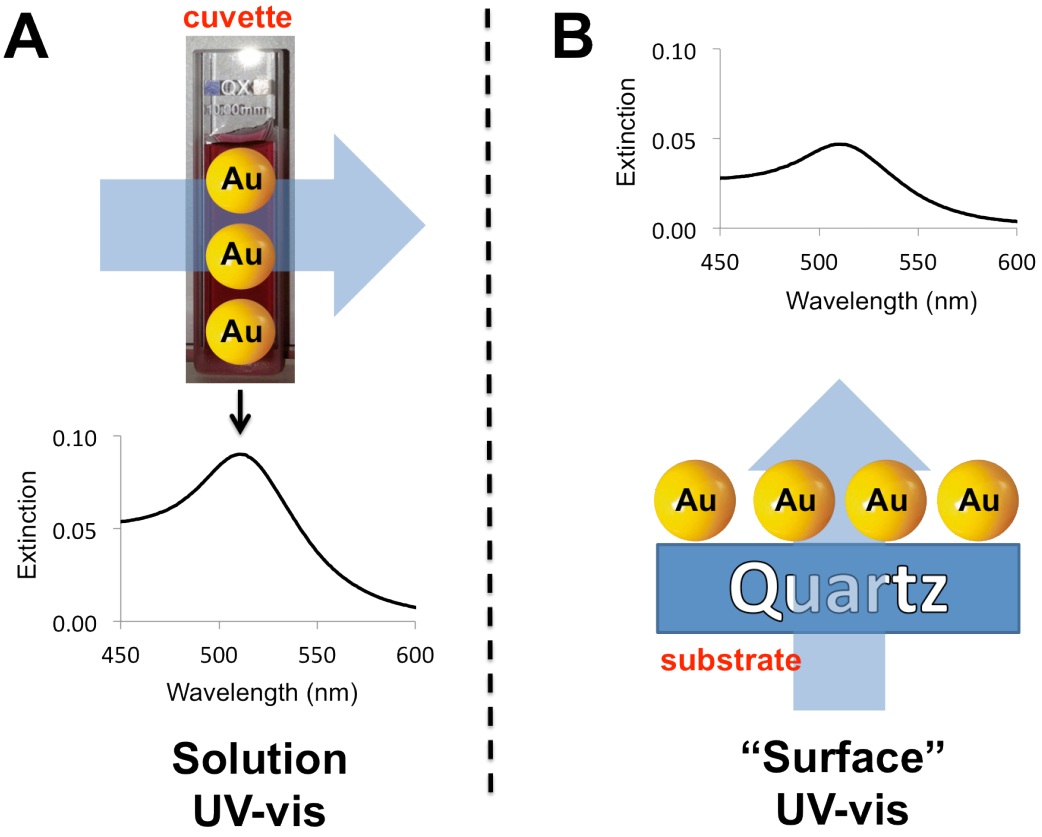

Figure 4.01. Schematic representation of the experimental design for an extinction measurement to evaluate the quantity of nanoparticles present in (a) solution and (b) immobilized on a transparent substrate.

Traditionally, the majority of extinction measurements are carried out in solution (Figure 4.01A), but more recently nanoparticles have been adsorbed to solid supports to serve as sensing platforms in bioassays. This requires extinction measurements of immobilized nanoparticles on transparent substrates (glass or quartz) as shown in Figure 4.01B. Typically, these sensing platforms detect binding of organic- or bio-molecules by relying on a shift in the NP extinction maximum due to refractive index changes as adsorption to the nanoparticle surface takes place. We took a different approach that utilizes nanoparticles as labels. In this fashion, the LSPR band magnitude is used for quantitation. The magnitude can be related to the number of nanoparticles present on the substrate surface, which in turn can be related to the number of analyte molecules captured.

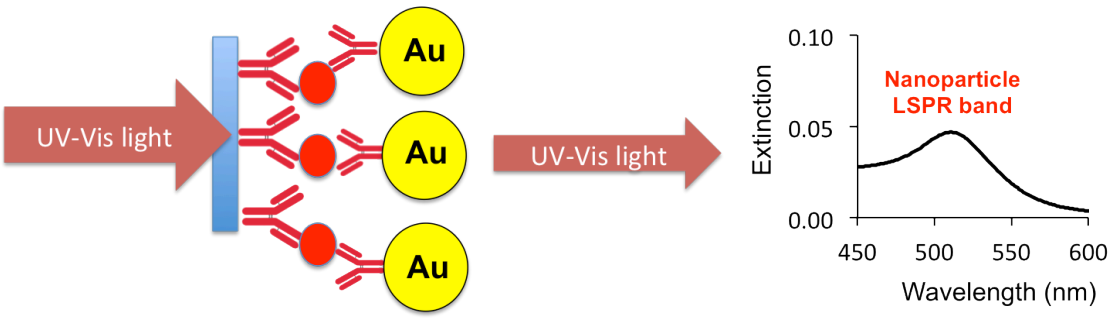

Figure 4.02. An outline showing a sandwich immunoassay that detects binding based on the nanoparticle density on the surface measured by the LSPR band intensity.

A schematic of this approach is illustrated in Figure 4.02 in which a sandwich immunoassay detects binding through the use of antibody coated NP labels. For the purpose of biosensing applications, we needed to explore our ability to quantitate nanoparticle adsorption on a solid support by extinction spectroscopy. Once the detection method was thoroughly studied, then the nanoparticle labels were incorporated into a sandwich immunoassay as shown in Figure 4.02 (Chapter 5).

Several researchers have studied the adsorption of AuNPs over the past 15 years, and the study presented here will serve to reproduce and expand on this work to establish a foundation for our biosensing application. In 1995, Natan and coworkers successfully demonstrated adsorption of gold nanoparticles on modified quartz to produce surface-enhanced Raman scattering (SERS) active substrates.[22] Other researchers have since studied the adsorption of gold nanoparticles to various substrates by surface-enhanced infrared absorption spectroscopy,[23] quartz crystal microbalance,[24, 25] SERS,[24] and extinction spectroscopy.[26, 27] The majority of work in this area investigated the adsorption kinetics and applications of such AuNP adsorbed films; however, low particle densities that would commonly be found in sandwich immunoassays were not considered. For such systems a more comprehensive study was necessary. In order to quantify the adsorption of various sizes of NPs to modified quartz, the nanoparticle densities obtained from scanning electron microscopy (SEM) were compared to LSPR band magnitudes obtained from UV-vis spectroscopy. Further, the goal of this work was to evaluate the possibility of monitoring more than one

type of metallic nanoparticle at the quartz surface simultaneously by UV-vis spectroscopy. A two-color detection would be beneficial for biosensing applications as there is a drive for techniques capable of analyzing multiple analytes at the same time. The work presented here lays the groundwork for Chapter 5, which describes the incorporation of nanoparticles as labels in biosensing.

4.2 EXPERIMENTAL

Reagents and Materials. N-(2-aminoethyl)-11-aminoundecyltrimethoxy silane (AUTS) was obtained from Gelest. Reagent-grade methanol, sulphuric acid, 96%, and hydrogen peroxide, 30%, were purchased from Caledon Laboratories. All substrates are made out of GE-124 fused quartz with a dimension of 1×1 cm supplied by Technical Glass. Citrate-capped 10, 40, 60, 100 nm gold nanoparticles (AuNPs) and 20, 40 nm silver nanoparticles (AgNPs) were purchased from BBInternational. In addition 20 nm silver nanoparticles were synthesized following the procedure published by Chen and Lu.[28] Briefly, $AgNO_3$ (0.012g) was added to a 90 °C mixture of 50 mL ethylene glycol and 0.026 g of sodium citrate. After stirring for 10 min the solution turned dark yellow and was consequently diluted with 100 mL of deionized water and stored at 4 °C until use. Deionized water with a resistivity of 18 MΩ-cm or better was obtained with a Millipore Milli-Q Plus purification system.

Silane Modification. All quartz substrates were cleaned in a hot piranha solution consisting of 4:1 (96% sulfuric acid: 30% hydrogen peroxide) for 30 minutes followed by thorough rinsing with deionized water and drying under a stream of argon gas. *Warning: Piranha solution should be handled with extreme care; it reacts violently with organic materials, presenting an explosion danger.* The cleaned substrates were placed elevated inside a glass petri dish in a furnace set to 90 °C. The silane solution was added to the petri dish (1-2 mL) and was not in direct contact with the substrates. A 1 h vapor deposition of the silanes

followed, after which the modified substrates were thoroughly rinsed with methanol, dried under a stream of argon gas and left to cure for 1-2 h before use.

Atomic force microscopy (AFM). In order to determine the silane layer thickness, a 2×2 μm area on the AUTS modified quartz surface was first imaged in tapping mode and then a 1×1 μm area was "scratched" by 10 cycles at 5 Hz in contact mode. Afterwards the "scratched" area was re-imaged in tapping mode and a height profile showed the difference between the undisturbed and disturbed area corresponding to the silane film thickness on the surface. The same procedure was repeated for an unmodified quartz substrate in order to determine if the applied force during contact mode caused damage to the quartz.

The above-mentioned work was carried out on a Digital Instruments Nanoscope III Multimode microscope using an Olympus Si cantilever with a spring constant of 2 N/m. The oscillation frequency used for tapping mode was 72 ± 4 kHz and a contact force of 0.3 μN was used for all contact mode experiments corresponding to a setpoint of 2.000 V. The applied force, $F_{applied}$, was determined using equation 4-05,

$$F_{applied} = \frac{V_S - V_B}{S} k_{spring} \qquad (4\text{-}05)$$

where V_S is the setpoint voltage used in contact-mode, V_B is the voltage required to break the tip away from the surface (-0.3384 V), and S is the cantilever sensitivity to bending (0.01387 V/nm), and k_{spring} is the spring constant for the cantilever (2 N/m).

Static sessile contact angle. All contact angle measurements were carried out on a Ramé-hart model 590 automated goniometer with DROPimage advanced version 2.4. Both unmodified and modified quartz substrates were analyzed by placing a drop of deionized water with a syringe needle on the surface and immediately capturing an image of the drop, which was used to calculate the contact angle the drop makes with the substrate. Measurements were repeated for a minimum of 3 samples.

X-ray photoelectron spectroscopy (XPS). The XPS analysis was performed at the Alberta Centre for Surface Engineering and Science (ACSES) using an AXIS Ultra Spectrometer (Kratos Analytical). The source, a monochromated Al Kα source (hν = 1486.6 eV), was operated at 210 W, and the analytical chamber maintained a base pressure lower than 4 x 10^{-7} Pa for all measurements. The spot size for all samples was set to 400×700 μm with a hemispherical analyzer operated in fixed analyzer transmission (FAT) mode. High-resolution spectra were collected for C1s, O1s, N1s and Si2p with pass energy of 20 eV and a step size of 0.1 eV. All spectra were referenced to the C1s peak at 284.8 eV and charge neutralization was omitted. The XPS data was processed with CasaXPS version 2.3.15.

Nanoparticle adsorption. The N-(2-aminoethyl)-11-aminoundecyltrimethoxy silane modified substrates were exposed to various nanoparticle solutions. Typically, adsorption was carried out by exposing the surface of a 1×1 cm substrate to 1-2 mL of NP solution for 24 h, followed by rinsing with deionized water / drying under a stream of argon gas. Both

nanoparticle solution concentration and immersion times were varied in studying adsorption behavior. Adsorbed NPs at the substrate surface were stable for several weeks without aggregation.

Extinction Spectroscopy. All nanoparticle solutions were diluted by a factor of 2 with deionized water before analysis. The extinction spectra for both solution-based and adsorbed nanoparticles were obtained in transmission mode on a double-beam Perkin Elmer Lambda 35 spectrophotometer with a photodiode detector. The UV-vis spectrum was scanned from 200 to 1100 nm with a scan rate of 960 nm/min. Deionized water or a bare quartz slide were used as the blank.

Scanning Electron Microscopy (SEM). All quartz substrates were coated with a 5 nm chromium film prior to SEM analysis to avoid charging. The Cr film was sputtered at a rate of 0.4 Å/s by bombarding a Cr target with a 8 keV and 300 μA electron beam in a Gatan precision etching coating system model 682. SEM images were either collected by Jane Cao on a Hitachi S4800 Field Emission SEM in the Hitachi Electron Microscopy Products Centre (NINT), or by staff on a JEOL Field Emission Auger Microprobe JAMP 9500F at ACSES. Image acquisition on the Hitachi SEM was carried out with a 10.0 kV accelerating voltage and a 15 μA emission current. Image acquisition on the JEOL was carried out using a 25.0 kV accelerating voltage and a 8 nA emission current. In both cases the working distance was approximately 20-24 mm.

4.3 RESULTS AND DISCUSSION

The following discussion is divided in several sections that describe the approach taken to quantify nanoparticles on transparent substrates. The modification of quartz will be discussed first and evidence for the successful surface modification will be presented. Then a description of a solution based UV-vis analysis of various nanoparticle solutions and mixtures follows. Lastly, both gold and silver NP adsorption on amine terminated silanes and their quantification based on LSPR intensities will be discussed.

4.3.1 Silane modification

Commercially available nanoparticles are typically coated with citrate molecules resulting in a negative charged surface that repels the individual nanoparticles from each other and prevents aggregation in solution. In order to capture NPs on a planar substrate the surface is modified to either enhance electrostatic interactions or to utilize specific metal-ligand interactions. Functional groups are chosen that either have a high affinity to gold (–SH and –CN)[22] or that yield in a positive surface charge ($-NH_2$)[29] at neutral-acidic pH which can electrostatically bind the negatively charged NPs. The most prevalent method to modify quartz is silane chemistry that typically uses trimethoxy- or trichlorosilanes.[30-36] Alkylsilanes self-assemble at hydroxylated surfaces to form relatively ordered monolayers driven by hydrophobic interactions between the alkyl chains. The two methods for film formation are solution or vapor based depositions. Especially in solution depositions from organic solvents the amount

of water needs to be stringently controlled in order to form reproducible layers. Excess water can lead to silane aggregates in solution that then deposit on the substrate forming disordered films.[30, 36-38] Several reports claim that chemical vapor deposition (CVD) results in more reproducible, ordered layers as a result of more controllable deposition conditions; solvent impurities are virtually eliminated and water content can be better controlled.[39-41] To this end the silane vapor deposition was chosen for this study. Lastly, a long chained amine terminated silane was selected in order to minimize hydrolysis of the formed film

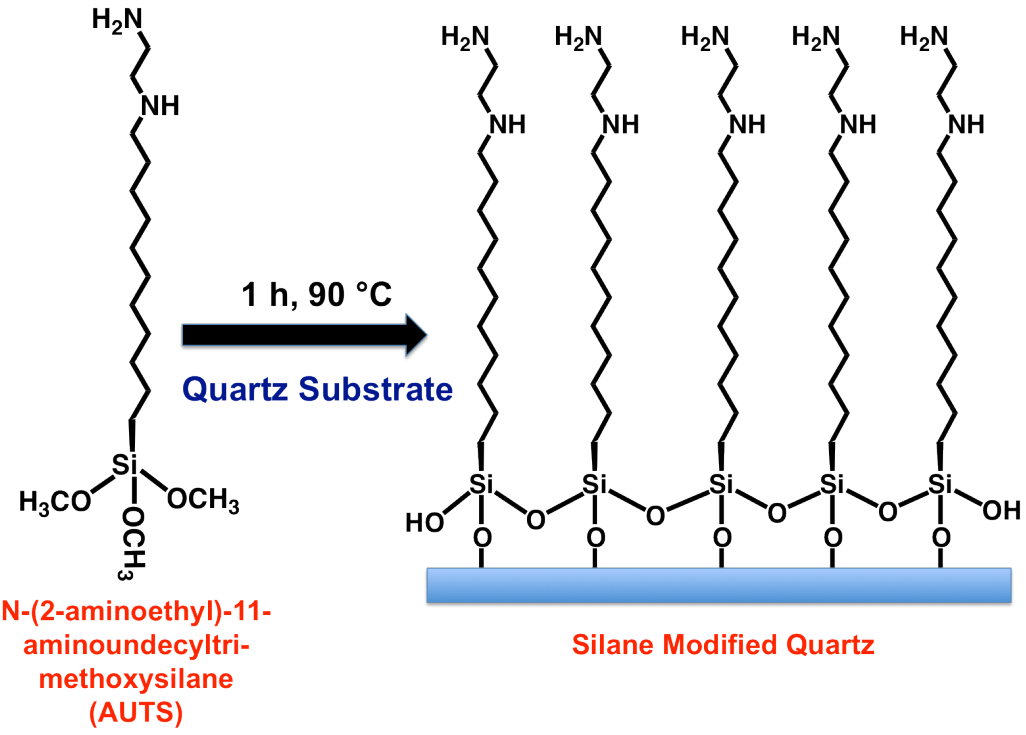

Figure 4.03. The formation of a vapor deposited silane layer on a quartz substrate.

due to exposure to aqueous nanoparticle solutions.[42] Figure 4.03 shows the formation of an ideal silane film with individual silane molecules cross-linked on quartz from CVD. The modified quartz substrates were characterized with contact angle measurements, AFM and XPS to show evidence for a successful surface modification.

4.3.2 Contact angle measurement.

Surface wettability can be determined by contact angle analysis. A water droplet is placed on the substrate under investigation and the angle between the surface and the tangent to the droplet defines the contact angle (see Figure 4.04). There are a variety of different contact angle techniques presently used: Wilhelmy-balance tensiometry, tilting-plate goniometry, and captive drop goniometry.[43] Although commonly two measurements involving the advancing and the receding angle are done to characterize wetting, a single measurement called the sessile drop contact angle method is sufficient for this study. The adhesive forces between the water droplet and the substrate govern the wettability. An unmodified, cleaned quartz surface commonly exhibits an angle near 0° displaying a high degree of wettability. On the other hand, an AUTS modified surface exhibits a larger contact angle that can exceed 90°.

Typical angles reported in the literature for closely packed alkanes that produce a highly hydrophobic surface are above 100°.[44, 45] Short-chained amine terminated compounds that exhibit a mixture of hydrophobic and hydrophilic surface characteristics show a contact angle between 50-60°.[34, 45] The measured

angle of 65 ± 1° obtained from our study of AUTS on quartz (Figure 4.04) is consistent with angles observed by Reinhoudt and coworkers that obtained a contact angle of 57 ± 2°.[46] Small changes in the measured angle can be due to variations in film packing and density. More importantly, the drastic change in contact angle from an unmodified substrate (10 ± 1°) to an AUTS modified substrate (65 ± 1°) indicates successful surface modification.

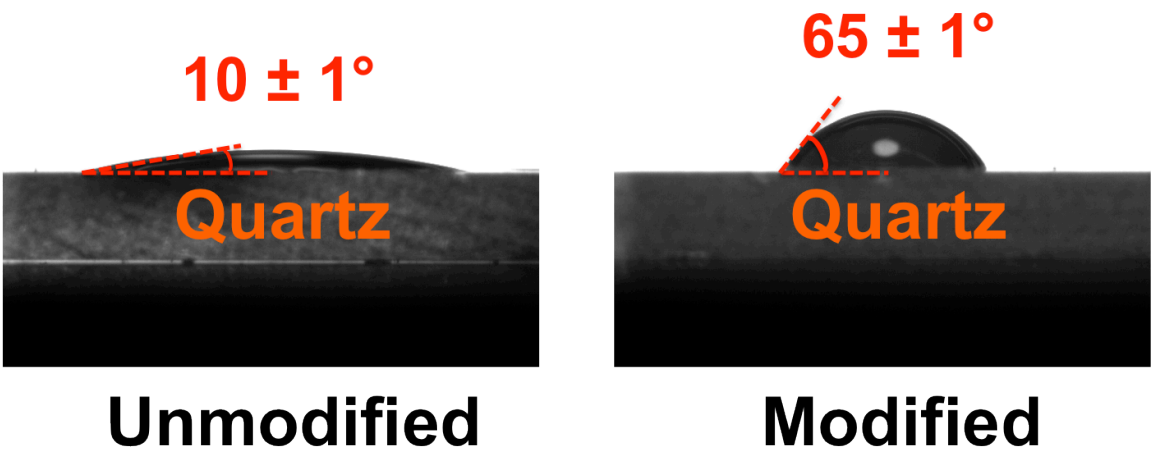

Figure 4.04. Sessile contact angle measurement for both unmodified and AUTS modified quartz substrates.

4.3.3 AFM measurement.

Additionally, the silane layer was probed with AFM and compared to an untreated quartz surface. The height images shown in Figure 4.05A and B indicate a change in the topography from the untreated quartz with a smooth surface (RMS roughness of 0.3 ± 0.1 nm) to the AUTS modified surface that exhibits twice the RMS roughness equal to 0.6 ± 0.1 nm. The latter shows regions of tall features dispersed over the imaged area. These features most likely represent localized regions of silane aggregation at the surface. Such aggregation has been mentioned in previous studies and aggregate prevention requires careful control of surface modification conditions.[30, 47] Despite aggregation occurring these height features are dispersed and at most 3-4 nm in height, corresponding to silane dimers or trimers. Overall the modified surface is uniform with a low roughness. The film thickness can be determined by a procedure first reported by Anariba *et al.* that involves the "scratching" of the film in contact mode AFM.[48]

Here a 1×1 μm area was scratched and re-imaged in tapping-mode (Figure 4.05C and D). Consequently, the height difference between the undisturbed and scratched areas shows the thickness of the silane film, as can be seen from the cross-sectional profile in Figure 4.05E. The measured height of 1.3 ± 0.3 nm is less than the reported monolayer height of 2.4 ± 0.2 nm measured by ellipsometry.[46] Our lower thickness measurement may be caused by molecular compression due to the AFM tip or molecular orientation on the surface that represents a more liquid-like film. However, based on the AFM results we are confident that the desired silane layer has formed on the quartz surface.

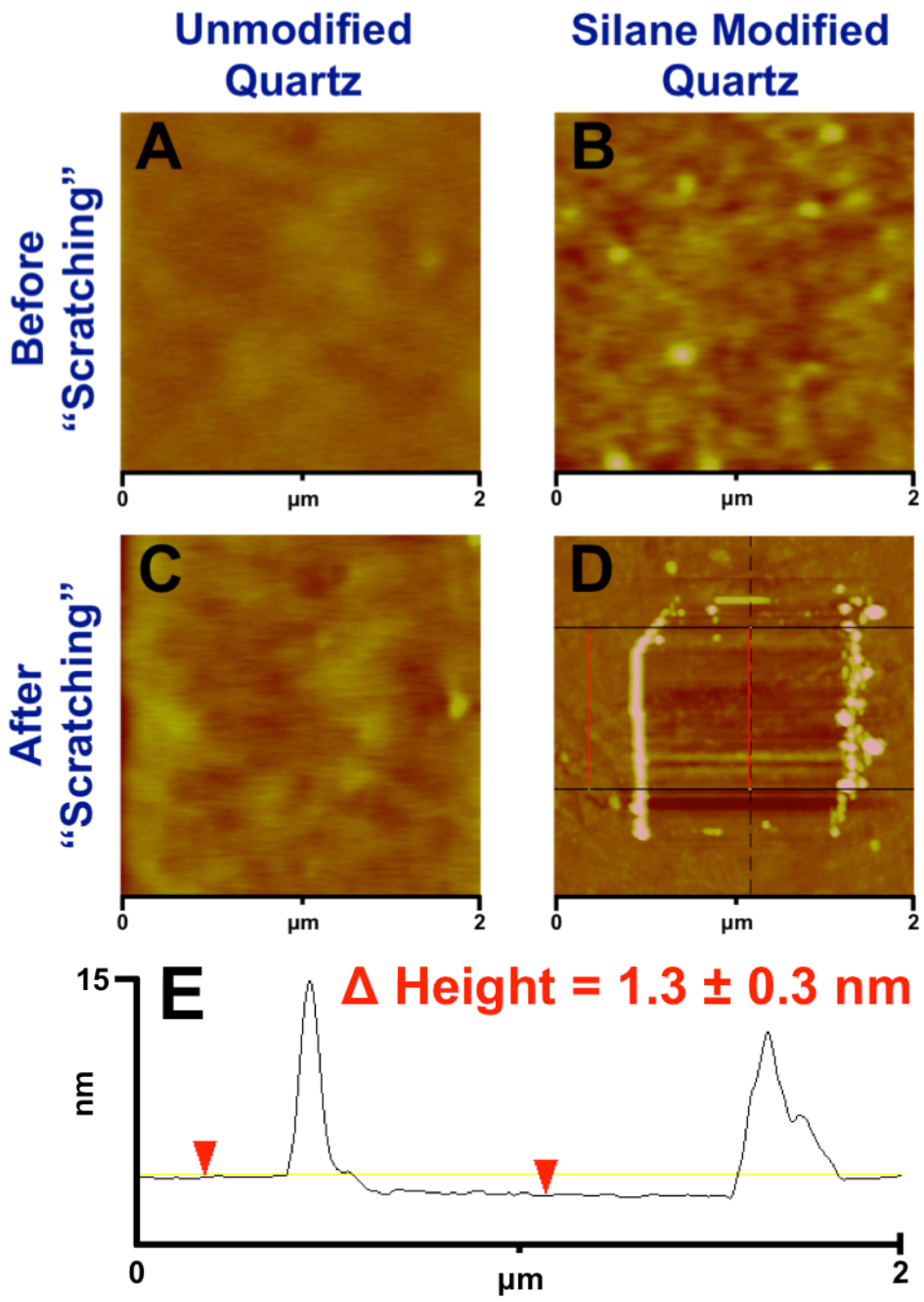

Figure 4.05. Tapping-mode AFM height images with 10 nm z-scale before scratching (A: unmodified quartz), (B: silane modified quartz) and after scratching a 1×1 µm area (C: unmodified quartz), (D: silane modified quartz). Section analysis of scratched area for silane modified quartz surface (E).

4.3.4 XPS analysis.

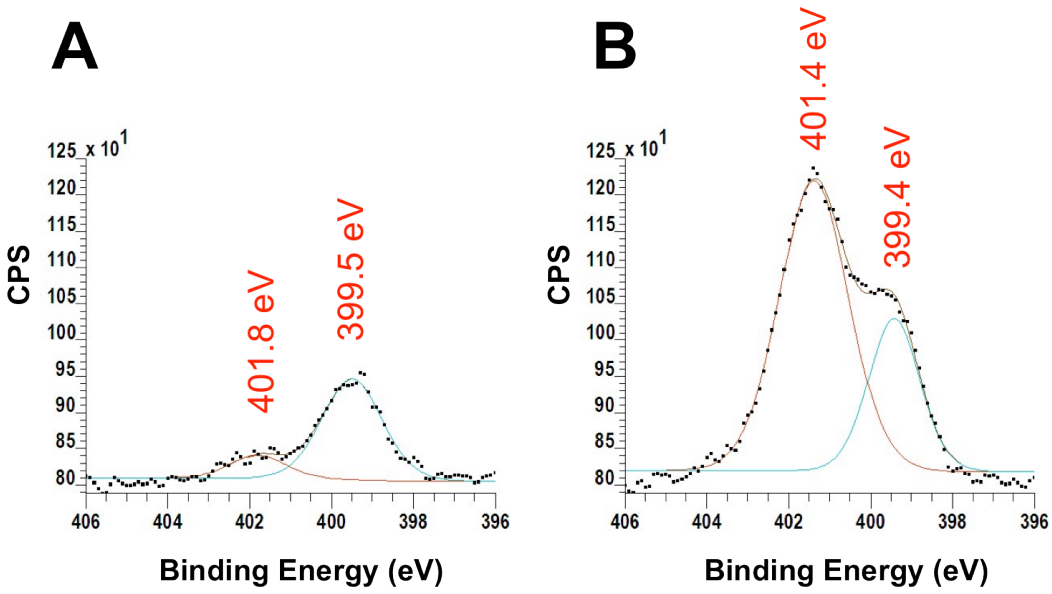

Figure 4.06. XPS high-resolution N1s spectra of an untreated quartz surface (A) and an AUTS modified quartz substrate (B).

Another surface sensitive method for silane film characterization is XPS, in which information on chemical bonding and elemental composition is provided.[47, 49-51] For this work we are mainly interested in determining that the AUTS layer has self-assembled on quartz and we will use the high-resolution nitrogen 1s spectrum for this purpose. Figure 4.06 clearly shows the difference in the N1s region between an untreated (A) and AUTS modified (B) substrate. Low intensity signals corresponding to nitrogen containing species are observed on the untreated quartz as shown in Figure 4.06A. We believe this is due to adsorbed impurities from sample handling and transport. The AUTS modified substrate exhibits strong nitrogen signals at 401.4 eV and 399.4 eV. These signals are significantly greater than those observed at the untreated quartz. The two peaks at

401.4 eV and 399.4 eV have been reported in the literature and were assigned to a protonated amino group and a free amine group respectively.[34] This assignment fits with the silane structure shown in Figure 4.03, as there is a secondary amine group within the molecule and a terminal amine group that can be easily protonated.

Table 4.1. XPS derived atomic concentrations (N, C and Si) for both an unmodified and silane modified quartz substrate.

XPS	Atomic Concentrations (%)		
	N1s	C1s	Si2p
Unmodified	0.560	17.4	26.1
Modified	2.40	24.2	23.4

Another piece of supporting evidence are the atomic compositions shown in Table 4.1. Relative to the unmodified quartz, the AUTS modified substrate exhibits a 5× higher N signal and a larger C signal, as we would expect from adding a carbon/nitrogen rich adlayer to the surface. Second, the silicon signal decreases for the modified substrate indicating the quartz surface has been covered and the silane film partially blocks the escaping electrons from the Si2p. In summary, all three techniques: contact angle, AFM and XPS provide evidence for the formation of a silane layer on quartz that is uniform and imparts an amine functionality to the surface that will be used in Sections 4.3.6 and 4.3.7 to capture gold and silver nanoparticles.

4.3.5 Solution UV-vis Spectroscopy of gold and silver nanoparticles

Initially, nanoparticle solutions were analyzed in the absence of a solid support, thus providing the simplest approach measuring the LSPR band intensity as a function of NP solution concentration. We selected 20 nm Ag and 40 nm Au nanoparticles on which to focus our study. The difference in size between silver and gold facilitates easy differentiation in SEM imaging. Figure 4.07A displays a representative extinction spectrum for the respective AgNPs and AuNPs in solution. This type of measurement was then extended to a mixture of two nanoparticle solutions with varying concentrations as shown by Figure 4.07B. For the mixtures the gold nanoparticle concentration was decreased from 75 pM to 5 pM while the silver nanoparticle concentration was increased and then kept constant in the upper two curves. The extinction magnitudes for both gold and silver were proportional to the solution concentration, as expected. This behavior is as predicted by the Beer-Lambert law (extinction $\propto$ concentration).

In order to monitor two LSPR bands simultaneously the bands have to be sufficiently resolved to accurately track nanoparticle concentrations by extinction magnitudes. The Rayleigh criterion can be used to determine if two bands are resolved by comparing the maxima of the two bands to the minimum between them.[52] Typically, the minimum has to be less than 80% of the maximum signal for the two bands to be considered resolved. In the case of Ag and Au in Figure 4.07B the bottom curve's minimum is approximately 50-60% in magnitude compared to the AgNP and AuNP LSPR bands, thus confirming the bands are well resolved.

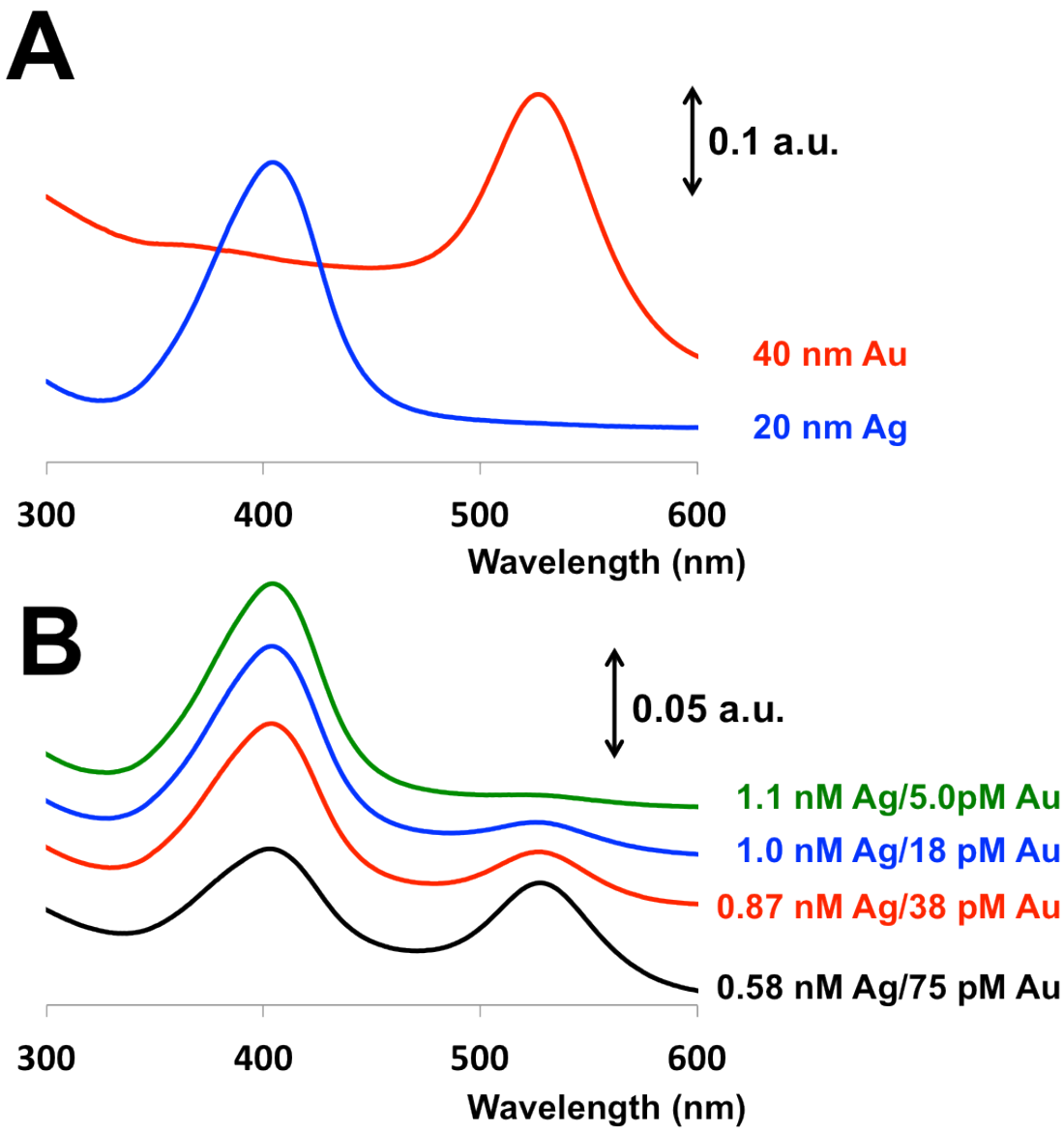

Figure 4.07. Individual solution UV-vis spectra are shown for 20 nm Ag and 40 nm gold nanoparticles in (A). UV-vis spectra of solution mixtures consisting of various concentration ratios of 20 nm Ag / 40 nm AU NPs are displayed in (B).

4.3.6 Transmission UV-vis of Au and Ag NPs adsorbed to modified quartz

We then extended the extinction measurements to immobilized nanoparticles on the modified transparent quartz substrates. The immobilization chemistry has been described earlier in section 4.3.1 and involves the use of amine-terminated silanes to modify the quartz surface. The amine functionality has a partial positive surface charge when exposed to a 7.4 pH nanoparticle solution and this surface charge facilitates electrostatic adsorption of the negatively charged NPs. For all our studies we mainly focused on 40 nm AuNPs, but we have also tested a variety of other sizes for comparison and validation. The effect of the adsorption time was investigated by collecting UV-vis spectra of adsorbed nanoparticles after specified intervals ranging from 1 h to 72 h. The plot in Figure 4.08A indicates that NP adsorption plateaus after 24 h. Similar results have also been established for 100 nm AuNPs and 40 nm AgNPs (not shown here). All consequent adsorption studies were carried out with a 24 h adsorption time to reach equilibrium coverage. The effect of solution concentration was investigated and the results are shown in Figure 4.08B and C. As the solution concentration was raised from 15 pM to 150 pM the extinction magnitude increased 30 fold. A plot of extinction vs. [solution] is linear ($R^2 = 0.9946$) in the range analyzed, which covered one order of magnitude. The lowest solution concentration studied, 15 pM, corresponds to the limit of detection (LOD) as this concentration produces an extinction magnitude that is approximately 3x the noise. We note that while the LOD for the NPs in solution is of general analytical interest, this figure of merit is irrelevant to our proposed application as modified

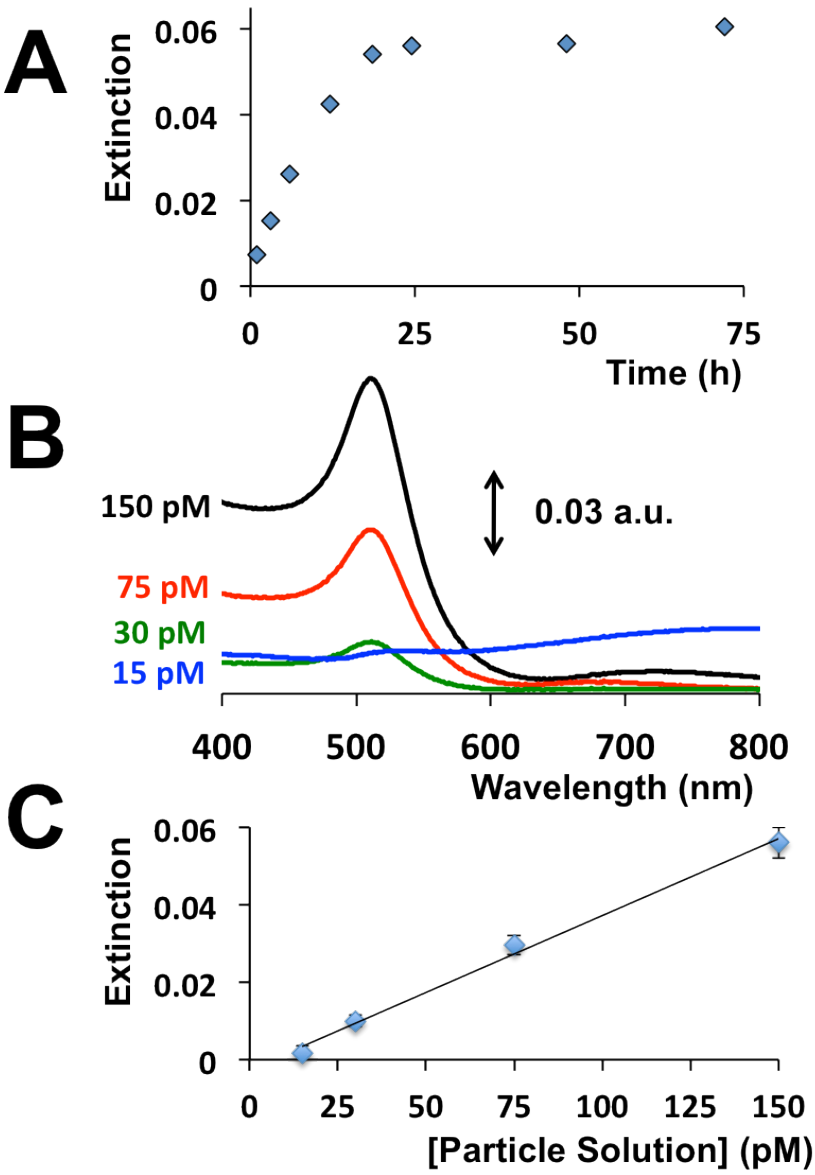

Figure 4.08. Adsorption of 40 nm gold nanoparticles on AUTS terminated quartz as a function of incubation time (A) and as a function of solution concentration (B). Part (C) shows a graph of the extinction magnitude of the LSPR bands from the UV-vis spectra in (B) versus solution concentration. The y-error bars in (C) represent the standard deviation for n=3 measurements. The line through the markers is the linear least square fit and yielded y = 0.000397x -0.00250 and a R^2 value of 0.9946.

NPs will be used as labels and will be present in solution concentrations much higher than 15 pM. It appears that a saturation coverage was not reached for the concentrations studied, but the range was sufficient to demonstrate effective adsorption and quantitative monitoring by UV-vis spectroscopy.

Hitherto we have considered the extinction response as a function of nanoparticle solution concentration; however, in our bioassay design a more appropriate measure is the nanoparticle density at the surface of the substrate. During a bioassay the analyte concentration is varied, but the nanoparticle solution concentration used to label the analyte is kept constant. Therefore the nanoparticle density on the surface is directly proportional to the number of analytes present. Scanning electron microscopy (SEM) was used to examine the relationship between extinction magnitude and NP surface density. The same substrates analyzed by UV-vis were coated with a thin film of chromium to prevent charging and imaged with SEM as shown in Figure 4.09A-D. Each image was analyzed by counting the number of NPs present and calculating a corresponding particle density (particles/μm^2). This value was then used to construct the calibration plot of extinction vs. particle density shown in Figure 4.09E. Again, we observe a linear relationship ($R^2 = 0.9970$) for the chosen range. The LOD that was mentioned previously as a solution concentration of 15 pM for 40 nm AuNPs corresponds to approximately 10 particles / μm^2. The total number of adsorbed NPs detected can be determined by considering the spot size of the

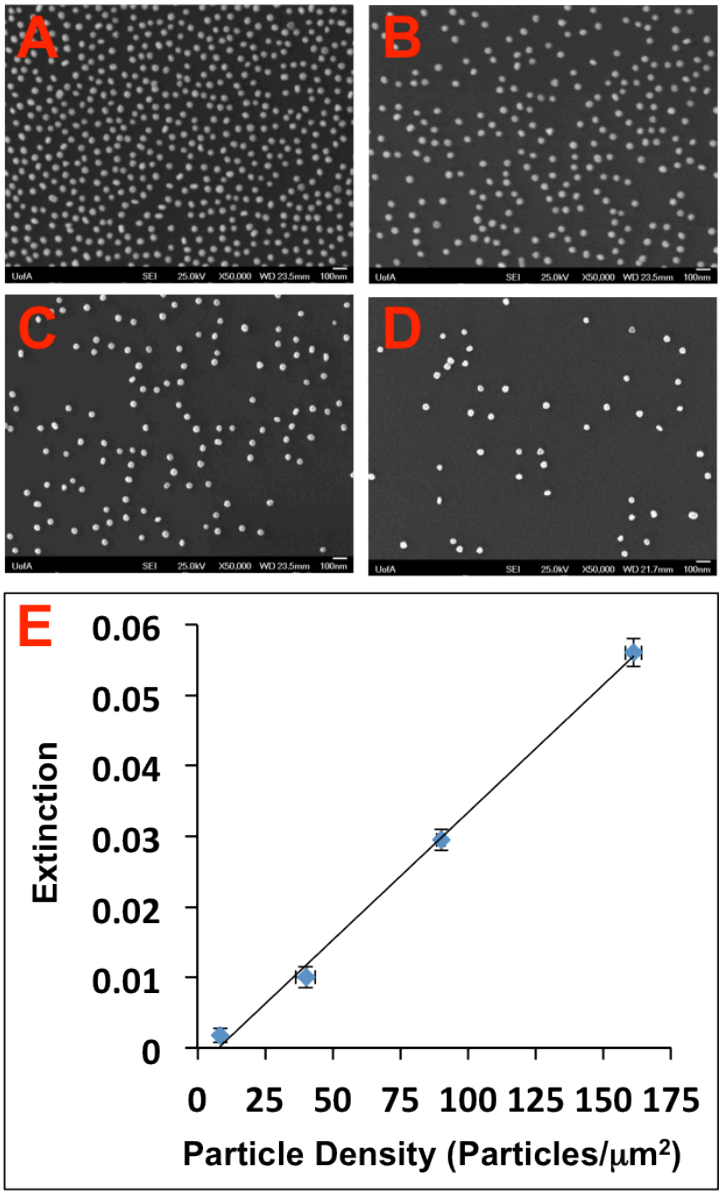

Figure 4.09. SEM imaging of adsorbed 40 nm AuNPs on quartz from four different solution concentrations: (A) 150 pM, (B) 75 pM, (C) 30 pM, and (D) 15 pM. Extinction magnitudes from UV-vis measurements of the substrates shown in A-D are plotted versus particle density in (E) with a linear least square fit with $y = 0.000362x - 0.00283$ and $R^2 = 0.9970$. The x- and y-error bars represent the standard deviation for n=3 measurements.

visible light beam. The light beam dimensions for the instrument used is 1 × 8 mm. Thus, we can detect about 8.0×10^7 nanoparticles in the light path. We note that this is a relatively large number of adsorbed NPs and does not approach single NP detection. However, in our intended application, the density of NPs will be governed by the number of analyte species captured by the assay, which, in turn depends on the binding strength between the immobilized capture agent and analyte.

Equation 4-03 shows that factors such as NP size and material significantly influence extinction and these factors are examined below. Following the same procedure as above we constructed extinction-particle density plots for AuNPs of various sizes as shown in Figure 4.10A. The differing ranges in particle density observed are due to the solution concentrations used for adsorption, which are typically higher for smaller NP sizes. The main feature of the plot in Figure 4.10A is the larger response for bigger nanoparticles. For example at a particle density of 8 particles / μm^2, the response is 30 fold higher for 100 nm compared to 40 nm AuNPs. This is also portrayed by the slopes of the curves for the various sizes, which are related to σ_{ext}. Extinction cross section values are available from the literature[21, 53] or can be calculated experimentally by equation 4-04. We would expect the slope of the plots in Figure 4.10A to be directly proportional to the extinction cross section and indeed Figure 4.10B shows a linear relationship. The effect of NP size on extinction is not surprising based on Mie theory and this has also been demonstrated computationally by El-

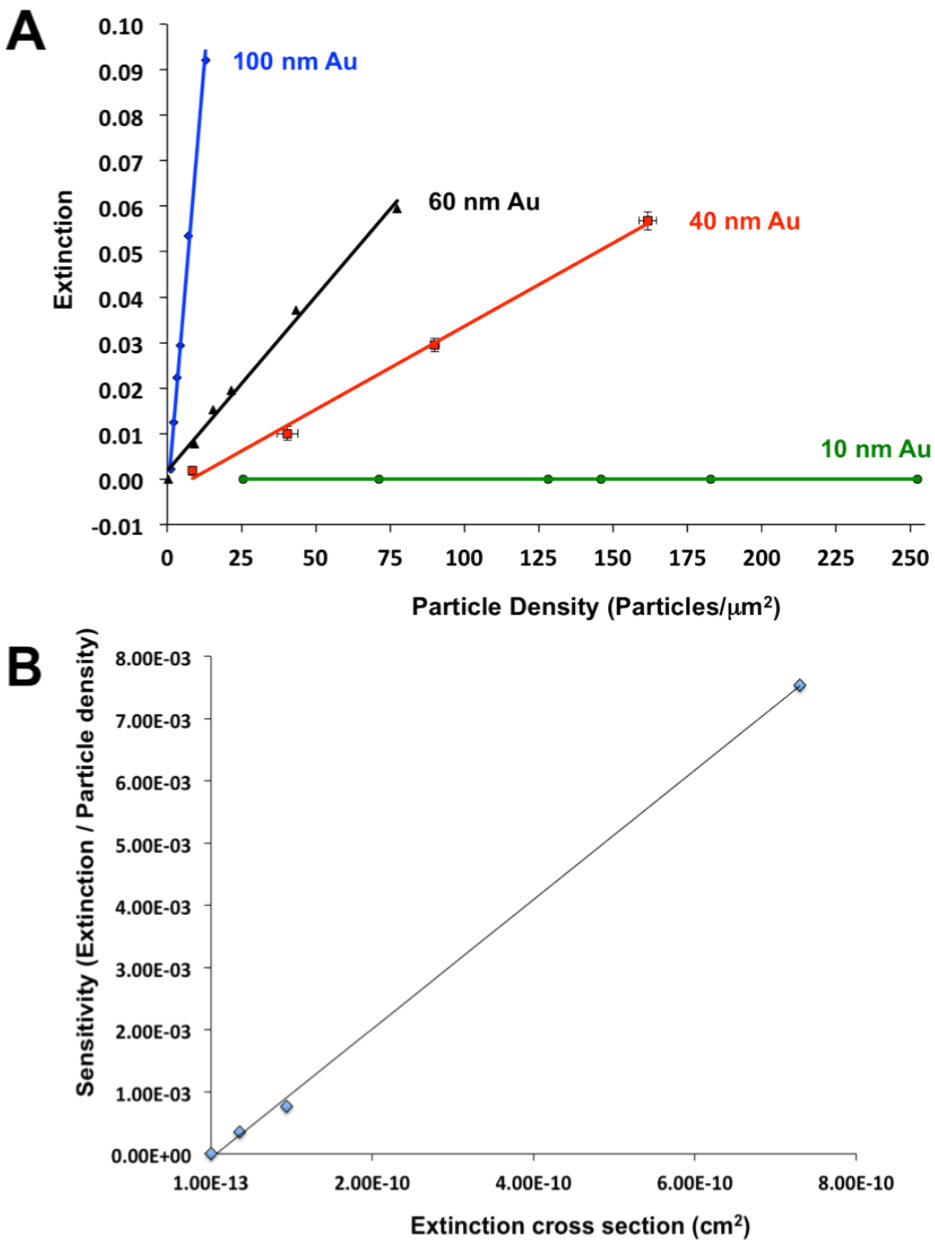

Figure 4.10. Plots of LSPR band extinction magnitudes versus particle density of adsorbed nanoparticles on a transparent substrate for a variety of AuNPs sizes are shown in (A). The slope for each line fit in (A) is graphed as a function of the corresponding extinction cross section for that AuNP size (B). The linear least square fit for (B) yielded $y = 1.04\times10^{7}x - 6.86\times10^{-5}$ and a R^2 value of 0.9993.

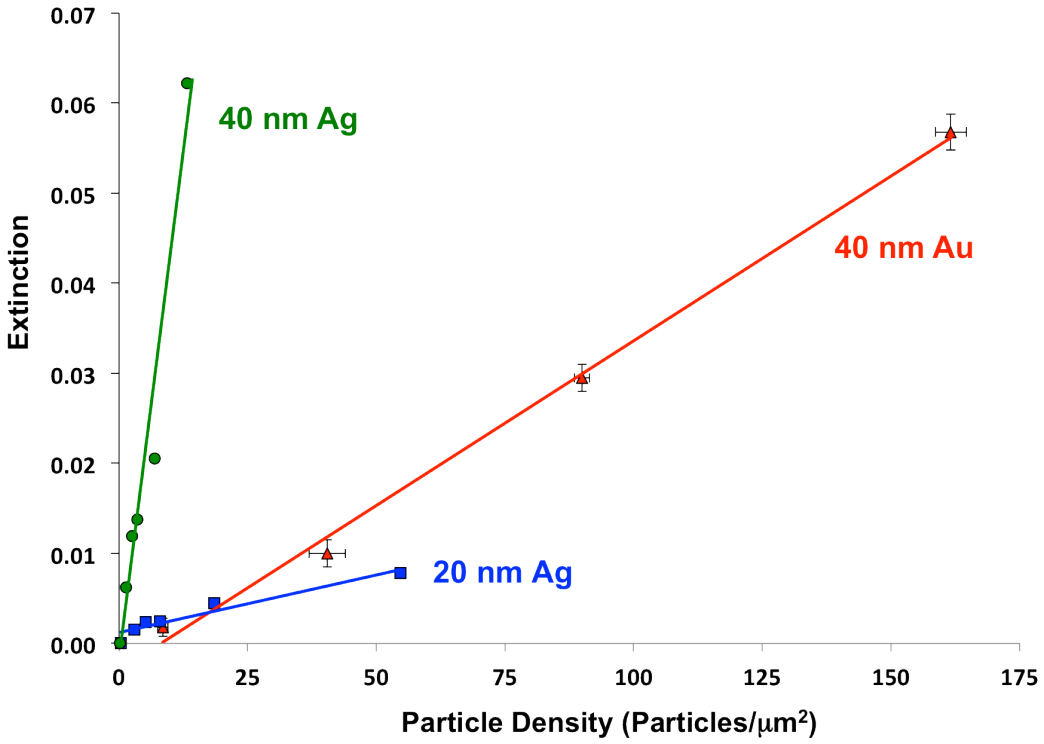

Figure 4.11. Plots of LSPR band extinction magnitudes versus particle density of adsorbed nanoparticles on a transparent substrate for silver (20 and 40 nm) and gold (40 nm) nanoparticles. The x- and y-error bars for 40 nm Au represent standard deviation for n=3 measurements.

Sayed and co-workers.[19] However, to the best of our knowledge this effect has not been studied experimentally for adsorbed NPs on modified quartz and NP size-selection will be an important criterion for future bioassay applications. The LOD is affected by the choice of nanoparticle size, which is defined by the minimum detectable signal that is 3× the noise. For 40 nm AuNPs the minimum particle density that can be detected is about 10 particles / μm^2 whereas for 100 nm AuNPs the detection limit is improved by an order of magnitude to 1 particle / μm^2.

Another feature that affects the response is the NP material and thus we have investigated both gold and silver nanoparticles. A comparison between 40 nm AuNPs and two sizes of AgNPs is shown in Figure 4.11. Again, as the silver particle diameter is increased the slope (extinction/particle density) increases as well and is directly proportional to the extinction cross section. Comparing the same size (40 nm) for both silver and gold, the resulting response differs greatly. The calculated σ_{ext} for 40 nm AgNPs is 1.44×10^{-10} cm^2 and is an order of magnitude greater than the σ_{ext} of 40 nm AuNPs (2.01×10^{-11} cm^2). The difference between gold and silver is explained by differences in the real and imaginary components of the dielectric function (ε_1 *and* ε_2) that affect the overall extinction cross section as indicated by equation 4-03 in Section 4.1.

In the design of a multiplexed bioassay the extinction cross section values will be important and choosing two different labels with near equivalent σ_{ext} will be beneficial as extinction read-outs can then be directly compared as would be the case for 20 nm AgNPs ($\sigma_{ext} = 1.26\times10^{-11}$ cm^2) and 40 nm AuNPs. Furthermore, other factors which need to be considered for future bioassay applications are discussed in Chapter 5 and 6, including NP surface modification with biomolecules and NP stability. Larger nanoparticle suspensions typically settle very quickly and this can lead to agglomeration and non-uniform adsorption on planar surfaces. For much smaller particles the response is significantly reduced due to the smaller extinction cross section. Lastly, the modification of AuNPs in solution with biomolecules is well-studied,[4] whereas the modification

of AgNPs and the resulting stability has to be evaluated before attempting to detect two labels in a bioassay simultaneously.

4.3.7 Transmission UV-vis of mixtures of Au and Ag NPs adsorbed to quartz

The final step in the work described in this Chapter was to demonstrate the capability of detecting two different metallic nanoparticles (AuNPs and AgNPs) adsorbed on the same quartz substrate. The advantages of multiplexing were discussed in Chapter 1, but in short these NPs can serve as labels in bioassays and it is desirable to detect more than one analyte simultaneously. A mixture of gold and silver nanoparticles was examined to provide the best possible band resolution. Two different NP combinations were studied by measuring the extinction of various solution concentration mixtures adsorbed on AUTS modified quartz. Figure 4.12A shows the results of the first mixture studied (20 nm AgNPs and 40 nm AuNPs). In the UV-vis spectrum the LSPR bands are well resolved with approximately 150 nm difference in λ_{max} and the minimum between the two bands is less than 80% of the two LSPR band maxima meeting the Rayleigh criterion as discussed in Section 4.3.5. The four curves plotted in (A) follow the expected trend in terms of extinction values as function of solution concentration as observed in Section 4.3.6. As the silver nanoparticle concentration is increased the extinction magnitude increases and vice versa. The same trend also holds true for the gold nanoparticles in the mixture. There is, however, a noticeable difference in the overall extinction magnitudes for adsorbed NPs in a mixture and in the absence of the other NP, which is highlighted by Figure 4.12B for 40 nm

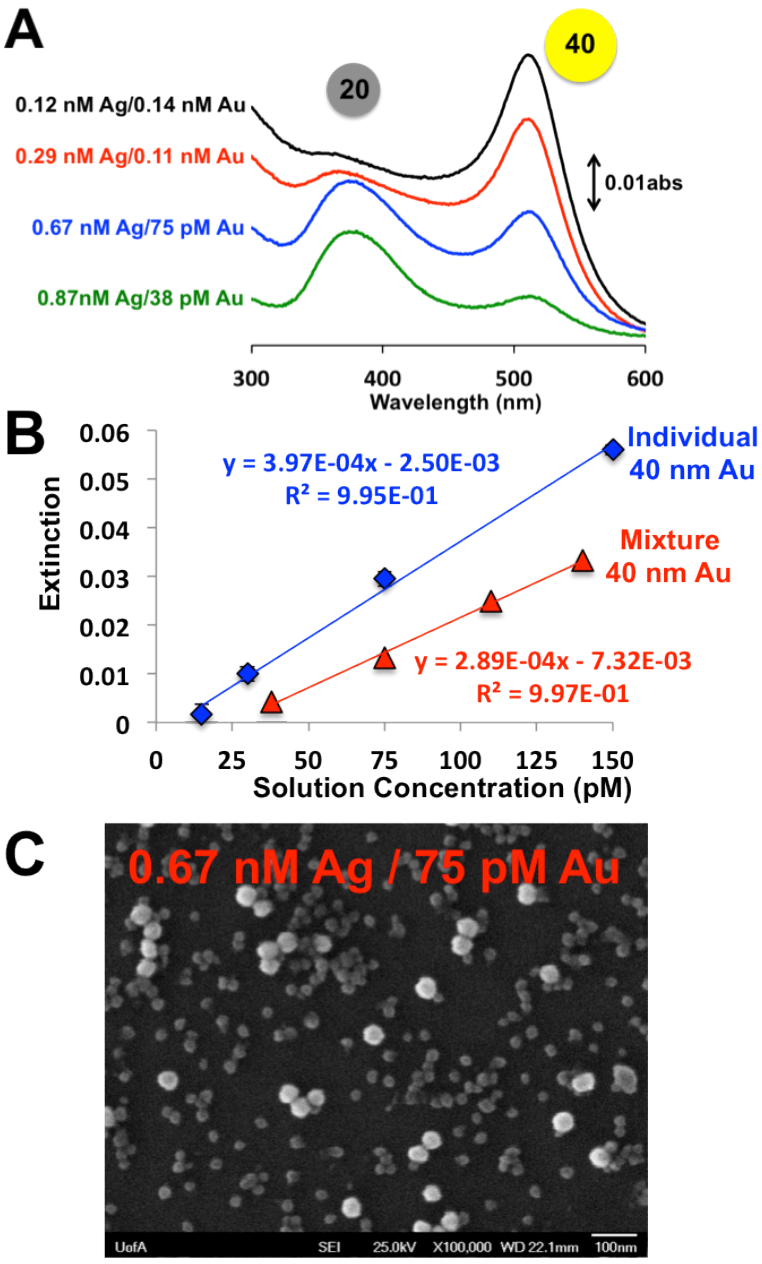

Figure 4.12. UV-vis spectra for various solution mixtures of 20 nm AgNPs and 40 nm AuNPs adsorbed on AUTS modified quartz (A). The 40 nm AuNP extinction response from (A) is plotted in (B) along side the response from Figure 4.08C. Part (C) shows a representative SEM image for an incubation mixture of 0.67 nM Ag (20 nm) and 75 pM Au (40 nm) nanoparticles.

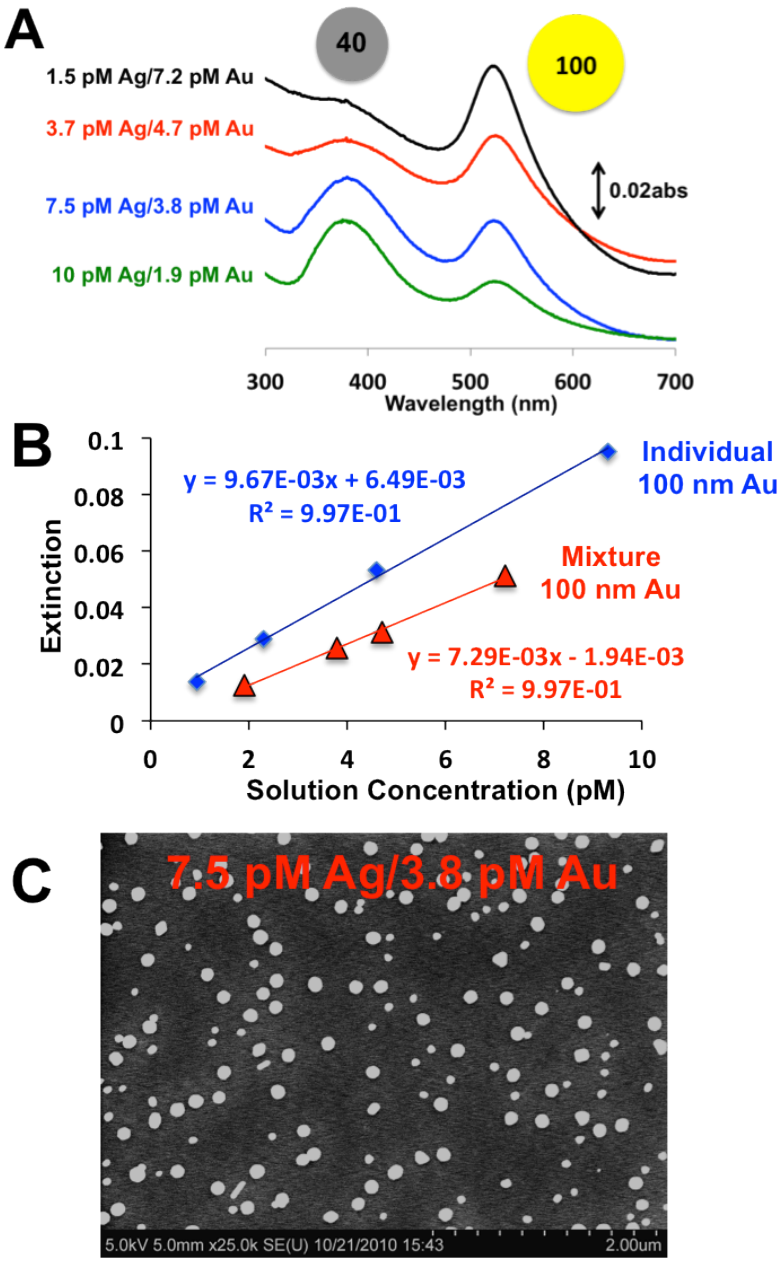

Figure 4.13. UV-vis spectra for various solution mixtures of 40 nm AgNPs and 100 nm AuNPs adsorbed on AUTS modified quartz (A). The 100 nm AuNP extinction response from (A) is plotted in (B) along side the response without AgNPs present. Part (C) shows a representative SEM image for an incubation mixture of 7.5 pM Ag (40nm) and 3.8 pM Au (100 nm) nanoparticles.

AuNPs. The two responses are offset as indicated by the different y-intercept (-2.50×10^{-3} vs. -7.32×10^{-3}), but the slopes remained fairly constant. This offset or decrease in overall extinction is most likely due to a reduced particle density at the quartz surface resulting from competitive adsorption, i.e. AgNPs occupying adsorption sites. This result is not surprising and has been reproduced for another mixture consisting of 100 nm AuNPs and 40 nm AgNPs shown in Figure 4.13A and B. Also here the two LSPR bands are baseline resolved and the extinction magnitude is proportional to the solution concentration. Figure 4.13B displays a similar slope behavior and offset in extinction from 100 nm gold nanoparticles for a mixture and for Au particles alone. The competition between two different labels will potentially affect the detection limit in a multiplexed bioassay design as the particle density of one label on the biochip is decreased resulting in a lower absorption for a similar analyte concentration. For both mixtures a representative SEM image is shown in Figure 4.12C and Figure 4.13C. The SEM images clearly confirm the presence of the respective nanoparticle sizes on the substrate and show a uniform distribution of the two sizes with minimal aggregation.

4.4 CONCLUSION

In this chapter the adsorption of gold and silver nanoparticles on modified quartz was investigated, monitored with UV-vis spectroscopy and verified with scanning electron microscopy. This study has shown that a common benchtop UV-vis spectrophotometer is capable of successfully quantitating the particle density at the quartz surface by measuring the LSPR band intensity. The band intensity is influenced by the extinction cross section, which increases with nanoparticle diameter. Based on this characteristic a series of gold NP sizes was studied and it was determined that the detection limit can be improved from 10 particles / μm^2 for 40 nm nanoparticles to 1 particle / μm^2 for 100 nm NPs. Another feature that can be exploited is NP material: silver nanoparticles exhibit a LSPR band that is significantly blue-shifted and as a result allows for the quantitation of both AuNPs and AgNPs adsorbed to a solid support simultaneously. This lays the foundation for applications in biosensing where nanoparticles serve as labels and provides the capability for multiplexing by utilizing NPs composed of different materials.

4.5 REFERENCES

1. Anker, J. N.; Hall, W. P.; Lyandres, O.; Shah, N. C.; Zhao, J.; Van Duyne, R. P. *Nat. Mater.* **2008,** 7, (6), 442-453.
2. Saha, K.; Agasti, S. S.; Kim, C.; Li, X.; Rotello, V. M. *Chem. Rev.* **2012,** 10.1021/cr2001178.
3. Zamborini, F. P.; Bao, L.; Dasari, R. *Anal. Chem.* **2011,** 84, (2), 541-576.
4. Grubisha, D. S.; Lipert, R. J.; Park, H. Y.; Driskell, J.; Porter, M. D. *Anal. Chem.* **2003,** 75, (21), 5936-5943.
5. Ambrosi, A.; Airo, F.; Merkoci, A. *Anal. Chem.* **2010,** 82, (3), 1151-1156.
6. Olofsson, L.; Rindzevicius, T.; Pfeiffer, I.; Kall, M.; Hook, F. *Langmuir* **2003,** 19, (24), 10414-10419.
7. Zhang, L. D.; Fang, M. *Nano Today* **2010,** 5, (2), 128-142.
8. Gifford, L. K.; Sendroiu, I. E.; Corn, R. M.; Luptak, A. *J. Am. Chem. Soc.* **2010,** 132, (27), 9265-9267.
9. Kim, S.; Lee, J.; Lee, S. J.; Lee, H. J. *Talanta* **2010,** 81, (4-5), 1755-1759.
10. Sim, H. R.; Wark, A. W.; Lee, H. J. *Analyst* **2010,** 135, (10), 2528-2532.
11. Luan, Q. F.; Zhou, K. B.; Tan, H. N.; Yang, D.; Yao, X. *Biosens. Bioelectron.* **2011,** 26, (5), 2473-2477.
12. Sendroiu, I. E.; Gifford, L. K.; Luptak, A.; Corn, R. M. *J. Am. Chem. Soc.* **2011,** 133, (12), 4271-4273.
13. Nath, N.; Chilkoti, A. *Anal. Chem.* **2004,** 76, (18), 5370-5378.

14. Hall, W. P.; Ngatia, S. N.; Van Duyne, R. P. *J. Phys. Chem. C* **2011,** 115, (5), 1410-1414.

15. Mie, G. *Ann. Phys.* **1908,** 25, (3), 377-445.

16. Kreibig, U.; Vollmer, M., *Optical properties of metal clusters*. Springer: Berlin ; New York, 1995; p xx, 532 p.

17. Lopatynskyi, A. M.; Lopatynska, O. G.; Guo, L. J.; Chegel, V. I. *IEEE Sens. J.* **2011,** 11, (2), 361-369.

18. Kelly, K. L.; Coronado, E.; Zhao, L. L.; Schatz, G. C. *J. Phys. Chem. B* **2003,** 107, (3), 668-677.

19. Jain, P. K.; Lee, K. S.; El-Sayed, I. H.; El-Sayed, M. A. *J. Phys. Chem. B* **2006,** 110, (14), 7238-7248.

20. Johnson, P. B.; Christy, R. W. *Phys. Rev. B* **1972,** 6, (12), 4370-4379.

21. Evanoff, D. D.; Chumanov, G. *J. Phys. Chem. B* **2004,** 108, (37), 13957-13962.

22. Grabar, K. C.; Freeman, R. G.; Hommer, M. B.; Natan, M. J. *Anal. Chem.* **1995,** 67, (4), 735-743.

23. Enders, D.; Nagao, T.; Nakayama, T.; Aono, M. *Langmuir* **2007,** 23, (11), 6119-6125.

24. Kim, K.; Ryoo, H.; Shin, K. S. *Langmuir* **2010,** 26, (13), 10827-10832.

25. Mayya, K. M.; Gole, A.; Jain, N.; Phadtare, S.; Langevin, D.; Sastry, M. *Langmuir* **2003,** 19, (22), 9147-9154.

26. Schmitt, J.; Machtle, P.; Eck, D.; Mohwald, H.; Helm, C. A. *Langmuir* **1999,** 15, (9), 3256-3266.

27. Keating, C. D.; Musick, M. D.; Keefe, M. H.; Natan, M. J. *J. Chem. Educ.* **1999,** 76, (7), 949-955.

28. Chen, Y. Q.; Lu, C. J. *Sens. Actuators, B* **2009,** 135, (2), 492-498.

29. Flavel, B. S.; Nussio, M. R.; Quinton, J. S.; Shapter, J. G. *J. Nanopart. Res.* **2009,** 11, (8), 2013-2022.

30. Ulman, A. *Chem. Rev.* **1996,** 96, (4), 1533-1554.

31. Mathauer, K.; Frank, C. W. *Langmuir* **1993,** 9, (12), 3446-3451.

32. Mathauer, K.; Frank, C. W. *Langmuir* **1993,** 9, (11), 3002-3008.

33. Lee, I.; Wool, R. P. *Thin Solid Films* **2000,** 379, (1-2), 94-100.

34. Kowalczyk, D.; Slomkowski, S.; Chehimi, M. M.; Delamar, M. *Int. J. Adhes. Adhes.* **1996,** 16, (4), 227-232.

35. Nakayama, H.; Nakanishi, J.; Shimizu, T.; Yoshino, Y.; Iwai, H.; Kaneko, S.; Horiike, Y.; Yamaguchi, K. *Colloids Surf., B* **2010,** 76, (1), 88-97.

36. Wasserman, S. R.; Tao, Y. T.; Whitesides, G. M. *Langmuir* **1989,** 5, (4), 1074-1087.

37. Krasnoslobodtsev, A. V.; Smirnov, S. N. *Langmuir* **2002,** 18, (8), 3181-3184.

38. Sagiv, J. *J. Am. Chem. Soc.* **1980,** 102, (1), 92-98.

39. Chaudhury, M. K.; Whitesides, G. M. *Science* **1992,** 256, (5063), 1539-1541.

40. Zhang, F.; Sautter, K.; Larsen, A. M.; Findley, D. A.; Davis, R. C.; Samha, H.; Linford, M. R. *Langmuir* **2010,** 26, (18), 14648-14654.

41. Fiorilli, S.; Rivolo, P.; Descrovi, E.; Ricciardi, C.; Pasquardini, L.; Lunelli, L.; Vanzetti, L.; Pederzolli, C.; Onida, B.; Garrone, E. *J. Colloid Interface Sci.* **2008,** 321, (1), 235-241.

42. Asenath-Smith, E.; Chen, W. *Langmuir* **2008,** 24, (21), 12405-12409.

43. Krishnan, A.; Liu, Y. H.; Cha, P.; Woodward, R.; Allara, D.; Vogler, E. A.; Grp, H. B. I. R. *Colloids Surf., B* **2005,** 43, (2), 95-98.

44. Jo, S.; Park, K. *Biomater.* **2000,** 21, (6), 605-616.

45. Araujo, Y. C.; Toledo, P. G.; Leon, V.; Gonzalez, H. Y. *J. Colloid Interface Sci.* **1995,** 176, (2), 485-490.

46. Rozkiewicz, D. I.; Kraan, Y.; Werten, M. W. T.; de Wolf, F. A.; Subramaniam, V.; Ravoo, B. J.; Reinhoudt, D. N. *Chem. Eur. J.* **2006,** 12, (24), 6290-6297.

47. Niehoff, P.; Ebbinghaus, P.; Keil, P.; Erbe, A. *Appl. Surf. Sci.* **2012,** 258, (7), 3191-3196.

48. Anariba, F.; DuVall, S. H.; McCreery, R. L. *Anal. Chem.* **2003,** 75, (15), 3837-3844.

49. Turner, N. H.; Schreifels, J. A. *Anal. Chem.* **1994,** 66, (12), R163-R185.

50. Libertino, S.; Giannazzo, F.; Aiello, V.; Scandurra, A.; Sinatra, F.; Renis, M.; Fichera, M. *Langmuir* **2008,** 24, (5), 1965-1972.

51. Heise, A.; Stamm, M.; Rauscher, M.; Duschner, H.; Menzel, H. *Thin Solid Films* **1998,** 327, 199-203.

52. Owen, T., Fundamentals of modern UV-visible spectroscopy, Primer. *Agilent Technologies* 2000.

53. Technical Information on Gold Conjugates. 2010. Ted Pella, Inc. . http://www.tedpella.com/gold_html/gold-tec.htm (1/4/2012),

Chapter 5:

Nanoparticle Labels in Biosensing: UV-vis Detection Based on Localized Surface Plasmon Resonance

5.1 INTRODUCTION

The work presented here is a combination of several studies and will tie the previous projects together in one final chapter that is geared towards biosensing. In Chapter 2 and 3 the modification of gold nanoparticles using diazonium salt and thiol chemistry was discussed. Here, the use of this chemistry to modify both nano and planar substrates is described. Further, in Chapter 4 it was demonstrated that the nanoparticle density on a transparent substrate could be successfully determined with a simple transmission measurement. Both aspects combined will be utilized to introduce a sandwich immunoassay design that detects and quantitates binding with the help of extrinsic nanoparticle (NP) labels.

Many advances in the detection of biomolecules involve the use of nanotechnology. At the forefront of such advances are gold nanoparticles (AuNPs) and many reviews are dedicated to applications of these nanospheres ranging from signal enhancements in established procedures to new forms of labeling *in vitro* and *in vivo*. [1-7] These AuNPs have unique properties that can be harnessed in the design of a biosensor such as a phenomenon called localized surface plasmon resonance (LSPR). As described in the previous chapters this phenomenon refers to a strong absorption band in the visible spectrum due to the collective excitation of conduction electrons in the metal nanospheres. Chapter 1

describes several research areas that utilize the sensitivity of the LSPR band towards changes in the refractive index of the nanoparticle surface and the surrounding medium. A monolayer of immobilized gold nanoparticles can serve as a sensing platform to detect biomolecule binding by monitoring the extent of the λ_{max} shift.[8-11] However, this type of assay does not allow for the detection of multiple analytes simultaneously and the instrumentation has to be more sophisticated when detecting small shifts. Chapter 1 describes a different approach that uses a sandwich immunoassay with gold nanoparticles as extrinsic labels, employing the capability of AuNPs to enhance Raman signals.[12] These labels can be modified with various biomolecules and carry unique Raman reporter molecules that can be detected in a SERS based assay providing the capability for multiplexing.[13]

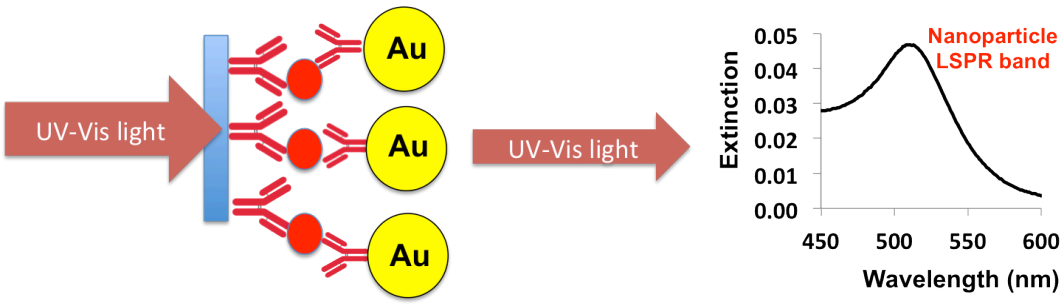

Figure 5.01. Schematic overview of sandwich immunoassay described in this chapter. An UV-vis detection method is employed that measures the intensity of the NP LSPR band and relates this to the nanoparticle density on the biochip, which in turn can be related to the analyte concentration.

A combination of those two concepts (LSPR sensing and SERS sandwich immunoassay) led to the proposed bioassay design presented in Figure 5.01. The sandwich immunoassay detection strategy relies on the detection of the LSPR band by extinction spectroscopy with a UV-vis spectrophotometer. The magnitude of the LSPR extinction band can be used quantitatively to assess the number of NPs present at the biochip surface, which in turn indicates information about the number of analytes captured. The advantages of such a design are two-fold: A simple, readily available detection using a benchtop UV-vis spectrophotometer and the capability of multiplexing by employing different nanoparticle labels (i.e. gold and silver NPs). In addition, a peak height measurement in UV-vis spectroscopy is more intuitive than a peak shift measurement. The latter requires knowledge of the LSPR band before exposure to analyte and small variations in buffer composition can influence the results. The peak height on the other hand is a straightforward measurement that is less prone to interferences and it intuitively scales with the number of labels bound.

In order to utilize a standard benchtop spectrophotometer the biochip design requires a transparent surface such as glass or quartz. As discussed in the previous chapter, silane chemistry is usually preferred when modifying these surfaces.[14, 15] Nevertheless, silane films that are typically used to bind biomolecules can be prone to instability when exposed to aqueous conditions for extended periods resulting in hydrolysis of the siloxane bond. This hydrolysis is catalyzed by the amine functionality.[16] This potentially presents a problem when attaching/capturing proteins at the surface, as all steps typically require immersion

in aqueous buffer solutions. The possibility to employ other surface modification chemistries is limited by the requirement for transparent substrates. One option is the use of transparent ultrathin metal films. A significant amount of research has focused on the manufacturing of optically transparent conductive films for various applications ranging from photodetectors[17, 18] to studying adsorbing electroactive molecules.[19, 20] Whitesides and co-workers have used thin silver and gold films for mircocontact printing of cells on glass.[21] Other researchers have utilized these transparent gold films to study thiol SAMs,[22] and as an anodes in organic light-emitting diodes.[23] Another method involves a transparent carbon film created by spin-coating a thin layer of photo resist and pyrolyzing it at high temperatures resulting in a robust and conductive film.[20, 24, 25] Carbon surfaces can be modified by the electrochemical grafting of aryl diazonium salts producing covalently linked multilayers.[26-29] Chapters 2 and 3 are dedicated to diazonium salt chemistry, and further, these layers have shown excellent stability on planar substrates.[29-31] The ultrathin carbon films provided a possible solution, but in the manufacturing of these substrates it is difficult to reproducibly produce films of the exact same thickness. This can lead to variations in the optical transparency of these substrates, which potentially could affect the bioassay readouts. Mahmoud *et al.* have presented an alternative approach utilizing an e-beam evaporated 5 nm thin titanium film, which rapidly oxidizes and becomes increasingly transparent.[31] The films exhibited a low optical absorption background. Titanium provides the necessary reducing potentials to drive the spontaneous reduction of aryl diazonium salts to completion, typically within minutes forming a multilayered

film. Stability studies conducted by Mahmoud *et al.* have shown remarkable robustness with only a 12% film-reduction during adverse conditions including heating to 200°C.[31] Combined, the reproducible film formation through e-beam evaporation, ease of modification, adlayer stability, and low optical background made Ti coated quartz ideal for use as a substrate in our biosensing platform.

This Chapter describes the design and evaluation of the performance of a sandwich immunoassay, which relies on modified gold nanoparticle (AuNP) labels for detection. This chapter is divided into two main parts: surface modification and biosensing. First, the surface chemistry of the planar substrate and the nanoparticles will be described and evaluated with UV-vis spectroscopy, atomic force microscopy (AFM) and infrared reflection absorption spectroscopy (IRRAS). Second, the sandwich immunoassay performance was assessed by UV-vis spectroscopy and scanning electron microscopy (SEM). This will show the effectiveness of using diazonium-derived layers in biosensing, and furthermore, show the successful implementation of gold nanoparticles as functionalized labels in the detection of biomolecules with a simple and readily available UV-vis detection. Lastly, detection limits and dynamic range will be compared to other established techniques such as surface plasmon resonance (SPR) to evaluate the competitiveness of this assay.

5.2 EXPERIMENTAL

Reagents and Materials. Sulphuric acid, 96%, and hydrogen peroxide, 30%, were purchased from Caledon Laboratories. All substrates are made out of GE-124 fused quartz with a dimension of 1×1 cm supplied by Technical Glass. Citrate-capped 40 nm gold nanoparticles (AuNPs) were purchased from BBInternational. Phosphate buffered saline, pH 7.4; N-(3-dimethylaminopropyl)-N′-ethylcarbodiimide hydrochloride (EDC), N-hydroxysuccinimide (NHS), sodium chloride, dithiobis(succinimidyl propionate) (DSP), bovine serum albumin (BSA), 4-aminophenylacetic acid, tetrafluoroboric acid (48% wt in H_2O), sodium nitrite, and 4-nitrobenzenethiol (tNB) were purchased from Sigma-Aldrich. BupH™ Borate buffer packs, pH 8.5, and SuperBlock PBS Blocking Buffer, pH 7.4, were obtained from Thermo Scientific. All buffer solutions were prepared in deionized water. Immunogold conjugates, goat anti rabbit IgG coated 40 ± 3 nm AuNPs, acquired from BBInternational with an optical density of 10.2 corresponding to approximately 8×10^{11} particles/mL suspended in 2 mM sodium tetraborate (pH 7.2). Purified goat IgG (g-IgG), purified rabbit IgG (r-IgG), and goat affinity purified antibody to rabbit IgG (r-AB), were obtained from MP Biomedicals. Deionized water with a resistivity of 18 MΩ-cm or better was obtained with a Millipore Milli-Q Plus purification system.

Titanium deposition. All quartz substrates were cleaned with a hot piranha solution consisting of 4:1 (98% sulfuric acid: 30% hydrogen peroxide) for 30 minutes followed by thorough rinsing in deionized water and dried under a

stream of argon gas. *Warning: Piranha solution should be handled with extreme care; it reacts violently with organic materials, presenting an explosion danger.* The cleaned substrates are placed either inside a Kurt J. Lesker PVD 75 or a Johnsen Ultravac Model 6100 e-beam evaporation system in Dr. Richard McCreery's research facilities at NINT, and with the help of Amr Mahmoud a 5 nm titanium film was coated on the quartz substrate with a deposition rate of 0.3 Å/s and at a base pressure of 2×10^{-7} Torr.

Titanium surface modification. Phenylacetic acid diazonium salt (dPAA) was used to modify the titanium film and it was synthesized in our group according to a previously published procedure by Starkey.[32] Briefly, the starting material, 0.1 M of 4-aminophenylacetic acid dissolved in 60 mL fluoroboric acid was cooled to 0°C. Next, 0.12 M sodium nitride dissolved in deionized water was added dropwise to the starting material with continuous stirring. The temperature of the reaction mixture was kept near 0°C. After 30 min the product was filtered and washed with cold ether repeatedly. The product was purified during recrystallization by dissolving it in a minimal amount of acetonitrile and precipitating it by adding cold ether. Phenylacetic acid diazonium salt was dried in a rotovap and stored at -18°C until use. The synthesized diazonium salt was characterized with IR and NMR to verify that the desired product was formed.

In order to prevent oxidation of the Ti film, the freshly prepared Ti coated quartz substrates were immediately placed in an acetonitrile solution containing 5 mM dPAA for 1 h. Subsequently, the substrates were rinsed with acetonitrile and blown dry under a stream of nitrogen.

Atomic force microscopy (AFM). In order to determine the phenylacetic acid (dPAA) layer thickness, a 5×5 μm area on the silane modified quartz surface was first imaged in tapping mode and then a 2×2 μm region was "scratched" by 10 cycles at 5 Hz in contact mode. Afterwards the "scratched" area was re-imaged in tapping mode and a height profile showed the difference between the undisturbed and disturbed area corresponding to the dPAA film thickness on the surface. The same procedure was repeated for an unmodified Ti film on quartz substrate in order to determine if the applied force during contact mode caused damage to the titanium film.

The above-mentioned work was carried out on a Digital Instruments Nanoscope III Multimode microscope using an Olympus Si cantilever with a spring constant of 2 N/m. The oscillation frequency used for tapping mode was 72 ± 4 kHz and a contact force of 0.09 μN was used for all contact mode experiments corresponded to a setpoint of 0.500 V. The applied force, $F_{applied}$, was determined using the relationship:

$$F_{applied} = \frac{V_S - V_B}{S} k_{spring} \quad (5\text{-}01)$$

where V_S is the setpoint voltage used in contact-mode, V_B is the voltage required to break the tip away from the surface (-0.1198 V), and S is the cantilever sensitivity to bending (0.01387 V/nm), and k is the spring constant for the cantilever (2 N/m).

Nanoparticle label preparation. A 1 mL solution of 40 nm gold nanoparticles (9×10^{10} particle/mL) was adjusted to pH 8.5 by adding 40 μL of 50 mM borate buffer. Then, 8 μL of 1 mM tNB and 2 μL of 1 mM DSP in

acetonitrile were added to the AuNPs and allowed to react for 6-8 h. Afterwards 20 μL of 1 mg/mL rabbit IgG antibody (r-AB) solution was added to the nanoparticle suspension and incubated for 18 h. In order to block any non-reacted succinimidyl ester sites, 100 μL of a 10% BSA solution was mixed with the modified nanoparticles and left to react for 1 h. Finally, the r-AB coated nanoparticles were separated from left-over reactants by centrifuging the solution at 6000 rpm for 10 min and re-suspending the modified AuNPs in 2 mM borate buffer. The centrifugation step was repeated once more at 4000 rpm for 10 min to clean the NP solution further and the final solution volume was reduced to 450 μL to concentrate the nanoparticles. Moments before the analyte is exposed to the NP labels, 50 μL of 1.5 M NaCl is added to the nanoparticle solution to aid in antibody-antigen interactions. The final label concentration is approximately 2×10^{11} particles/mL. This procedure is a modified version of previously published work.[33]

Sandwich immunoassay steps. The first step was to covalently link the capture agent (r-AB) to the transparent substrate. This was accomplished by exposing the dPAA film to an aqueous solution of 0.4 M EDC and 0.1 M NHS for 30 min to activate the carboxylic acid groups. Afterwards the surface was briefly rinsed with deionized water and immediately exposed to 600 mM r-AB in 0.1 M PBS buffer for 18 h followed by rinsing with PBS buffer. In order to block any unreacted succinimidyl ester sites the surface was exposed to SuperBlock blocking buffer for 1 h and rinsed with PBS buffer. At this stage the biochip was

ready to be exposed to varying concentrations of analyte (r-IgG) in 0.1 M PBS buffer for 2 h followed by rinsing with 2 mM borate buffer.

The analyte was labeled on the biochip surface by incubating the substrate with 0.5 mL of r-AB modified 40 nm gold nanoparticles for 18 h followed by rinsing with 2 mM borate buffer or deionized water and drying under a stream of nitrogen. Both the commercially available and in-lab r-AB modified 40 nm gold nanoparticles were used.

Infrared reflection absorption spectroscopy (IRRAS) measurements. The dPAA film formation, succinimidyl ester conversion and the nanoparticle binding in the assembly of the sandwich immunoassay were monitored with IRRAS. In order to obtain a reflective substrate while maintaining the titanium film, a gold-coated microscope slide (fabricated by the procedure outlined in Chapter 3) was coated with the same 5 nm Ti film used for the quartz substrates above. This substrate then underwent the same surface modifications as outlined above for the sandwich immunoassay. IRRAS spectra were collected on a Mattson Infinity Series Fourier transform infrared spectrometer equipped with a mercury-cadmium-telluride (MCT) detector cooled with liquid nitrogen. The sample was probed with a p-polarized IR beam incident at an angle of 80° with respect to the surface normal. All spectra were collected by averaging 1000 scans at a resolution of 2 cm^{-1}. An unmodified Ti film on a gold-coated microscope slide was used as a reference.

Extinction Spectroscopy. All biochips were analyzed with UV-vis spectroscopy to measure the LSPR band intensity from the nanoparticles

immobilized on the transparent quartz surface. The extinction spectra for adsorbed nanoparticles were obtained in transmission mode on a double-beam Perkin Elmer Lambda 35 spectrophotometer with a photodiode detector. The UV-vis spectrum was scanned from 200 to 1100 nm with a scan rate of 960 nm/min. Ti coated / dPAA modified quartz slides were used as the blank.

Scanning Electron Microscopy (SEM). The Ti film was sufficiently conducting to prevent charging during SEM analysis. SEM images were collected by Jane Cao or Ryan Lister on a Hitachi S4800 Field Emission SEM in the Hitachi Electron Microscopy Products Centre (NINT). Image acquisition on the Hitachi SEM was carried out with a 10.0 kV accelerating voltage, a 15 μA emission current and working distance of approximately 20-24 mm.

5.3 RESULTS AND DISCUSSION

The two main requirements for the proposed sandwich immunoassay are the modification of gold nanoparticles with rabbit IgG antibodies (r-AB) and the immobilization of capture antibodies (r-AB) on a transparent substrate. The analyte, rabbit IgG (r-IgG), was sandwiched between the transparent substrate and the NP label. Consequently, the nanoparticle modification will be discussed followed by fabrication and characterization of the transparent substrate. The combined bioassay design was tested and compared to other comparable techniques presently at use.

5.3.1. Nanoparticle surface modification and monitoring.

The modification scheme for the gold nanoparticles is shown in Figure 5.02A. A mixed monolayer of 4-nitrobenzene thiol (tNB) and dithiobis(succinimidyl propionate) (DSP) is used to maintain colloidal stability. We find that the NPs tend to aggregate when modified solely with DSP. Our group's experience in modifying NPs for SERS labels led me to used tNB as a diluent molecule to maintain stability, while r-AB was covalently linked to the nanoparticle surface through DSP. The sensitivity of the LSPR band towards changes in the refractive index of the NP surface and the surrounding medium was discussed in Chapter 1 and 3. The refractive index of an organic monolayer is typically higher than the refractive index of a solvent.[34] Therefore we expect a red-shift in λ_{max} as the nanoparticle surface is modified. This effect is monitored by UV-vis spectroscopy as shown in Figure 5.02B. Upon adsorption of DSP and

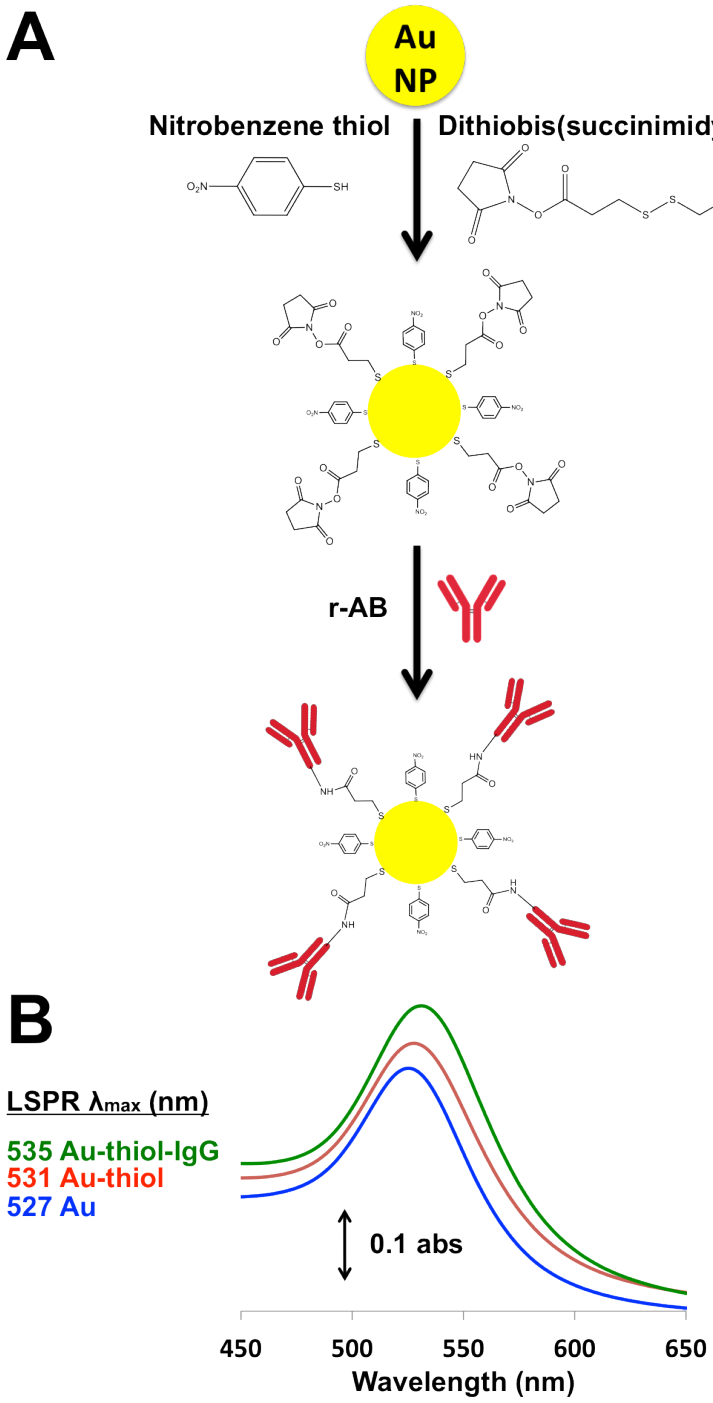

Figure 5.02. Schematic overview of the process involved to immobilize IgG antibodies to NPs: (A) Stepwise modification of gold nanoparticles (AuNPs) and (B) Extinction spectra tracking the modification of AuNPs. All spectra were collected in water.

tNB to the NP surface the LSPR band maximum shifts from 527 nm to 531 nm indicating a change in the refractive index of the AuNP surface. The shift is even more pronounced upon r-AB immobilization, with a red shift to 535 nm. This can be explained by the layer thickness term, *d*, expressed in the equation for $\Delta\lambda_{max}$ presented in Chapter 1 and 3. The magnitude of the red-shift increases as the organic film becomes thicker. We would expect a layer of r-AB to increase the film thickness substantially and the UV-vis spectrum confirms this. Lastly, no broadening in the LSPR band is observed upon modification, and the absence of a second band at higher wavelengths rules out any aggregation in the nanoparticle suspension.

5.3.2 UV-vis spectroscopy of Ti film and dPAA layer.

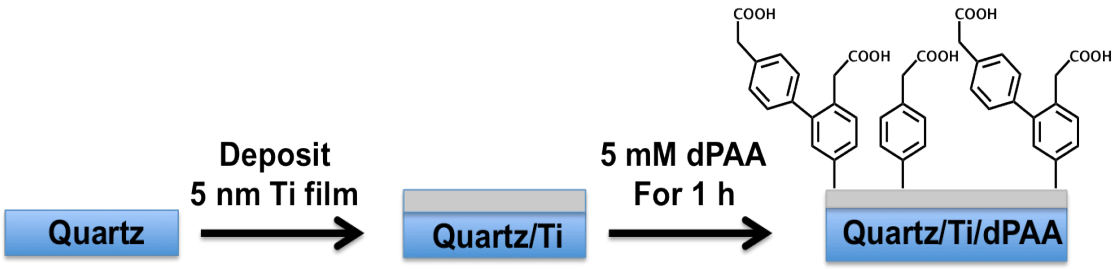

Figure 5.03. A schematic representation of the surface preparation involved in immobilizing biomolecules to optically transparent quartz. Phenylacetic acid diazonium salt (dPAA) is spontaneously adsorbed to a freshly deposited titanium film (5 nm).

The modification of quartz surfaces with silane chemistry to form an amine-terminated monolayer to adsorb nanoparticles was described in the previous chapter. In the current chapter we needed to covalently link biomolecules to the quartz surface, a process that typically requires buffers and extended incubation periods. It was mentioned in the Section 5.1 that amine-terminated silanes are prone to hydrolysis and therefore we have chosen to utilize a different substrate and surface chemistry. Quartz substrates were coated with a thin film of titanium to spontaneously adsorb dPAA as shown in Figure 5.03. The rabbit antibody immobilization was then carried out by activating the carboxylic acid group on the surface with EDC / NHS chemistry. This chemistry converts the carboxylic acid group to a succinimidyl ester, which couples to an IgG through an amide linkage.[35-37] The resulting dPAA film will be characterized with UV-vis spectroscopy, IRRAS and AFM.

One of the main requirements for the substrate and its associated surface chemistry is transparency. This is especially important in the wavelength region that is occupied by the LSPR band for gold and silver nanoparticles. In Chapter 4 this region was determined to be between 300-700 nm. The optical properties were investigated by collecting a UV-vis spectrum of both the freshly prepared Ti film and the dPAA modified Ti film (Figure 5.04A). The absorbance is reasonably uniform between 400-1100 nm allowing about 60 % of the light to pass through. The substrate becomes more transparent near 300 nm and then rapidly absorbs more light towards shorter wavelengths and becoming less transparent. Both the Ti film by itself and the dPAA modified Ti film exhibit

similar absorption behavior, which shows low absorbance in the spectral region occupied by the gold NP LSPR band.

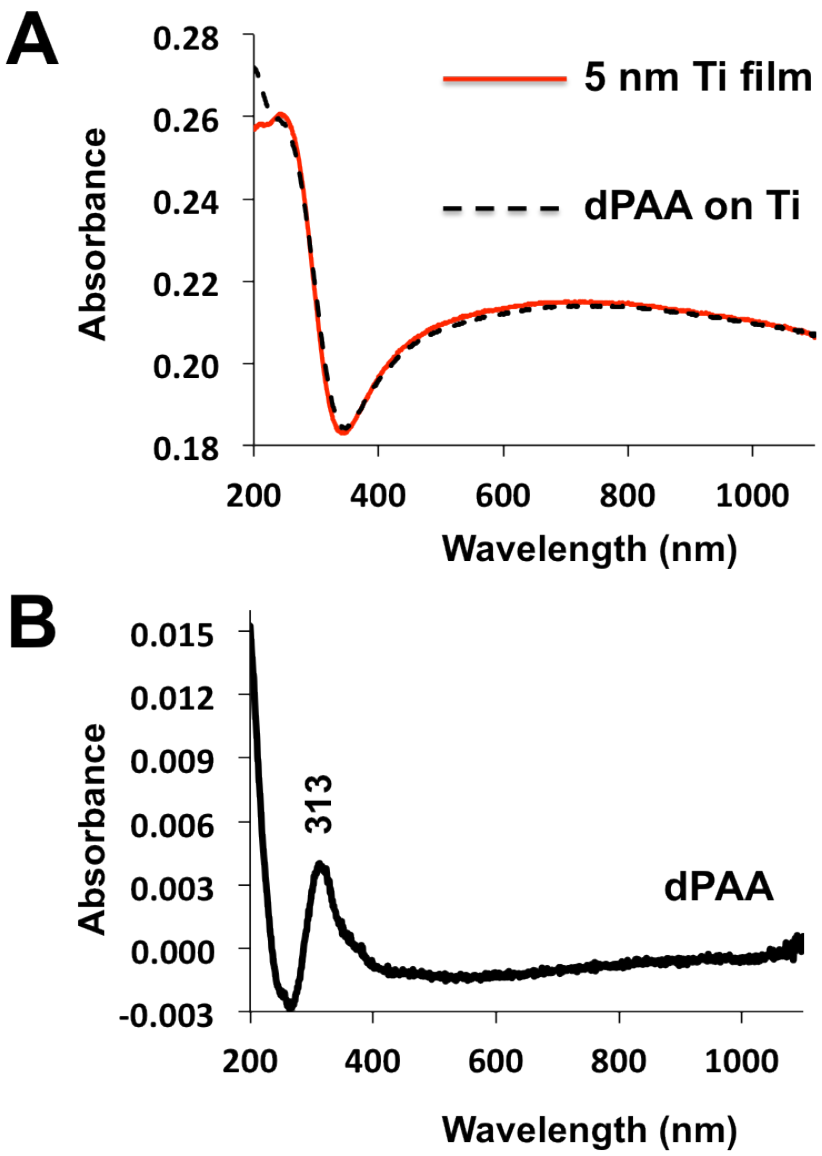

Fig. 5.04. UV-vis spectra referenced to quartz for a 5 nm titanium film on quartz and for a subsequent adsorption of dPAA to the titanium film (A). The difference spectrum for the curves is plotted in (B) highlighting the absorption band for dPAA at 313 nm.

One method to confirm the presence of dPAA on the surface is to determine the difference spectrum between the two curves in Figure 5.04A. This difference spectrum is shown in Figure 5.04B and exhibits an absorption band at 313 nm, which is red-shifted from phenylacetic acid in methanol solution (250-270 nm).[38] We note that the red-shift is on the order of 50 nm, but due to crosslinking of phenylacetic acid molecules during multilayer formation this absorbance band can be shifted to higher wavelengths. Also, the dPAA molecules can interact with the substrate causing a shift in the absorption band. However, the presence of such a band near 300 nm is evidence that a dPAA film has formed on the surface.

5.3.3 Atomic force microscopy (AFM) characterization of dPAA film.

The extent of multilayer formation and the topography of the dPAA layer were probed with AFM. Both the height images of the unmodified titanium film (RMS roughness of 0.4 ± 0.1 nm) and the dPAA film (RMS roughness of 0.6 ± 0.1 nm) are shown in Figure 5.05A and B respectively. Both surfaces exhibit low RMS roughness and have a uniform topography throughout the 5×5 μm area. A few tall features, which could indicate localized aggregation, are present on the dPAA image (figure 5.05B). However, these features are also present to a lesser extent on the unmodified Ti surface indicating that they could have resulted from air contaminants during sample handling. Solely based on the height images in Figure 5.05A and B the surface modification cannot be proven. A “scratch” test as used in Chapter 4 was undertaken to probe the dPAA film further. A 2×2 μm area

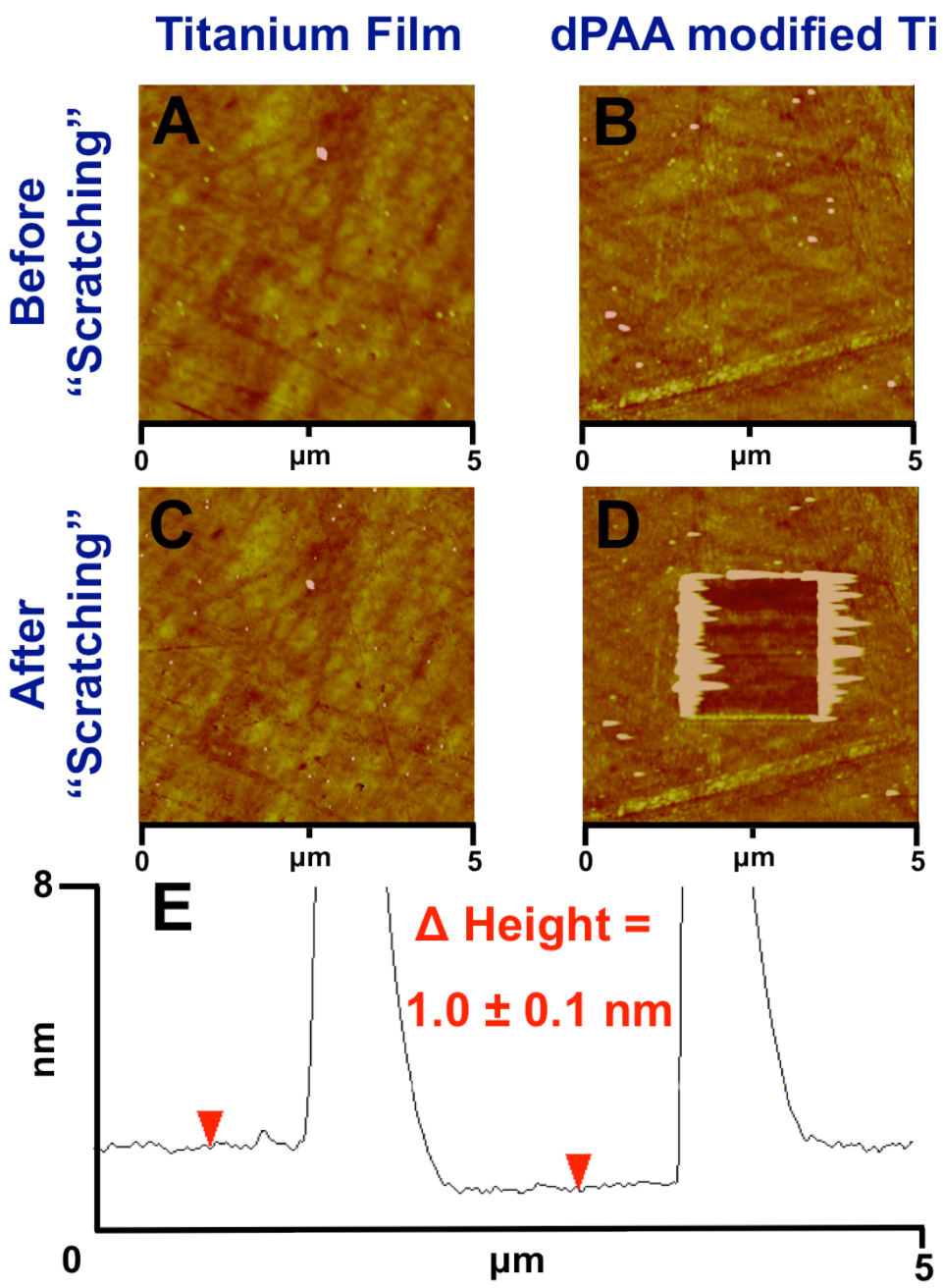

Figure 5.05. Tapping-mode AFM height images with a 10 nm z-scale before scratching (A: unmodified titanium film), (B: dPAA modified Ti film) and after scratching a 2×2 µm area (C: unmodified titanium film), (D: dPAA modified Ti film). Section analysis of scratched area for dPAA modified Ti surface (E).

was scratched in contact-mode and re-imaged in tapping-mode. The height image of the unmodified Ti film after scratching (Figure 5.05C) looks similar, but the dPAA height image (Figure 5.05D) changed significantly after the scratching step. The removal of a layer on quartz from "scratching" indicates that the dPAA surface has been modified and from the cross-sectional profile in Figure 5.05E the film thickness was determined to be 1.0 ± 0.1 nm. The molecular length derived from a phenylacetic acid crystal structure is approximately 0.7 nm.[39] Comparing the calculated length to the film thickness determined by AFM, we propose a multilayer formation consisting of 1-2 layers of dPAA as shown in Figure 5.03. In conclusion, the surface topography of the modified Ti substrate indicates a very uniform layer and the "scratch" test confirms the presence of a film derived from the spontaneous adsorption of dPAA on titanium.

5.3.4 Carboxylic acid activation and biomolecule immobilization.

Hitherto, the biochip substrate and the required surface chemistry for the immobilization of biomolecules has been introduced and characterized. All subsequent steps are outlined in Figure 5.06. The next step in the sandwich immunoassay was to covalently link the capture agent (r-AB) to the phenylacetic acid layer by activating the carboxylic acid groups with EDC/NHS. The resulting succinimidyl ester functionality reacts with a primary amine group on the rabbit IgG antibodies to form an amide linkage with the dPAA film on the transparent substrate as shown by the first 3 steps in Figure 5.06. The remaining two steps in Figure 5.06 show the capturing of the analyte (r-IgG) followed by "sandwiching"

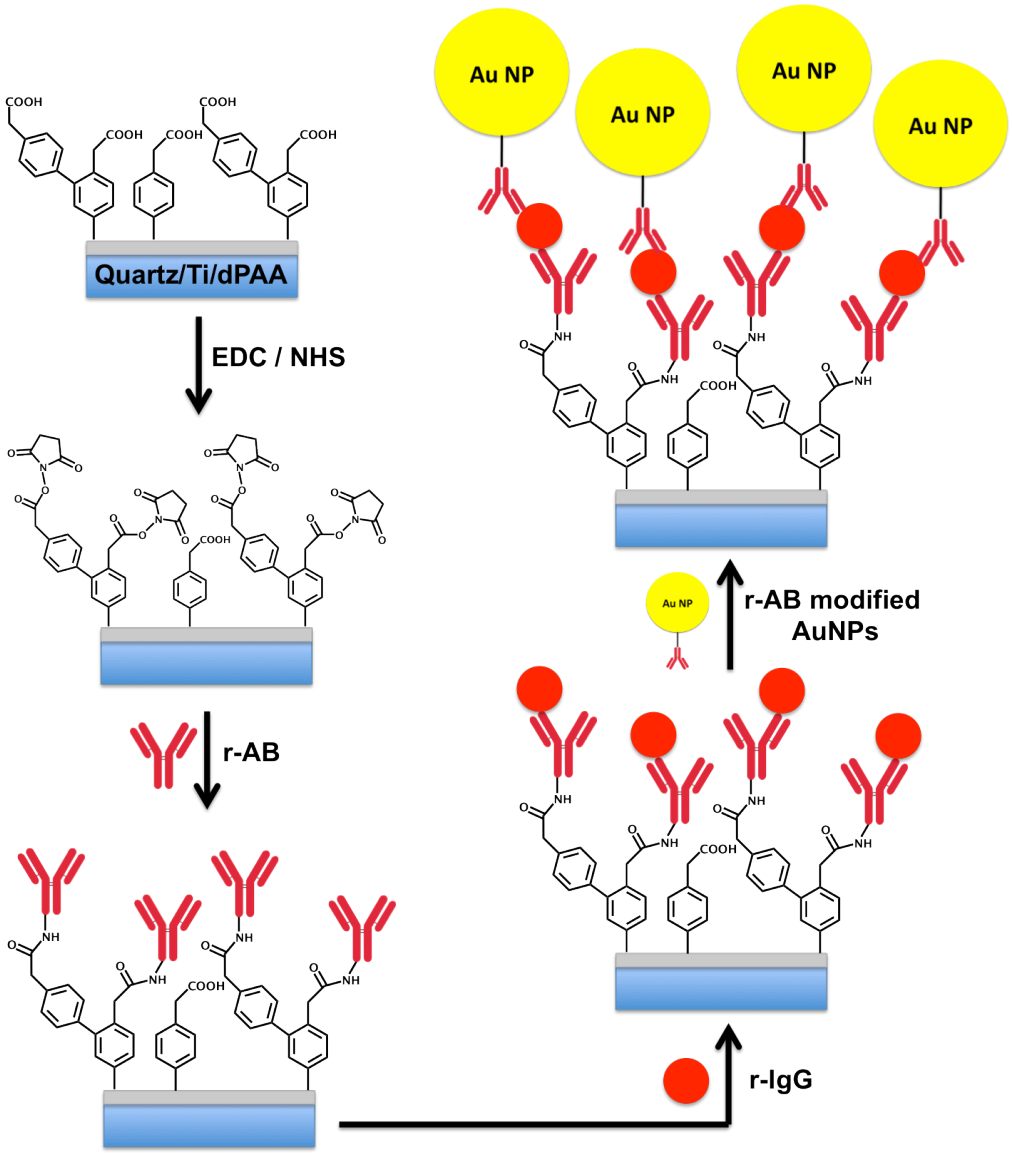

Figure 5.06. Schematic representation of the steps involved in the proposed sandwich immunoassay from protein immobilization to nanoparticle labeling. The carboxylic acid groups are converted into a succinimidyl ester with EDC/NHS and rabbit antibody (r-AB) is linked to the surface. Then the surface is exposed to the analyte, rabbit antigen (r-IgG), followed by the label exposure for detection, r-AB modified gold nanoparticles (AuNPs).

the analyte between the capture agent and an extrinsic label, r-AB modified AuNP.

The dPAA film formation, EDC/NHS activation and the analyte labeling with AuNPs have been monitored by IRRAS (Figure 5.07). The major bands and their assignments are listed in Table 5.1. We note that IRRAS can also be used quantitatively to monitor the amount of analyte captured, but it was not the goal of this work to verify the antigen-antibody binding as such interactions are well studied.[40-42] The IR spectrum of the dPAA layer in Figure 5.07 is as expected, showing the C=O stretch (1712 cm^{-1}), ring stretching (1597 and 1507 cm^{-1}) and a symmetric carboxylate stretch (1423 cm^{-1}). Upon exposure to EDC/NHS several new bands appear that correspond to the conversion of the carboxylic acid group to a succinimidyl ester moiety. The bands at 1813 and 1781 cm^{-1} result from the succinimide group and correspond to an asymmetric and symmetric C=O stretch respectively. Another C=O stretch stemming from the ester carbonyl is observed at 1741 cm^{-1} and, lastly, the ring stretching doesn't change significantly from the dPAA IR spectrum (1599 and 1508 cm^{-1}). These band positions and assignments are in agreement with previously published reports. [40, 43, 44]

The IRRAS spectrum of the complete sandwich immunoassay (IgG/AuNPs) in Figure 5.07 is more complex due to the variety of molecules adsorbed to the surface of the substrate. We would expect the IR spectrum to be dominated by protein-derived bands as both rabbit antigens and antibodies are present in significant amounts. Typically the presence of protein results in two strong bands in IR spectra (amide I and amide II).[45] These bands stem from the

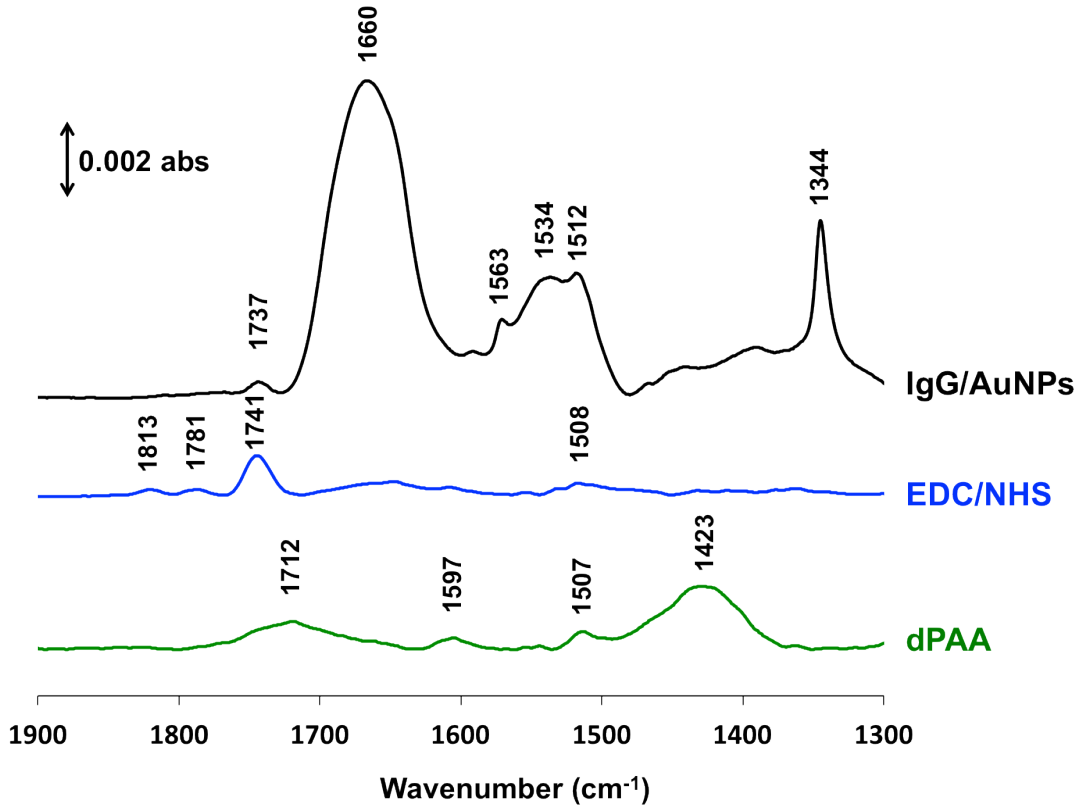

Figure 5.07. Infrared reflection absorption spectroscopy (IRRAS) spectra for phenylacetic acid (dPAA) adsorbed to titanium, EDC/NHS activation of dPAA layer and a completed sandwich immunoassay with rabbit IgG antibody modified AuNPs at the surface. The Ti film has been deposited on a 300 nm gold film to provide a reflective surface for IRRAS.

Table 5.1. Band position and assignments for IRRAS spectra of phenylacetic acid (dPAA) adsorbed to titanium, EDC/NHS activation of dPAA layer and a completed sandwich immunoassay with rabbit IgG antibody modified AuNPs at the surface. (References 40, 43, and 44 were used for some assignments)

	Band position (cm^{-1})		
Assignment	**dPAA**	**EDC/NHS**	**IgG/AuNPs**
Asymmetric C=O stretch (succinimide)	–	1813	–
Symmetric C=O stretch (succinimide)	–	1781	–
C=O stretch (ester)	–	1741	1737
C=O stretch (carboxylic acid)	1712	–	–
Amide I band	–	–	1660
Amide II band	–	–	1534
Aromatic Ring stretch	1597, 1507	1599, 1508	1587, 1563 1512
Symmetric COO^- stretch	1423	–	–
Symmetric NO_2 stretch	–	–	1344

amide linkage between the numerous peptides in a protein. The amide I band (1600-1700 cm^{-1}) is the most prominent vibrational mode with a C=O stretch as its major component and the amide II band (1500-1600 cm^{-1}) is less intense containing C-N stretching and N-H in-plane bending.[45, 46] Both of these modes are observed in the IgG/AuNPs IR spectrum in Figure 5.07 along with ring stretching modes from the initial dPAA layer and from nitrobenzene thiol (tNB) present on the gold nanoparticle surface. The ring stretches listed in Table 5.1 for

IgG/AuNPs at 1587 and 1512 cm^{-1} are due to the dPAA film, while the remaining ring stretch at 1563 cm^{-1} is attributed to the tNB layer on the AuNP. Also, the asymmetric NO_2 stretch at 1344 cm^{-1} results from the presence of tNB. The amide I and II band location at 1660 cm^{-1} and 1534 cm^{-1}, respectively, are in agreement with the above-mentioned ranges for those vibrational modes.

There also appears to be residual activated succinimidyl ester groups present (C=O stretching at 1737 cm^{-1}) either on the NP or on the titanium surface. The presence of such groups is indicative of an incompletely blocked surface. These unreacted ester groups can be a result of size constraints as not all groups will be accessible by larger biomolecules such as antigens or antibodies used in the assay. Further, the blocking steps outlined in Section 5.2 that typically include small proteins such as BSA to prevent non-specific binding from occurring also seem unable to cover all unreacted succinimidyl ester groups. The presence of this incomplete blocking can lead to an increase in non-specific binding. In order to improve upon detection limits in the future other blocking steps need to be considered.

The IRRAS results confirm the activation of the carboxylic acid layer on the substrate, the covalent attachment of the capture agent (rabbit IgG antibodies) and the completion of the bioassay that includes the capturing of the analyte and the subsequent labeling *via* AuNPs. In the following sections the bioassay design will be tested quantitatively with the desired UV-vis detection method, which is based on the magnitude of the LSPR band from the AuNP-labels, and these results will be compared to SEM derived NP surface densities for validation.

5.3.5 Transmission UV-vis spectroscopy of AuNP labels in bioassay.

The utilization of gold nanoparticles in sandwich immunoassays was evaluated based on two types of AuNP-labels: in-lab modified labels coated with rabbit IgG antibodies (r-AB) and commercially available r-AB coated AuNPs. The typical responses from UV-vis spectroscopy for a complete assay with in-lab modified AuNP-labels are shown in Figure 5.08. The extinction curves from the various concentrations of analyte (r-IgG) ranging from 100 pM to 100 nM are displayed in Figure 5.08A. The magnitude of the LSPR band clearly scales with the r-IgG concentration. Figure 5.08B highlights the lower end of the concentration range (100 pM) and compares this response to a control sample containing 20 nM goat IgG, which should not bind to the modified surface. Although non-specific binding did occur it was well below the 100 pM analyte response. Another important aspect that can be obtained from the various extinction curves is information about NP aggregation. As mentioned earlier, a second band at higher wavelength would appear if NP aggregation has taken place. The absence of such a band is proof that the AuNPs did not aggregate at the biochip surface. We do, however, observe a slight shift in λ_{max} at a r-IgG concentration of 100 nM. This is most likely due to the close proximity of the NPs at the surface at these high concentrations allowing for LSPR coupling or possibly the beginning of NP aggregation. SEM imaging will be described in Section 5.3.6 to investigate this further.

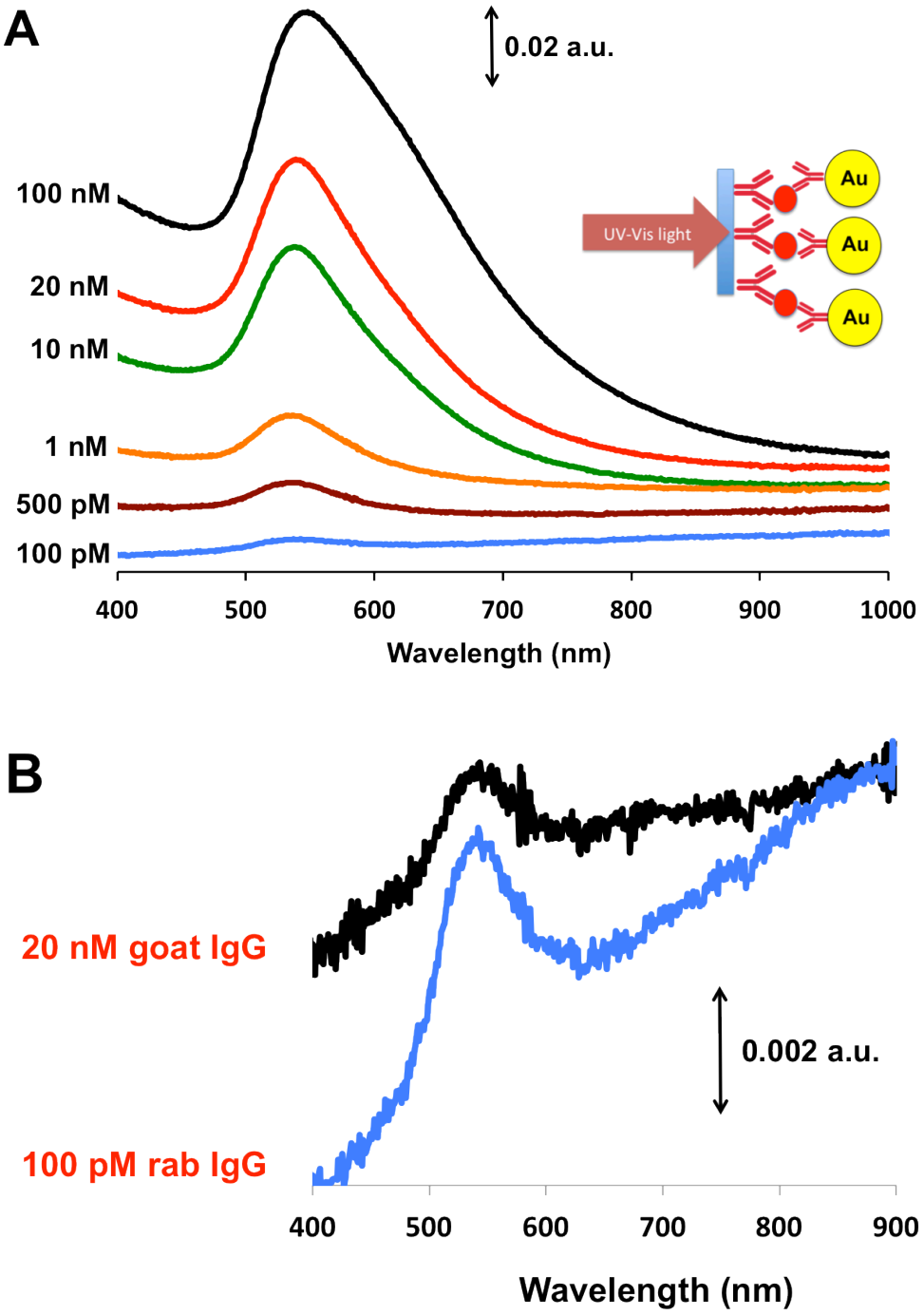

Figure 5.08. Extinction curves for one complete sandwich immunoassay utilizing in-lab modified AuNP-labels. (A) displays the resulting LSPR bands for various concentrations of rabbit IgG and (B) shows a magnified region of the lower concentration range versus a goat IgG control run.

The results for in-lab modified and commercially coated AuNP-labels at the various analyte concentrations are summarized in Figure 5.09A and B, respectively. In each plot the extinction-response increases as the analyte (r-IgG) concentration increases until the surface has been saturated with analyte resulting in the response to level-off. The maximum concentration analyzed was 1000 nM and produced a similar response to that for 100 nM, indicating that saturation coverage has already been reached at 100 nM (not shown in Figure 5.09). The magnified areas in Figure 5.09 highlight the lower end of the concentration range. The lowest [r-IgG] analyzed was 100 pM and was chosen as the lowest detectable analyte concentration. The response for 100 pM lies above the generally-defined limit of detection (blank signal + $3\sigma_{Blank}$), which can be approximated by three times the peak-to-peak noise shown in the magnified regions in Figure 5.09. Also non-specific binding was taken into consideration when determining the lowest detectable concentration, as this is a common concern in surface-based bioassays. Non-specific binding was evaluated by exposing the capture layer to a high concentration of goat IgG (20 nM) instead of r-IgG (analyte). This "control" test exhibited minimal non-specific binding as shown in Figures 5.08 and 5.09. The "control" response is above the LOD (~3×peak-to-peak noise), but below the response for the lowest concentration of r-IgG thereby supporting the claim of a detection limit of 100 pM for the IgG analyte. This establishes the range of our sandwich immunoassay from 100 pM to approximately 100-1000 nM yielding a dynamic range of 3-4 orders of magnitude, which is common for surface based bioassays.

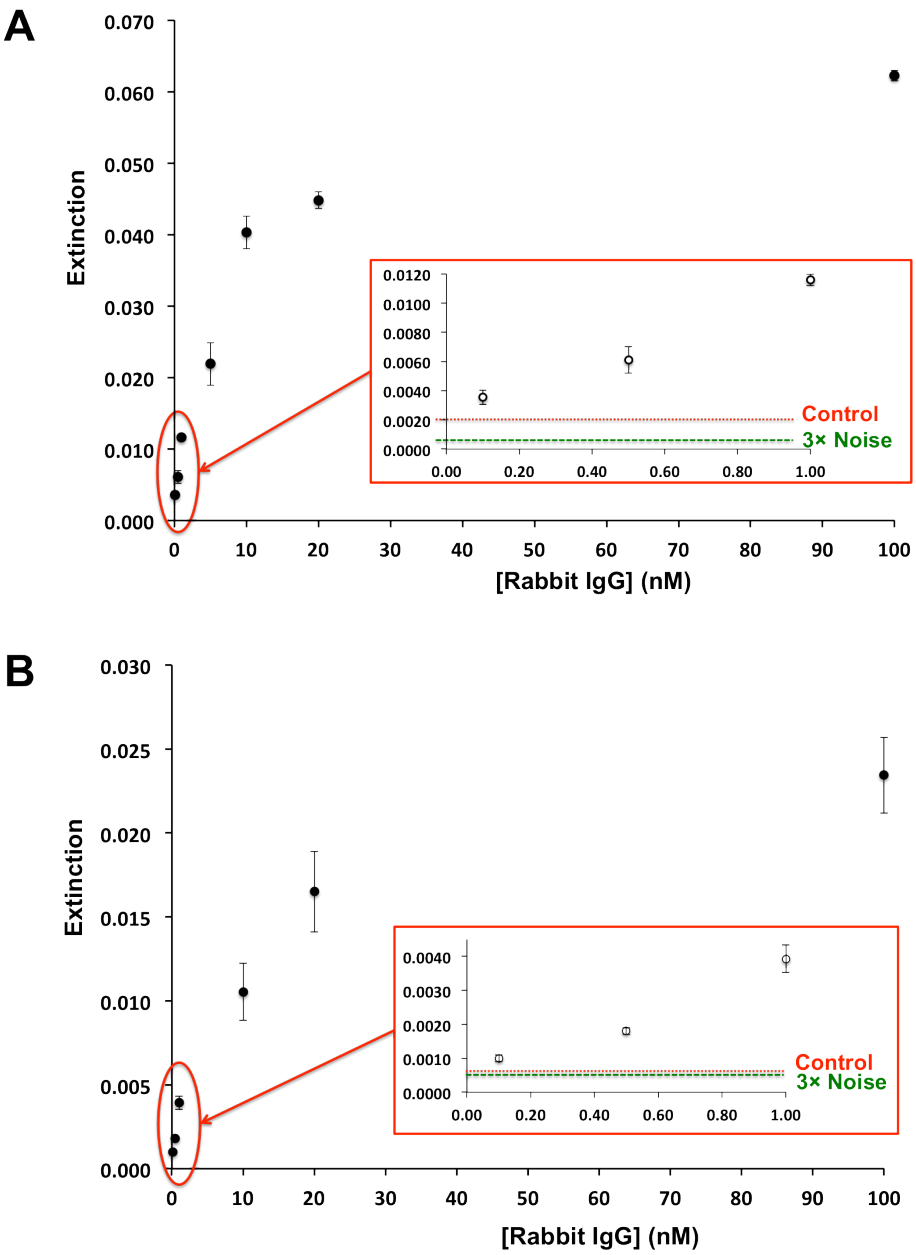

Figure 5.09. Response (Extinction) versus analyte (Rabbit IgG) concentration plots for a sandwich immunoassay on quartz that utilizes an UV-vis detection relying on the magnitude of the LSPR band from r-AB coated 40 nm gold nanoparticles either modified in-lab (A) or commercially acquired (B). The error bars represent the standard deviation of the mean for a minimum of 2 separate bioassays.

One marked difference between the two types of AuNP-labels used in the assay is the magnitude of the response. The in-lab modified labels produce 2-4 times the response for an identical concentration of analyte compared to the commercially available labels (Figure 5.09). The amplification in signal appears to be consistent throughout the dynamic range of the assay. We note that such a difference seems unusual when considering the typically strong antibody-antigen interaction. One possible explanation can be a change in the AuNP-label concentration, but in fact the commercially available AuNPs were used at a slightly higher concentration than the in-lab modified labels. The most likely explanation includes factors such as antibody activity, antibody orientation, and adsorption equilibrium time. It is conceivable that the in-lab modified AuNPs result in a more active antibody surface that offsets the concentration difference and speeds up surface labeling resulting in a higher density during the same incubation period. However, this would assume that a 24 h period is not enough to reach equilibrium coverage under the conditions used and such an effect would have to be investigated in future studies. More importantly, the assay behaves as a typical surface-based immunoassay, where errors on the order of 10 % RSD for the in-lab modified AuNP-labels and even ~10-30 % RSD for the commercially available AuNP-labels are common in these kind of bioassays.[47, 48]

5.3.6 Scanning electron microscopy (SEM) imaging of immunoassay.

The individual biochips were imaged with SEM at the various rabbit IgG concentration to verify that the response (extinction) correlates with nanoparticle density on the biochip. Figure 5.10 and 5.11 show the SEM images of the in-lab

and commercially available labels, respectively. For each set of labels the same 6 different analyte concentrations used for transmission UV-vis spectroscopy were investigated with SEM and a nanoparticle surface density was determined for each case. The SEM-determined particle density is plotted versus analyte concentration (Figure 5.12) in an analogous fashion as the extinction vs. analyte concentration plots shown in Figure 5.09.

The SEM images for the in-lab modified labels in the sandwich immunoassay for the following analyte concentrations (100 nM, 20 nM, 10 nM, 1 nM, 0.5 nM and 0.1 nM) are shown in Figure 5.10A-F. All images were collected at the same magnification and a visual inspection reveals the expected trend: nanoparticle density decreases as the analyte concentration is decreased. In all six images the nanoparticles are generally well dispersed with a few clusters present throughout. This aggregation into clusters is more prevalent at higher analyte concentration. A possible explanation for the clusters is an incomplete modification of the NP surface that results in aggregation at higher NP densities. The appearance of aggregates at higher concentrations explains the shift in λ_{max} observed in Figure 5.08. Furthermore, there appear to be salt crystals present in the SEM images apparent as square or irregular shaped structures, larger in size than 40 nm AuNPs. These salt crystals stem from the last washing step in the sandwich immunoassay with 2 mM borate buffer and can be prevented by rinsing with deionized water instead. Overall the salt crystals do not interfere with the assay reproducibility, as the nanoparticle density for several runs for in-lab modified labels has been consistent.

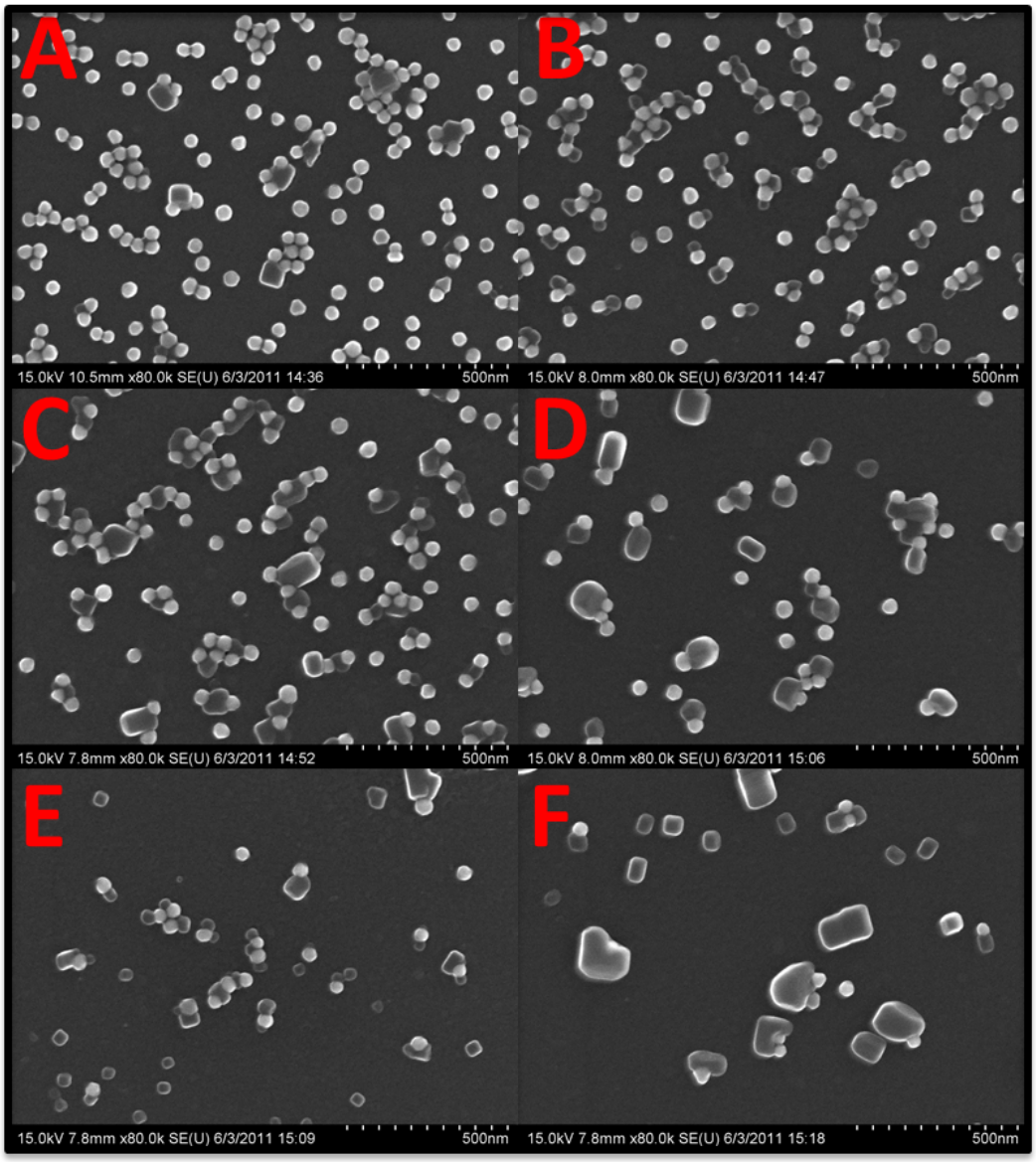

Figure 5.10. SEM imaging of the sandwich immunoassay biochip showing the in-lab modified 40 nm gold nanoparticles with rabbit IgG antibodies bound to various analyte (rabbit IgG) concentrations on the biochip: (A) 100 nM, (B) 20 nM, (C) 10 nM, (D) 1 nM, (E) 500 pM, and (F) 100 pM. All images are magnified by a factor of 80k.

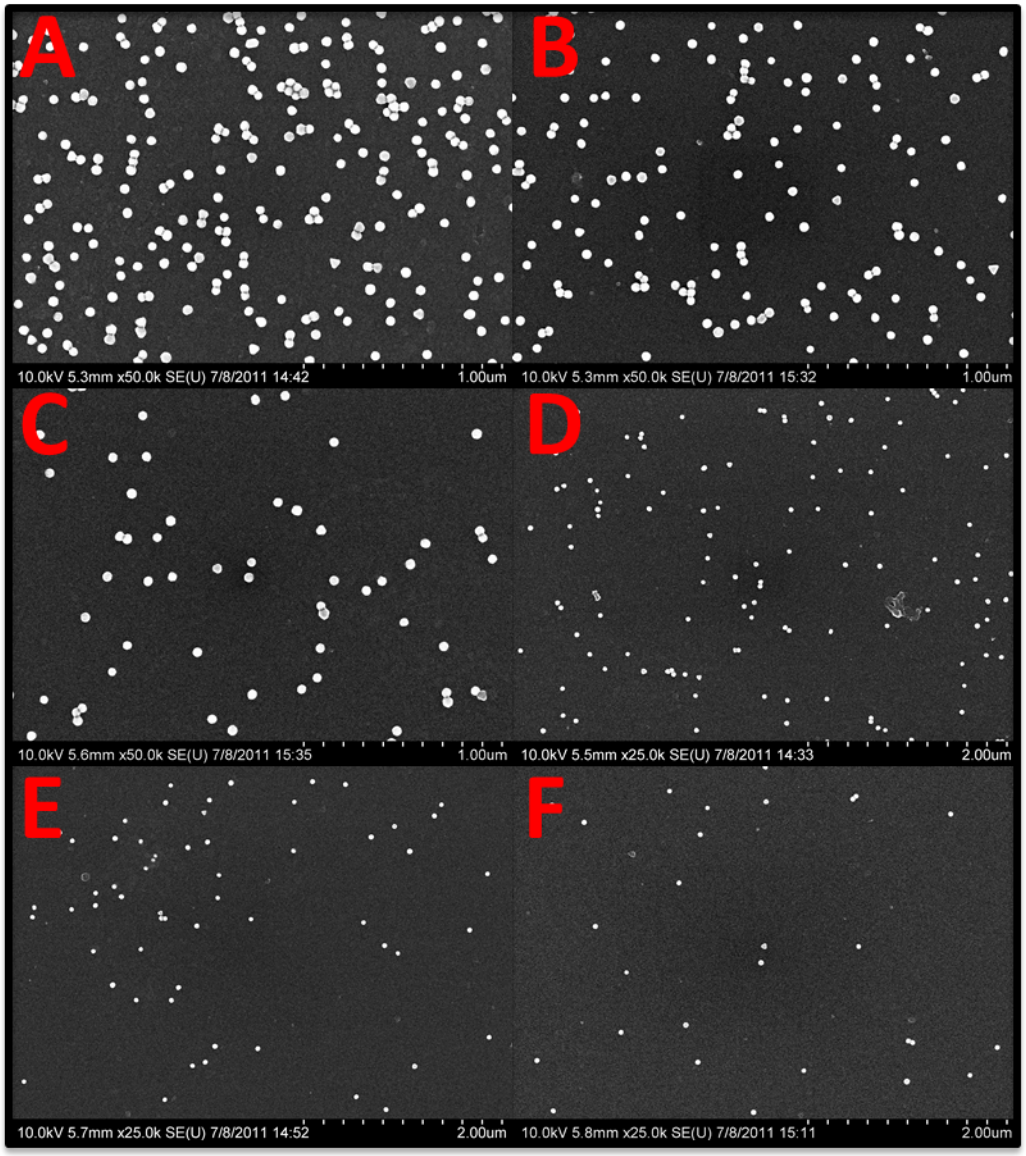

Figure 5.11. SEM imaging of the sandwich immunoassay biochip showing the commercially available 40 nm gold nanoparticles coated with rabbit IgG antibodies bound to various analyte (rabbit IgG) concentrations on the biochip: (A) 100 nM, (B) 20 nM, (C) 10 nM, (D) 1 nM, (E) 500 pM, and (F) 100 pM. The images are magnified by either a factor of 50k or 25k as indicated on the bottom of each image.

The other set of images shown in Figure 5.11A-F correspond to the sandwich immunoassay with commercially coated AuNPs and [analyte] ranging from 100 nM to 100 pM. These images also demonstrate the decrease in nanoparticle density as the analyte concentration is decreased. There is, however, a difference between the two labels: the commercially coated labels in Figure 5.11 seem to exhibit less aggregation and generally a lower density on the biochip is observed. It is possible that the coating surrounding the nanoparticle is more uniform preventing aggregation or that the aggregation is minimal at the lower particle densities observed for commercially coated AuNPs. In terms of viewing similar NP densities between the two labels, images from Figure 5.10 C can be compared to Figure 5.11A. Although the magnification is different, both images display a similar degree of aggregation. Therefore it is plausible to assume that both AuNP labels aggregate to the same extent, which is governed by the NP density. Also, in Figure 5.11 the biochip surface was rinsed with deionized water during the final washing step in the bioassay procedure, thus freeing the surface from salt crystals.

The images shown in Figure 5.10 and 5.11 have been analyzed and a corresponding particle density expressed in particles/μm^2 was determined. This analysis was carried out for several different runs and the results are shown in Figure 5.12. Here the particle density is plotted versus the analyte concentration for both types of AuNP-labels. The trend clearly shows that a higher analyte (r-IgG) concentration results in a higher particle density and eventually this particle density saturates at higher [analyte]. This behavior is identical to the UV-vis

results shown in Section 5.3.5. Furthermore, there appears to be a consistent difference in response between the two types of labels. The average particle densities differ by a factor of 2-3. A similar trend was observed for the extinction response discussed earlier. This supports our findings that extinction scales with nanoparticle density and that there is a difference in label adsorption between the two types of labels. In the next section the bioassay response will be fitted to a model to investigate the biomolecule binding in more detail.

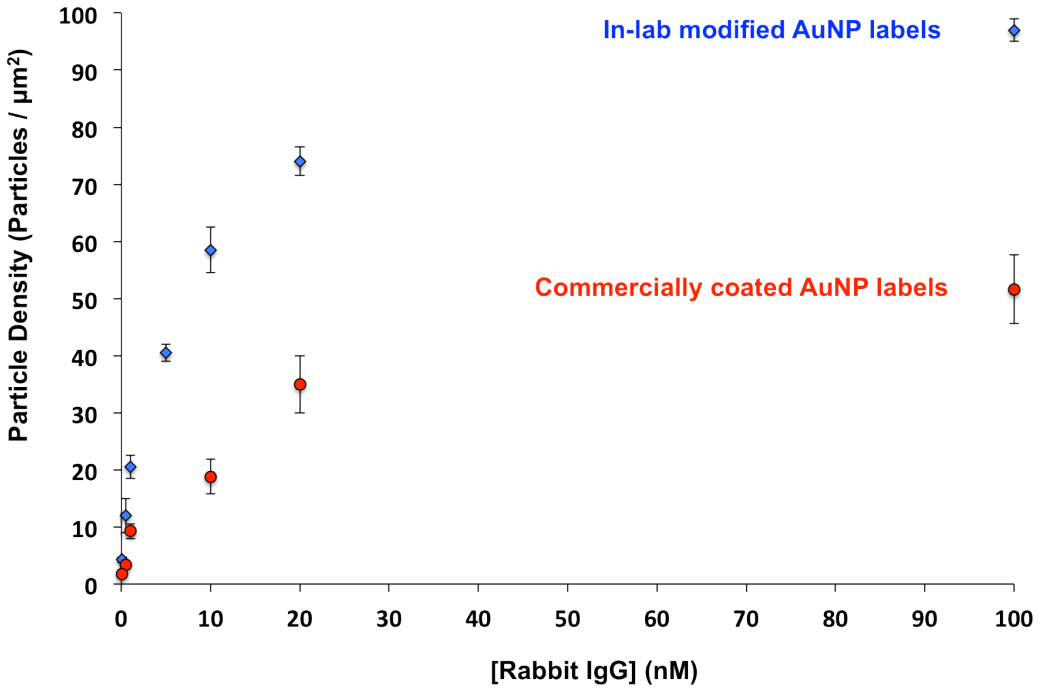

Figure 5.12. A plot of NP density at the biochip surface versus analyte (rabbit IgG) concentration for both in-lab modified and commercially coated 40 nm gold nanoparticle labels in a sandwich immunoassay. The error bars represent the standard deviation of the mean for a minimum of 2 separate bioassays with 3 different spots analyzed on each biochip.

5.3.7 Langmuir adsorption isotherm fits for immunoassay responses.

In order to compare the results between the two gold nanoparticle labels and to compare the results to previous immunoassays, we fitted both plots from Figure 5.09 to a Langmuir isotherm (Figure 5.13). This model assumes that all adsorption sites are equivalent, monolayer coverage results, and adsorbing molecules do not interact with each other. The parameters obtained from this fit can be compared to literature values. The Langmuir isotherm fit is based on equation 5-02:

$$Ext = \frac{Ext_{max}[antigen]}{K_d + [antigen]} \quad (5\text{-}02)$$

In this equation the variables have been adapted to properly reflect the analyte species under investigation and the resulting response. Here, *Ext* refers to the extinction resulting from the gold nanoparticle labels; Ext_{max} is the maximum response at saturation coverage; *[antigen]* refers to the concentration of the analyte (rabbit IgG); and K_d (M) is the dissociation constant for the antibody-antigen binding. In the literature a more common constant assessing binding strength is K_{ads} (M^{-1}) that is easily obtained from equation 5-03:

$$K_{ads} = {}^{1}/_{K_d} \quad (5\text{-}03)$$

The K_{ads} values calculated from the derived K_d values in Figure 5.13 were similar ($1 \pm 3 \times 10^8$ M^{-1}) for both in-lab and commercially coated AuNP-labels. This value compares well with reported values in the literature.[49-51]

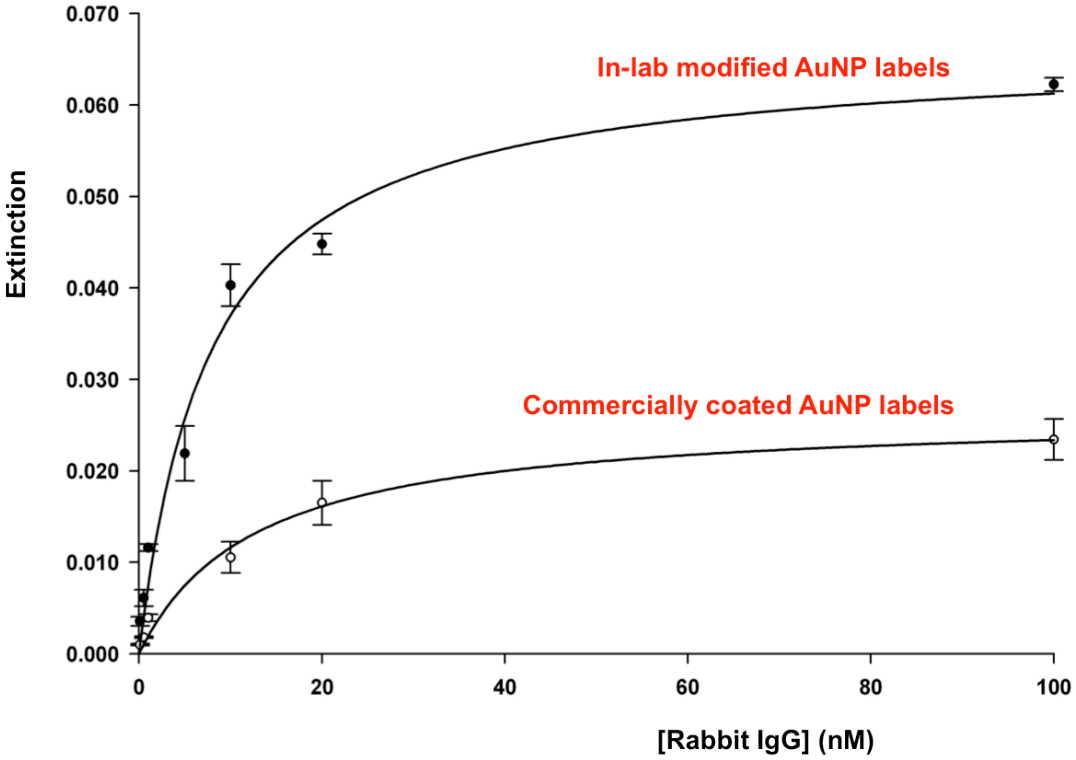

Figure 5.13. Langmuir adsorption isotherm fits for sandwich immunoassay results based on in-lab modified labels and commercially available AuNP labels. The fit yields K_d = 8 ± 2 x 10^{-9} M, Ext_{max} = 0.066 ± 0.004, and R^2 = 0.99 for in-lab modified AuNP labels; K_d = 13 ± 3 x 10^{-9} M, Ext_{max} = 0.026 ± 0.002, and R^2 = 0.99 for commercially coated AuNP labels.

Overall, the binding curves for the two different labels are similar, as expected, but deviations are observed when considering the Ext_{max} values and the linear region of the Langmuir isotherm fit. The top curve in Figure 5.13 (in-lab modified labels) has a much steeper linear region that spans a greater concentration range as opposed to the lower curve (commercially coated labels) resulting in a superior sensitivity for in-lab modified labels. Similarly the Ext_{max} value for the upper curve is approximately 3× greater, which is also true for every response at the same concentration. Hence, employing in-lab modified labels as illustrated in this sandwich immunoassay provides a better response and thereby puts less stringent requirements on instrumentation, as the signal is overall greater. Lastly, the detection limit at 100 pM for rabbit IgG is competitive with a SERS based sandwich immunoassay of approximately 10 pM[33] and a SPR based immunoassay of 77 pM.[49]

5.4 CONCLUSION

The implementation of an ultrathin film of titanium coated on quartz as the foundation for a sandwich immunoassay has proven to be successful. A robust diazonium salt derived phenyl acetic acid layer was spontaneously adsorbed to the titanium film. This adlayer provided the capability to covalently link the capture-agent used in this immunoassay, a rabbit IgG antibody, to the surface. IRRAS and AFM characterization support the successful surface modification and biomolecule attachment. This is the first report of diazonium-derived chemistry on titanium to immobilize biomolecules.

Further, this Chapter has effectively demonstrated the use of extrinsic AuNP-labels in the UV-vis detection of rabbit IgG in a sandwich immunoassay. Rabbit IgG was "sandwiched" between a capture layer and a rabbit antibody coated AuNP. In this fashion, the number of nanoparticles present on the biochip is directly related to the number of analytes captured. Therefore, monitoring the magnitude of the AuNP LSPR band provides an effective strategy to quantitate analyte binding in the assay. This method was able to detect 100 pM of analyte, which is competitive with other commonly used immunoassay detection methods such as surface plasmon resonance (SPR) and surface-enhanced Raman scattering. Additionally, UV-vis detection provides the benefit of being readily available in most analytical laboratories and requires minimal technical knowledge for operation. Lastly, with the development of other plasmonic labels such as silver nanoparticles and gold nanorods, the assay will provide the capability to detect multiple analytes simultaneously.

5.5 REFERENCES

1. Shipway, A. N.; Katz, E.; Willner, I. *Chemphyschem* **2000,** 1, (1), 18-52.
2. Wilson, R. *Chem. Soc. Rev.* **2008,** 37, (9), 2028-2045.
3. Anker, J. N.; Hall, W. P.; Lyandres, O.; Shah, N. C.; Zhao, J.; Van Duyne, R. P. *Nat. Mater.* **2008,** 7, (6), 442-453.
4. Mirkin, C. A. *MRS Bull.* **2010,** 35, (7), 532-539.
5. Saha, K.; Agasti, S. S.; Kim, C.; Li, X.; Rotello, V. M. *Chem. Rev.* **2012**.
6. Zamborini, F. P.; Bao, L. L.; Dasari, R. *Anal. Chem.* **2012,** 84, (2), 541-576.
7. Jans, H.; Huo, Q. *Chem. Soc. Rev.* **2012,** 41, (7), 2849-2866.
8. Nath, N.; Chilkoti, A. *Anal. Chem.* **2004,** 76, (18), 5370-5378.
9. Englebienne, P. *Analyst* **1998,** 123, (7), 1599-1603.
10. Dahint, R.; Trileva, E.; Acumnan, H.; Konrad, U.; Zimmer, M.; Stadler, V.; Himmelhaus, M. *Biosens. Bioelectron.* **2007,** 22, (12), 3174-3181.
11. Shao, Y. L.; Xu, S. P.; Zheng, X. L.; Wang, Y.; Xu, W. Q. *IEEE Sensors J.* **2010,** 10, (4), 3585-3596.
12. Porter, M. D.; Lipert, R. J.; Siperko, L. M.; Wang, G.; Narayanana, R. *Chem. Soc. Rev.* **2008,** 37, (5), 1001-1011.
13. Ni, J.; Lipert, R. J.; Dawson, G. B.; Porter, M. D. *Anal. Chem.* **1999,** 71, (21), 4903-4908.
14. Ulman, A. *Chem. Rev.* **1996,** 96, (4), 1533-1554.

15. Wasserman, S. R.; Tao, Y. T.; Whitesides, G. M. *Langmuir* **1989,** 5, (4), 1074-1087.

16. Asenath-Smith, E.; Chen, W. *Langmuir* **2008,** 24, (21), 12405-12409.

17. Haacke, G. *Annu. Rev. Mater. Sci.* **1977,** 7, 73-93.

18. Schroder, D. K. *IEEE Trans. Electron Devices* **1978,** 25, (2), 90-97.

19. Kuwana, T.; Darlington, R. K.; Leedy, D. W. *Anal. Chem.* **1964,** 36, (10), 2023-&.

20. Tian, H.; Bergren, A. J.; McCreery, R. L. *Appl. Spectrosc.* **2007,** 61, (11), 1246-1253.

21. Mrksich, M.; Dike, L. E.; Tien, J.; Ingber, D. E.; Whitesides, G. M. *Exp. Cell. Res.* **1997,** 235, (2), 305-313.

22. Postlethwaite, T. A.; Hutchison, J. E.; Hathcock, K. W.; Murray, R. W. *Langmuir* **1995,** 11, (10), 4109-4116.

23. Hatton, R. A.; Willis, M. R.; Chesters, M. A.; Briggs, D. *J. Mater. Chem.* **2003,** 13, (4), 722-726.

24. Donner, S.; Li, H. W.; Yeung, E. S.; Porter, M. D. *Anal. Chem.* **2006,** 78, (8), 2816-2822.

25. Dai, Y.; Swain, G. M.; Porter, M. D.; Zak, J. *Anal. Chem.* **2008,** 80, (1), 14-22.

26. Liu, Y. C.; McCreery, R. L. *Anal. Chem.* **1997,** 69, (11), 2091-2097.

27. Downard, A. J. *Electroanal.* **2000,** 12, (14), 1085-1096.

28. Combellas, C.; Kanoufi, F.; Pinson, J.; Podvorica, F. I. *Langmuir* **2005,** 21, (1), 280-286.

29. Pinson, J.; Podvorica, F. *Chem. Soc. Rev.* **2005,** 34, (5), 429-439.

30. Shewchuk, D. M.; McDermott, M. T. *Langmuir* **2009,** 25, (8), 4556-4563.

31. Mahmoud, A. M.; Bergren, A. J.; McCreery, R. L. *Anal. Chem.* **2009,** 81, (16), 6972-6980.

32. Starkey, E. B. *Org. Synth.* **1939,** 19, 40-42.

33. Wang, G. F.; Park, H. Y.; Lipert, R. J. *Anal. Chem.* **2009,** 81, (23), 9643-9650.

34. Jakubowicz, A.; Jia, H.; Wallace, R. M.; Gnade, B. E. *Langmuir* **2005,** 21, (3), 950-955.

35. Lofas, S.; Johnsson, B. *J. Chem. Soc. D* **1990**, (21), 1526-1528.

36. Johnsson, B.; Lofas, S.; Lindquist, G. *Anal. Biochem.* **1991,** 198, (2), 268-277.

37. Frederix, F.; Bonroy, K.; Reekmans, G.; Laureyn, W.; Campitelli, A.; Abramov, M. A.; Dehaen, W.; Maes, G. *J. Biochem. Bioph. Methods* **2004,** 58, (1), 67-74.

38. Meiggs, T. O.; Miller, S. I. *J. Am. Chem. Soc.* **1972,** 94, (6), 1989-&.

39. Hodgson, D. J.; Asplund, R. O. *Acta Crystallogr., Sect. C: Cryst. Struct. Commun.* **1991,** 47, 1986-1987.

40. Briand, E.; Salmain, M.; Herry, J. M.; Perrot, H.; Compere, C.; Pradier, C. M. *Biosens. Bioelectron.* **2006,** 22, (3), 440-448.

41. Boujday, S.; Gu, C. Y.; Girardot, M.; Salmain, M.; Pradier, C. M. *Talanta* **2009,** 78, (1), 165-170.

42. Boujday, S.; Methivier, C.; Beccard, B.; Pradier, C. M. *Anal. Biochem.* **2009,** 387, (2), 194-201.

43. Zhang, C. H.; Thompson, M. E.; Markland, F. S.; Swenson, S. *Acta Biomater.* **2011,** 7, (10), 3746-3756.

44. Nakajima, M.; Ishimuro, T.; Kato, K.; Ko, I. K.; Hirata, I.; Arima, Y.; Iwata, H. *Biomater.* **2007,** 28, (6), 1048-1060.

45. Roach, P.; Farrar, D.; Perry, C. C. *J. Am. Chem. Soc.* **2005,** 127, (22), 8168-8173.

46. Surewicz, W. K.; Mantsch, H. H.; Chapman, D. *Biochem.* **1993,** 32, (2), 389-394.

47. Marinakos, S. M.; Chen, S. H.; Chilkoti, A. *Anal. Chem.* **2007,** 79, (14), 5278-5283.

48. Driskell, J. D.; Uhlenkamp, J. M.; Lipert, R. J.; Porter, M. D. *Anal. Chem.* **2007,** 79, (11), 4141-4148.

49. Grant, C. Development and characterization of interfacial chemistry for biomolecule immobilization in surface plasmon resonance(SPR) imaging studies. University of Alberta, Edmonton, Alberta, 2009.

50. Kanda, V.; Kariuki, J. K.; Harrison, D. J.; McDermott, M. T. *Anal. Chem.* **2004,** 76, (24), 7257-7262.

51. Pribyl, J.; Hepel, M.; Halamek, J.; Skladal, P. *Sens. Actuators, B* **2003,** 91, (1-3), 333-341.

Chapter 6:

Conclusions and Future Work

6.1 CHAPTER CONCLUSIONS

The drive towards nanotechnology and its applications was the primary motivation for focusing the work conducted in this thesis on gold nanoparticles (AuNPs). The thesis was divided into two distinct parts; Chapter 2 and 3 revolved around the modification of gold nanoparticles using aryl diazonium cations; Chapter 4 and 5 demonstrated the use of gold nanoparticles as extrinsic labels in an UV-vis detection based bioassay. Both studies have provided new avenues and insights for the utilization of gold nanoparticles.

Chapter 2 introduced the usage of diazonium-derived films on AuNPs and focused on the interaction between the gold surface and the molecular layer. 4-nitrobenzene diazonium ion spontaneously adsorbed to the gold nanoparticle surface, and both UV-vis spectroscopy and surface enhanced Raman scattering (SERS) provided evidence for the presence of nitrobenzene at the surface. In the SERS spectrum, a band at 412 cm^{-1} was assigned to a gold-carbon stretch based on DFT calculations of a covalently linked nitrobenzene molecule to gold. This is the first direct evidence of a Au-C bond and explains the increased stability of diazonium-derived films on gold.

Chapter 3 further investigated the films formed by the spontaneous reduction of diazonium salts at the gold nanoparticle surface. Large shifts in the gold LSPR band due to modification and several bands between 1200 and 1300

cm^{-1} in the SERS spectra indicated multilayer formation. This was confirmed by comparing diazonium-derived layers to thiol monolayers with transmission electron microscopy (TEM). High-resolution images of modified gold nanoparticles clearly showed multilayers for nitrobenzene and nitroazobenzene diazonium salt derived films, whereas nitrobenzene thiols formed monolayers. The thickness of these multilayers can be controlled. Lastly, molecular layers on AuNPs formed from the spontaneous reduction of diazonium salts exhibited intense SERS spectra, which can find applications in SERS based assays that require a Raman active molecule to label the gold nanoparticle surface. The outcome of Chapters 2 and 3 have finally provided the long sought for evidence of a Au-C covalent bond in diazonium derived adlayers on gold. This should convince even the skeptics to give diazonium salts a try, as stable and versatile gold nanoparticles are high in demand.

Chapter 4 focused on the quantitation of AuNPs on quartz by UV-vis spectroscopy. Various sizes and concentrations of both silver and gold nanoparticles were adsorbed to modified quartz. Transmission UV-vis spectroscopy was used to measure the LSPR band magnitude, and scanning electron microscopy (SEM) provided a nanoparticle surface density measurement. It was demonstrated that the LSPR band intensity scaled with the number of nanoparticles adsorbed to quartz. Detection limits on the order of 10 particles / μm^2 for 40 nm AuNPs were achieved. This detection limit can be improved by employing larger nanoparticles as they have a greater extinction cross section.

Lastly, Chapter 5 brought the various research areas together in a biosensing application. A sandwich immunoassay was constructed by covalently linking a capture-molecule (rabbit IgG antibody) to quartz with the help of a thin film of titanium containing a spontaneously adsorbed phenylacetic acid diazonium salts adlayer. Various concentrations of analyte (rabbit IgG) were captured and labeled by rabbit IgG antibody coated gold nanoparticles, which were detected and quantitated by a standard benchtop UV-vis spectrometer. In this fashion analyte concentrations as low as 100 pM were detected, which is similar to detection limits observed for other techniques such as surface plasmon resonance (SPR). Chapters 4 and 5 described a new approach for using the gold nanoparticle LSPR band in biosensing. Quantitating the LSPR band magnitude provides a straightforward and robust measurement. Similar approaches utilizing fluorophores or dyes have been adopted for years in detection strategies such as fluorescence or chemiluminescence. Gold nanoparticles exhibit extremely high molar extinction coefficients that typically outperform organic dyes, therefore it makes sense to employ these nanospheres in applications such as these.

6.2 FUTURE WORK AND OUTLOOK

The work conducted in this thesis on the modification of gold nanoparticles by the spontaneous reduction of diazonium salts shows a new and simple method to covalently attach molecular layers to AuNPs. The majority of work on diazonium salt grafting has been carried out on planar substrates, and only recently have nanostructures shifted to the focus of attention of such

research. A comprehensive review on diazonium salt chemistry with up to date applications has recently been published by Dr. Chehimi entitled “Aryl Diazonium Salts”.[1] The book emphasizes the need for stable reproducible adlayers on commonly used surfaces in biosensing such as gold. To date the majority of bioassays still rely on alkanethiols to attach capture-molecules onto a planar support, which then selectively binds the analyte of interest. However extended sensing times necessary for a number of analytes degrades the alkanethiol layer that holds the capture molecule in place and thus compromises the integrity of the bioassay.[1] This is where diazonium salt derived adlayers should enjoy increased attention in the near future.

Moreover, this thesis introduced the spontaneous adsorption of phenylacetic acid diazonium salt on titanium to immobilize biomolecules. This titanium substrate as a foundation provides ease of modification, stability and reproducibility. The phenylacetic acid layer was exposed to various buffers for up to 48 h without any apparent loss in functionality. Furthermore, the extent of multilayer formation can generally be controlled by changes in incubation time or concentration, thereby allowing for more flexibility. My colleague has shown that multilayers can double the binding capacity in bioassays and thereby facilitate a greater response.[2] However, one drawback of the capability to change film thickness is reproducibility, and extra care must be taken to employ the exact incubation conditions to minimize chip-to-chip variability. Future work will have to evaluate if this limitation has a significant impact.

Another area of interest for diazonium salts will be in the modification of silver nanoparticles (AgNPs). There is a strong drive for the integration of silver nanoparticles in medical sciences ranging from implant research to sensing.[3] These nanoparticles exhibit greater extinction cross sections than gold nanoparticles and additionally have useful antimicrobial properties.[3] The ongoing issue with the usage of silver nanoparticles in a variety of sensing applications is the chemical degradation and oxidation of these nanoparticles.[4] Several reports have commented on the difficulty of forming AgNPs that remain stable over extended periods.[5, 6] Initial experiments to modify silver nanoparticles with diazonium salts have shown promising SERS spectra, and it is my belief that diazonium salt chemistry will be beneficial in this area of research.

The second part of this thesis introduced a new detection method for immunoassays, as was demonstrated using gold nanoparticles. The detection relies on the magnitude of the nanoparticle LSPR band, and has the capability for multiplexing by employing a variety of different labels. The main requirement for multiplexing is that the LSPR bands are sufficiently separated, and Chapter 4 showed baseline resolution between silver and gold LSPR bands. However, the silver nanoparticle surface chemistry remains an issue and several attempts to achieve reproducible results have failed. As mentioned previously I would like to see the diazonium salt chemistry be extended to silver nanoparticles in hopes of successfully incorporating AgNPs in this type of immunoassay.

Another potential label that has gained significant attention in recent years is gold nanorods. They can be synthesized in a variety of different aspect ratios,

producing tunable LSPR bands in the near infrared region. These nanorods exhibit excellent optical properties superior to gold nanoparticles in terms of extinction cross section. The extinction efficiency is approximately 20 times greater for nanorods compared to nanospheres.[7] Further, their absorbance at higher wavelengths enables *in vivo* applications, as tissue only weakly absorbs photons at those wavelengths.[8] Due to their superior properties they have been employed in biosensing applications resulting in highly sensitive biosensors,[9] and more recently allowing for single molecule detection.[10]

The introduction of new labels with higher extinction cross sections such as gold nanorods in the UV-vis detection of biomolecules is promising. Multiplexing will unquestionably make this method more competitive, and the optimization and utilization of new labels will also contribute to improve the detection limits of this technique. Furthermore, the instrumentation side can likely be improved upon to detect weaker signals. With the implementation of these changes I foresee an improvement by 1-2 orders of magnitude of the current 100 pM detection limit.

6.3 REFERENCES

1. Chehimi, M. M., *Aryl Diazonium Salts*. 1st ed.; Wiley-VHC 2012.
2. Grant, C. Development and characterization of interfacial chemistry for biomolecule immobilization in surface plasmon resonance(SPR) imaging studies. University of Alberta, Edmonton, Alberta, 2009.
3. Mody, V. V.; Siwale, R.; Singh, A.; Mody, H. R. *J. Pharm. Bioall. Sci.* **2010,** 2, (4), 282-289.
4. Liu, Y.; Huang, C. Z. **2012,** 137, (15), 3434-3436.
5. Cao, Y. W.; Jin, R.; Mirkin, C. A. *J. Am. Chem. Soc.* **2001,** 123, (32), 7961-7962.
6. Vidal, B. C.; Deivaraj, T. C.; Yang, J.; Too, H. P.; Chow, G. M.; Gan, L. M.; Lee, J. Y. *New J. Chem.* **2005,** 29, (6), 812-816.
7. Pissuwan, D.; Valenzuela, S. M.; Cortie, M. B. *Biotechnol. Genet. Eng.* **2008,** 25, 93-112.
8. Tong, L.; Wei, Q. S.; Wei, A.; Cheng, J. X. *Photochem. Photobiol.* **2009,** 85, (1), 21-32.
9. Yu, C. X.; Irudayaraj, J. *Anal. Chem.* **2007,** 79, (2), 572-579.
10. Ament, I.; Prasad, J.; Henkel, A.; Schmachtel, S.; Sonnichsen, C. *Nano Lett.* **2012,** 12, (2), 1092-1095.